Magnetic Field Generation and B-Dot Sensor
Characterization in the High Frequency Band

THESIS

Ryan L. Hardin, Captain, USAF

AFIT/GE/ENG/12-20

DEPARTMENT OF THE AIR FORCE
AIR UNIVERSITY

AIR FORCE INSTITUTE OF TECHNOLOGY

Wright-Patterson Air Force Base, Ohio

Magnetic Field Generation and B-Dot Sensor Characterization in the High Frequency Band

THESIS

Presented to the Faculty

Department of Electrical and Computer Engineering

Graduate School of Engineering and Management

Air Force Institute of Technology

Air University

Air Education and Training Command

In Partial Fulfillment of the Requirements for the

Degree of Master of Science in Electrical Engineering

Ryan L. Hardin, B.S.E.E.

Captain, USAF

March 2012

AFIT/GE/ENG/12-20

Magnetic Field Generation and B-Dot Sensor Characterization in the High Frequency Band

Ryan L. Hardin, B.S.E.E.

Captain, USAF

Approved:

_____

Lt Col Geoffrey A. Akers, PhD
(Chairman)

_____

date

_____

Dr. Andrew J, Terzuoli, PhD (Member)

_____

date

_____

Dr. Michael J. Havrilla, PhD (Member)

_____

date

Abstract

Designing a high frequency (HF) magnetic field direction finding (DF) array for use onboard a military aircraft is the challenge that drives the effort of the research presented. The frequency range of interest, 2-32 MHz, has a maximum wavelength (150 meters) that exceeds the maximum length of any platform in the USAF inventory. The large wavelengths in the HF range make it difficult to accurately estimate from which direction a magnetic field is emitting. Accurate DF estimates are necessary for search and rescue operations and geolocating RF emitters of interest.

The primary goal of this research is to characterize the performance of the MGL-S8A (Multi-Gap loop) B-Dot sensor. Although the sensors are designed to operate at frequencies above 5 GHz, their small size and potential to accurately detect magnetic fields in the 2-32 MHz range make them likely to be one type of an ensemble of sensors in the design of an HF DF array. The sensors are characterized in the azimuthal angles of 0, 45, -45, 90, and -90 degrees. Each sensor is characterized using two different types of magnetic field generators, a transverse electromagnetic (TEM) cell and a Helmholtz coil. The TEM cell generates a consistent magnetic field that acts as the input to the B-Dot sensor. The second type of magnetic field generator used, which is also the secondary objective of this research, is a Helmholtz coil. An ideally designed Helmholtz coil is intended to be an inexpensive alternative to help in the characterization of B-Dot sensors in the HF range.

The sensors can accurately measure electromagnetic (EM) fields in the HF frequency range. Although the detection capability of the sensors is very good, the small differences between the 0 and 45 degree measurements may make it difficult for the sensors to be used in a DF array.

Acknowledgements

The completion of this thesis proves that there are never any road blocks, only speed bumps. The knowledge and experience gained while conducting this research will no doubt stick with me through my Air Force career and beyond. It is sometimes hard to admit that despite all the frustration, I enjoyed writing my thesis. All the knowledge I gathered during my tenure at AFIT definitely had me up at night contemplating, "Is this right?" or "How can I do this better?"

I could never have finished this research on my own. I want the thank my thesis committee, Dr. Terzuoli and Dr. Havrilla for their help in my research. Also, despite being deployed during the majority of my time at AFIT, Major Gooodman played an important role which helped guide my research. I would like to thank the sponsors of my research, AFRL, I hope the research conducted and end result of this thesis help to determine the future role of the B-dot sensor.

I would especially like to thank Joshua Wilson and Stephen Hartzell of the SOCHE research assistance team for their work on the CST simulations of the B-dot sensor and the Helmholtz coil. Also, their insight towards the operation of the coil and sensor definitely helped to guide me and keep me on the correct path to achieve my goal. I know the future is bright for Josh and Stephen, and I hope to get the opportunity to work with them again in the future.

Furthermore, I would like to thank Dr. Lorenzo LoMonte from AFRL and Dr. Edmond Wong and Dr. Marcio DeAndrade from SPAWAR. These gentlemen helped me to understand the theory of the Helmholtz coil and magnetic field sensors. They never seemed putout by answering my elementary electromagnetic field questions and were always more than happy to explain the finer points of EM fields.

I also want to thank my wife and daughter. They always understand why I spend countless hours at school and why I had to go out of town to make measurements. They also understand why I had to confine my self to my office while writing my thesis. They may not know it, but they played a big role in keeping me sane during

my time at AFIT by providing a shoulder to lean on and someone to talk to, I surely appreciate that.

Most of all, I want to thank my advisor, Lt Col Geoffrey Akers. I am so grateful to have an advisor that played such an active role during my research, without him I would not have been able to complete nearly as much as I did. He always pointed me in the right direction and kept me goal oriented. I am glad he ended up being my advisor and I hope I did a good enough job for him, Thanks Lt Col Akers.

Ryan L. Hardin

Table of Contents

List of Figures

xi

List of Tables

Magnetic Field Generation and B-Dot Sensor Characterization in the High Frequency Band

I. Introduction

1.1 Introduction

In a world overcome with technology, dependency on electronic devices has become more and more prevalent throughout the years. Cell phones, radio and wireless networks are just a few examples of the technology that the world has become dependent on. The military is one of many organizations that exceedingly relies on electronic transmission device such as these, not just for personal use, but for mission readiness. Because of our dependency on transmission devices and the important role they play in our national defense, it is important to understand how they work. All wireless transmission devices operate by emitting electromagnetic fields. These fields are all around us and their applications are often taken for granted. Since first understanding EM fields, the military have benefitted by incorporating them into nearly all of their assets. Radars, radios and aircraft landing systems are just a few of the systems that use EM fields as a primary resource. Communication systems such as these have always been, without a doubt, a major contribution to any war-fighting effort and show the importance of electromagnetic fields and the role they play.

All electronic devices transmit an EM field which radiates indefinitely throughout space. These fields can be treated as a combination of an electric field and a magnetic field, or **E** and **H** field respectively. The details in which the charges and currents interact with the electromagnetic field are described in Maxwell's equations and the Lorentz force law. There are numerous electrical systems on an aircraft such as the avionics, radios, and instrument landing systems that emit and are susceptible to EM field transmissions. These magnetic fields interact with other electrical equipment on board, causing interference. The interference, or noise, generated by the

electrical equipment on board an aircraft can make it difficult to detect other fields of interest.

The Multi-Spectral Sensing and Detection Division within sensors directorate of the Air Force Research Laboratory (AFRL) at Wright-Patterson AFB and the Air Force Institute of Technology (AFIT) are working together to build an efficient, low cost magnetic field detection system. This system will be used for sensing low intensity magnetic fields in the 2-32 MHZ high frequency range onboard a military aircraft. Due to the long wavelengths that correspond to the HF range (approximately 150 meters at 2 MHz and 9 meters at 32 MHz), the angular resolution, given this scenario, is limited since an array of sensors cannot be placed throughout the aircraft one-half wavelength apart. As a result of this limitation to accurately detect and determine the direction of a magnetic field, AFIT and AFRL have embarked on a research project to find a solution to this challenge. The goal is to introduce a smaller and cheaper sensor that can be used in conjunction with the current state-of-the-art sensors. The addition of the new sensors would increase the sensor array direction finding capability in the HF range.

The sensors investigated in this research are commercially built MGL-S8A B-Dot sensors, as seen in Figure 1.1. Understanding the RF characteristics of the sensor will help the engineer determine locations for the sensors throughout the aircraft.

Practical sensor locations may be confined to the upper and lower portions of the aircraft fuselage and at each of the wing tips. Together with the current state-of-the-art sensors, the MGL-S8A sensors placed throughout the aircraft will be used as a secondary detection resource to help verify the direction of any magnetic fields of interest. Figure 1.2 gives an example of a potential direction finding array with several MGL-S8A sensors placed at the aircraft wing-tips, nose, tail and fuselage.

The research conducted within in this thesis explores:

1. The frequency and angular response characterization of the MGL-S8A magnetic field sensor from 2-32 MHz at azimuthal angles of 0, 45, -45, 90 and -90 degrees,

Figure 1.1:   MGL-S8A B-Dot Sensor
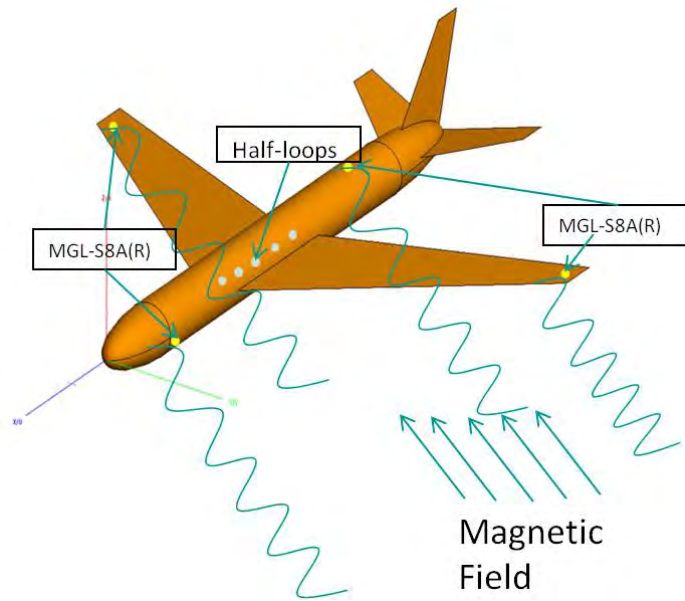
Figure 1.2:   Direction Finding Array - Sensor Placement

2. The simulation, construction, and analysis of a uniform magnetic field generating platform with which to characterize the sensor - Helmholtz coil,

3. The comparison of two separately manufactured MGL-S8A B-Dot sensors originally designed to operate at frequencies greater than 5 GHz.

Magnetic field sensors have been widely used for navigation, vehicle detection, current sensing, and spatial and geophysical research. Reconnaissance aircraft are often equipped with direction finding systems for spatially locating sources, or emitters, of magnetic radiation such as communication and radar systems. These aircraft and their direction finding capabilities play an integral part in many Air Force missions. However, the DF capabilities used in these aircraft are typically optimized to detect VHF to microwave frequencies. These DF techniques are an exceptional capability; however, due to the long wavelengths of the HF spectrum, it becomes a challenge to accurately detect and determine the direction of an HF signal.

The research presented here examines magnetic field variations in the 2-32 MHz frequency spectrum. Accurately determining the presence of an outside magnetic field is important when distinguishing between interference, noise, and the signal of interest. The comparison between the signal and noise is commonly referred to as the signal-to-noise ratio (SNR). Determining the presence of a magnetic field is one key aspect in the research of this thesis. Examination of magnetic field intensities and the time rate of change of the field in the 2-32 MHz range will be explored to determine if the sensors of interest have the sensitivity to be used in a HF DF system. The goal of this research and any further research in this field, is to implement the frequency response characterization of one of these sensors to produce a new, inexpensive, magnetic field detection finding capability in the HF range. Such a system will consist of an ensemble of different B-Dot sensors placed onboard an aircraft in a non-uniform array and used to detect changes in the already present magnetic fields. The implementation of this system will allow the aircraft operator and determine the direction of transmitted fields in the 2-32 MHz range. It will serve as a valuable situational awareness tool and may prove to be an integral asset to the current DF system by providing increased effectiveness and capability.

1.2 Scope and Assumptions

The scope of this research is limited to the characterization and comparison of the URS and Prodyn MGL-S8A B-Dot sensors. Sensor characterization is based on the CST Microwave Studio® simulation and on measurements from a consistent magnetic field generator (TEM cell and Helmholtz coil) in the 2-32 MHz range. Because the DF platforms on which the sensor array may be utilized are intended to operate at a considerable distance from the emitter they are attempting to locate, it is assumed that all incident magnetic field waves have a planar wave front (far-field approximation). It will also be assumed that the waves are linearly polarized and, for the scope of this research, any electromagnetic interaction between the sensor array and the platform on which the array is mounted are also ignored. It is important, however, to understand that the interaction between the sensor array and the platform can have a significant impact on the sensor's field measurement. Finally, it is also assumed that the sensor array is operating in an ideal environment, homogeneous free-space propagation, no atmospheric disturbance, perfect system processing and no implementation bias.

CST Microwave Studio® will serve as the modeling and simulation software for the B-Dot sensors and the Helmholtz coil. CST enables the fast and accurate analysis of HF devices such as antennas, filters, couplers, planar and multi-layer structures and signal integrity analysis and electromagnetic compatibility effects [14]. The research will also use the MATLAB® R2010b software suite. MATLAB® is a high-level language and interactive environment that enables the performance of computationally intensive tasks [10]. The convenience and familiarity of the MATLAB® software suite was chosen to run the analytical calculations needed towards research completion. Additional equipment needed will be provided through AFIT, AFRL and other outside organizations.

5

1.3 Problem Statement and Research Goals

The MGL-S8A B-Dot sensors were originally designed under Air Force Weapons Laboratory (AFWL) contract number F29601-75-R-0085 in 1975. The sensor is a multi-gap loop half cylinder on a ground plane (as seen in Figure 1.1). The sensor produces a voltage output in response to a time variant magnetic field, or B-field, input. The AFWL sensors, which are now produced by two New Mexico based companies, URS and Prodyn, are the sensors used in this research and will potentially be the sensors placed in the nose, wings, and tail of the aircraft when the sensor array is constructed. The Prodyn and URS sensors are high quality sensors designed for a frequency response greater than 5 GHz, and not designed to operate efficiently in the 2-32 MHz range.

The first task involved in completing the research towards the characterization and implementation of the MGL-S8A B-Dot into the sensor array is to characterize the sensors through modeling and simulation. Due to the advancement of computer technology, it has become common practice to model and simulate any device to the extent it can be simulated. Modeling helps by building a foundation of expected values and aids in the verification of the item under test, it also cuts down on testing costs. Due to their similar designs, Figure 1.3 serves as the model used to simulate both the Prodyn and URS B-Dot sensors.

The simulations will be accomplished using the Computer Simulation Technology (CST) Microwave Studio® in the AFIT Low Observables Radar and Electromagnetics (LORE) Laboratory. The characterization simulation will provide useful information with which to compare the sensors against actual measured values.

After the modeling and simulations are complete, the next step is to characterize the sensors against a steady magnetic field at azimuth orientations of 0, 45, -45, 90 and -90 degrees from 2-32 MHz. Measurements will be done in two ways. The first method of characterization is to simulate and build a Helmholtz coil for in-house use at AFIT. A Helmholtz coil can be used for high quality, low frequency magnetic field
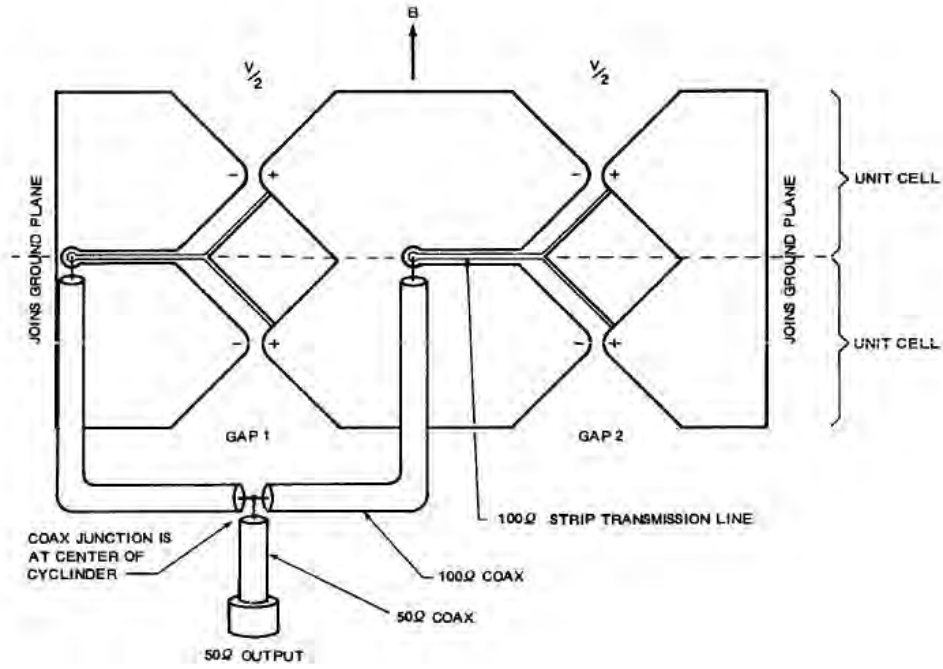
Figure 1.3:   Schematic Drawing of the Prodyn MGL-S8A B-Dot Sensor

susceptibility testing. Developing the coil would reduce electromagnetic compatibility qualification test time and provide a relatively uniform sensor for characterization [1]. The second method used to characterize the B-Dot sensors is to use a transverse electromagnetic (TEM) cell. The TEM cell provides a uniform magnetic field from 2-32 MHz in an enclosed test compartment which helps reduce outside interference. Because the TEM cell field performance is calibrated and validated, it can be used as a truth reference; the results given from the TEM cell will be used as a control to verify the accuracy of the Helmholtz coil.

Once the sensor measurements have been taken, the third task in this research effort is to compare the URS and Prodyn sensors to each other and the analytical and simulated values. Although the sensors are essentially the same design, it is important to compare the frequency response and magnitudes of each sensor. Making this determination will help guide the decision on which sensor will possibly be used in the sensor array.

In conclusion, the primary goal of this thesis is to determine if a magnetic field sensor designed to operate at frequencies greater than 5 GHz can be properly simulated and characterized in the 2-32 MHz frequency spectrum at all azimuthal angles. The sensor capability will be evaluated to determine if it can be used efficiently to improve the DF system performance on existing USAF assets. A secondary goal is to simulate and construct a magnetic field generator (Helmholtz coil). The coil will provide a consistent magnetic field that will be used in the characterization and analysis of the magnetic field sensors. The development of the coil will also aid in future research and testing. It will provide an inexpensive, in-house field generator that would provide the consistent fields needed to test sensors in the 2-32 MHz range.

1.4   Document Organization

This thesis contains measured characteristics of the MGL-S8A B-Dot sensor and comparisons between the Prodyn and URS B-Dot sensors. Chapter II provides background information on magnetic field theory, Helmholtz coils, and B-Dot sensors. Chapter III describes the methodology used to develop an ideal Helmholtz coil and the steps taken to characterize the B-Dot sensors in both the TEM cell and Helmholtz coil. Chapter IV summarizes the sensor characterization and provides expected versus measured analysis of the sensors in both the TEM cell and Helmholtz coil. Chapter IV also provides a comparison analysis between the two types of B-Dot sensors used. The final chapter presents conclusions on the performance of the B-Dot sensors and possible future developments that may help improve magnetic field generation and detection [13] [9].

II. Background

2.1 Introduction

This thesis explores the theory of magnetic fields, the methods used in field generation, and the applications and detection capability of magnetic field sensors, specifically the MGL-S8A B-Dot sensor. This section provides a background on research completed regarding the concept of magnetic fields, magnetic field generators, and magnetic field sensors. All background information presented in this section will build a solid foundation in the theory of magnetic fields and define the scope of the research conducted. The research conducted within this thesis will help to determine how the performance of the small MGL-S8A B-Dot sensors compares to simulated structurally-integrated antennas in the 2-32 MHz HF spectrum [4]. The reason for detecting magnetic fields in the HF spectrum is to determine the presence and direction of magnetic fields. The small B-Dot sensors provide an unobtrusive B-field detection array throughout the aircraft which will help provide awareness of surrounding magnetic fields and increase the aircraft direction finding capability. The structurally-integrated antennas which the sensors will be compared with were simulated by the Berriehill Research Corporation and have been the topic of previous AFIT research [4]. The previous research conducted in regards to the simulated Berriehill antennas will be compared against the measurements taken with the MGL-S8A B-Dot sensors.

The scope of this research will be to simulate and develop a magnetic field generator, Helmholtz coil, and characterize the small B-Dot sensors in the HF range using the Helmholtz coil. Another parallel approach used for the characterization of the B-Dot sensors is the use of a TEM cell. The TEM cell generates a stable magnetic field that will provide accurate measurements of the B-Dot sensors, which can then be used as a comparison tool to verify the accuracy of the Helmholtz coil. Once satisfactory results are achieved, the two MGL-S8A B-Dot sensors from different manufacturers will be compared to each other to determine performance and efficiency. All Helmholtz coil and B-Dot sensor simulations will be accomplished using CST

Microwave Studio® and current MATLAB® software. The simulations will provide a solid baseline to begin construction of the Helmholtz coil and help to determine the expected values of the B-Dot sensors. Once simulations are complete, the coil will be constructed and will be used to measure the frequency and angular performance of the B-Dot sensors.

2.2 Magnetic Fields

Magnetic fields are the basis for this research and are the core building block behind the research and theory within this thesis. Although magnetic fields can theoretically be explored independently, they are more easily understood when partnered with the electric field. This section provides the theory and background of electromagnetic fields. Prodyn Technologies [7], is one of the manufacturers of the B-Dot sensors used during this research. Prodyn provides relevant magnetic field theory needed to understand EM fields and the interaction of the fields with the sensors. Electromagnetic radiation is the transportation of energy through a medium by simultaneous propagation of a time variant electric field and an associated covariant magnetic field. EM radiation can be in the form of a continuous wave (CW), as in radio waves, or a single burst as in an electromagnetic pulse (EMP). The electric and magnetic fields which occur in a traveling wave or a burst are related to each other, to the power transmitted by the wave or burst, and to the properties of the medium [7]. The relationship, in free space, is described by the cross product of the $\mathbf{E}$ and $\mathbf{H}$ fields which results in the Poynting Vector $\mathbf{S}$:

$$\mathbf{S} = \mathbf{E} \times \mathbf{H} = \mathbf{E} \times \frac{\mathbf{B}}{\mu_o} = \frac{\mathbf{D} \times \mathbf{B}}{\mu_o \varepsilon_o} = c^2 \, \mathbf{D} \times \mathbf{B} \, \left(\frac{W}{m^2} \right), \qquad (2.1)$$

where:

$\mathbf{S}$ = power density being transported, W/m^2

$\mathbf{E}$ = electric field strength, V/m

$\mathbf{H}$ = magnetic field strength, amp/m

$\mathbf{B}$ = magnetic induction, Tesla

$\mathbf{D}$ = electric displacement, coul/m2

μ_o = permeability of free space, $4\pi \text{x} 10^{-7}$ (Tesla-m)/A

ε_o = permittivity of free space, $8.85 \text{x} 10^{-12}$ farad/m

c = speed of light in free space, $3 \text{x} 10^8$ m/sec

Equation (2.1) can be used as a comparison tool to help understand the relationship between the Poynting vector, the $\mathbf{E}$ and $\mathbf{H}$ fields, and the associated relationship of the $\mathbf{D}$ and $\mathbf{B}$ fields when accounting for the permittivity and permeability of free space, respectively. The electric and magnetic fields are orthogonal, so the magnitude of the Poynting vector is the electric field, E, times the magnetic field, H, or E times B/μ_o. The direction of the Poynting vector is the direction of propagation. The Poynting vector readily describes how an EM wave or burst transmits power through an area perpendicular to the direction of propagation:

$$P = \int \mathbf{S} \cdot dA = SA \ (W) \tag{2.2}$$

or

$$S = \frac{P}{A} = \frac{E \times B}{\mu_o} \left(\frac{W}{m^2} \right). \tag{2.3}$$

The Poynting vector is an important analytical concept to understand and if it can be evaluated, often the problem can be solved. Because the Poynting vector is such a powerful tool, it is important to understand how it is derived and the properties that are included within. The first important property to understand is the relationship of the speed of light to the properties of free space; this relationship can be presented by

$$c^2 = \frac{1}{\mu_o \varepsilon_o}. \tag{2.4}$$

11

Equation (2.4) is an outcome of Maxwell's field theory and is the starting point in deriving and understanding many other field relationships. This relationship is also used to describe the impedance of free space

$$c\mu_o = \frac{1}{c\varepsilon_o} = \sqrt{\frac{\mu_o}{\varepsilon_o}} = Z_o, \tag{2.5}$$

where Z_o represents free space impedance. Maxwell's field theory can simplified further; it can be used to relate the ratio of the electric and magnetic field components to the speed of light

$$c = \frac{E}{B}. \tag{2.6}$$

Combining the relationship between propagation speed, field strength, the Poynting vector magnitude, and the impedance of free space, we obtain:

$$S = \frac{P}{A} = \frac{E \times B}{\mu_o} = \frac{E^2}{c\mu_o} = \frac{E^2}{Z_o} \tag{2.7}$$

or

$$P = \frac{E^2 A}{Z_o}. \tag{2.8}$$

Because $E^2 A$ has the units of V^2 and Z_o has the units of ohms, the similarities to Ohm's law can be seen $(P = V^2/R)$. Realizing the relationship between Ohm's law and the Poynting vector, one can apply the Poynting vector to a length of wire and calculate the electrical power infused in it or radiated from it. The utility of the Poynting vector in EM measurements lies in the ability to measure either or both of the constituent field intensities and calculate the radiated power density, or to calculate either or both of the constituent field intensities from a specified radiated power density [7]. Having given a brief background on the theory behind EM fields and their relationship in speed, magnitude, field strength, and free space impedance,

the remainder of this section will focus on continuous wave (CW) magnetic fields. The magnetic field in a CW is defined as

$$B(t) = B_p \sin(2\pi f_o t), \tag{2.9}$$

where B_p is the amplitude or maximum value, f_o is the frequency, and t is the time. The signal induced in a conducting loop with an area A, normal to the direction of propagation, is directly proportional to the time rate of change, or derivative of the magnetic field intensity (Faraday's Law):

$$V(t) = \frac{dB(t)}{dt} A_{eff}, \tag{2.10}$$

where A_{eff} is the effective area of the B-Dot sensor and the derivative B with respect to time is defined as:

$$\frac{dB}{dt} = 2\pi f_o B_p \cos(2\pi f_o t). \tag{2.11}$$

As can be seen from (2.11), the derivative of the B field has the same waveform as the B field with the exception of an amplitude magnification of $2\pi f_o$ and a phase shift of $\pi/2$.

The above introduction to EM fields provides sufficient information behind the theory of magnetic fields and will help to understand the remainder of this thesis and the research conducted in magnetic field generation and sensing.

2.3   Magnetic Field Generation

Magnetic field generation is a critical portion of this thesis and the research conducted. The magnetic field generation technique used for this research is the development of a Helmholtz coil and the use of a TEM cell. The Helmholtz coil is intended to be designed and used as an inexpensive test platform to aid in the characterization of B-Dot sensors in the 2-32 MHz frequency range. The TEM cell

test method is used because it provides a known, accurate magnetic field that will ensure accurate measured results of the B-Dot sensor. This section will begin by focusing on the theory behind the Helmholtz coil and then explain the concept of the TEM cell.

2.3.1 Helmholtz Coil.

A Helmholtz coil is a device used to produce a stable, uniform magnetic field [16] and is often used for high quality susceptibility testing [1] and sensor characterization (See Figure 2.1).
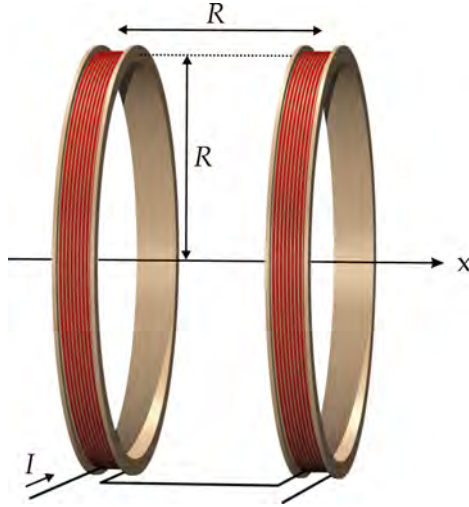
Figure 2.1:   Helmholtz Coil

The Helmholtz coil design required for this research is to generate a magnetic field in the HF range from 2-32 MHz. The coil will provide the sensor under test a uniform, consistent magnetic field needed to accurately characterize the B-Dot sensors. Developing and building a Helmholtz coil is best done using the variational principle. The variation principle that works best for Helmholtz coils is the use of Lagrangian multipliers [1]. This method is the best for determining required field strength, coil dimensions, and input current; however, certain trade-offs need to be made to account for the ideal operation and generation of the magnetic field. An ideal Helmholtz coil for this research requires the self resonance to be outside the 2-32 MHz

frequency range of interest, the magnetic field to be maximized, the self and mutual inductances to be minimized, the impedance to be minimized, and the electric field to be minimized. There are several ways to approach the development of a Helmholtz coil, but certain constraints need to be determined to optimize the coil parameters and the variables. For example, to maximize the resonance frequency with the magnetic field as a constraint condition would require solving the simultaneous equations, or constraint equations

$$\frac{\partial F}{\partial N} + \lambda \frac{\partial B}{\partial N} = 0 \tag{2.12}$$

and

$$\frac{\partial F}{\partial r} + \lambda \frac{\partial B}{\partial r} = 0, \tag{2.13}$$

where F is the resonant frequency, B is the magnetic field, N is the number of turns on each side of the coil, and r is the radius of the coil (λ is the Lagrange multiplier which will be defined later). Solving these two equations simultaneously yields the maximum magnetic field for a given number of turns, coil radius, and self resonance value. The constraint equation can be used in a variety of ways. Maximizing the B-field while using current as a constraint or to minimizing the E-field while using the B-field as a constraint are just some of the options available when using the constraint equation. Understanding the constraint equations designed for optimal Helmholtz coil production is important, but it does require more detail and explanation using Lagrangian multipliers. For instance, the expression for the resonant frequency of a series connected alternating current (AC) Helmholtz coil is

$$F = \frac{1}{2\pi \sqrt{(L + M)(C_o + C_G)}}, \tag{2.14}$$

where:

F = resonant frequency, Hz

15

L = external inductance of the coil, Henries

M = mutual inductance between the coil pair, Henries

C_o = coil inter-winding capacitance, farads

C_G = coil capacitance to ground, farads

The mutual inductance is defined as

$$M = \alpha N^2 r \tag{2.15}$$

and the series inductance can be estimated using

$$L = N^2 r \mu_o \left[\ln \left(\frac{16r}{a} \right) - 2 \right], \tag{2.16}$$

where:

$\alpha = 0.494 \times 10^{-6}$, Henries/meter

N = number of turns in the coil, per side

r = radius of Helmholtz coil, meters

μ_o = permeability of free space, Henries/meter

a = diameter of wire bundle cross section

Because the inductance is directly proportional to the number of turns squared, the number of turns must be minimized in order to keep the inductance down. Now that the resonant frequency has been defined, the derivative must be taken with respect to N and r, this is the next step in solving the constraint (2.12)

$$\frac{\partial F}{\partial N} = \frac{- \left[2Nr\mu_o \left(\ln \left(16\frac{r}{a} \right) - 2 \right) + 2\alpha Nr \right]}{\left[4 \left[\pi \left[\left[N^2 r \mu_o \left(\ln \left(16\frac{r}{a} \right) - 2 \right) + \alpha N^2 r \right] C_T \right]^{\frac{3}{2}} \right] \right]^{C_T}} \tag{2.17}$$

and

16

$$\frac{\partial F}{\partial r} = \frac{-\left[N^2 \mu_o \left(\ln\left(16\frac{r}{a}-2\right)+N^2\mu_o+\alpha N^2\right)\right]}{\left[4\left[\pi\left[\left[N^2 r\mu_o\left(\ln\left(16\frac{r}{a}\right)-2\right)+\alpha N^2 r\right]C_T\right]^{\frac{3}{2}}\right]\right]^{C_T}} \tag{2.18}$$

where C_T is the total capacitance. Using the calculus of variations with the Lagragian multiplier technique with the Lagrangian multiplier from (2.12) and solving for λ gives the Lagragian expression

$$\lambda = \frac{r}{\left[2N\left[\pi\left[\sqrt{N^2 r(4\mu_o \ln(2)+\mu_o \ln(r)-\mu_o \ln(a)-2\mu_o+\alpha}\right]\right]\right]}, \tag{2.19}$$

and substituting λ into (2.12) and solving for N yields

$$N = \frac{\frac{1}{2}\left(\mu_o \ln\left(16\frac{r}{a}\right)\mu_o+\alpha\right)Br}{\left[I\left[\gamma\left(\mu_o \ln\left(16\frac{r}{a}\right)-2\mu_o+\alpha\right)\right]\right]} \times \sqrt{\frac{4\mu_o \ln(2)+\mu_o \ln(r)-\mu_o \ln(a)-2\mu_o+\alpha}{\left(\mu_o \ln\left(16\frac{r}{a}\right)-2\mu_o+\alpha\right)}}. \tag{2.20}$$

Solving (2.20) calculates the minimum number of turns required in order to build the optimal Helmholtz coil based on the constraints given. A common closed form solution for the B-field produced by a series-driven system of two identical coils can be seen in (2.21) [1]:

$$B_z = \frac{\mu_o N I r^2}{2}\left[\frac{1}{(z^2+r^2)^{3/2}+\left((d-z)^2+r^2\right)^{3/2}}\right], \tag{2.21}$$

where:

B_z = Magnetic field along the z-axis of the coil, Tesla

I = Input current to the coil, amperes

z = distance along the common axis, m

d = coil separation, m

For a Helmholtz coil configuration where the separation between the two coils is equal to the radius of the coils, and assuming the device under test is being measured

at the center volume of the coil an equal distance from each coil pairing, (2.21) can be simplified as

$$B = \frac{\gamma N I}{r},$$

(2.22)

where γ is the constant value given the parameters of an ideal Helmholtz coil (8.99×10^{-7}). The derivative of the magnetic field with respect to r and N yields

$$\frac{\partial B}{\partial r} = -\gamma N \frac{1}{r^2}$$

(2.23)

and

$$\frac{\partial B}{\partial N} = \gamma \frac{1}{r}.$$

(2.24)

Determining the electrical and physical parameters of the Helmholtz coil can sometimes be difficult depending on the constraints used. Certain parameters may need to be sacrificed such as field strength in order to get the required radius or optimal number of turns. Using the constraint equations modeled by Dr. Anderson [1] is a sound approach when designing a Helmholtz coil.

2.3.2 Transverse Electromagnetic (TEM) Cell.

The transverse electromagnetic (TEM) transmission cell was first introduced by Myron L. Crawford at the National Bureau of Standards in 1973 [5]. In 1974, Crawford realized that the electronic or electromechanical systems in the open systems would affect the level and number of potential interfering signals. For this reason, he presented the TEM cell for establishing uniform electromagnetic fields in a shielded environment [6]. It operates at broad band frequency, which is restricted by the waveguide multimode frequency associated with the cell size. Crawford designed the TEM cell to operate as a 50 ohm impedance-matched system. It consists of a

rectangular coaxial transmission section tapered with coaxial connectors on the both ends, as shown in Figure 2.2.

Figure 2.2:   CC-105SEXX TEM Cell

Crawford's TEM cell design maximizes usable test cross sectional area, maximizes upper useful frequency limit, minimizes cell impedance mismatch and thus voltage standing wave, and maximizes uniformity of EM field pattern characteristic of the cell [3]. The IFI CC-105 series TEM cell used for the measurements of the B-Dot sensors is discussed in the following chapter.

2.4   *Magnetic Field Sensing: Theory Behind B-Dot Sensors*

Magnetic field sensors, also known as B-Dot sensors, consist of a loop of conducting material. When an electromagnetic plane wave is incident on the conducting loop, an open-circuit voltage develops across the loop terminals [2]. Figure 2.3 is an example of an incident wave acting on a single loop of conducting wire where the voltage out can be detected between terminals 1 and 2.

The term B-Dot comes from the mathematical expression for the notation for the first time derivative of the magnetic field, $\dot{B} = dB/dt$. The voltage out across terminals 1 and 2 can be expressed using Faraday's law (2.10). As can be seen, the equivalent area of the loop and the time derivative of the B-field make-up the output voltage across the terminals.
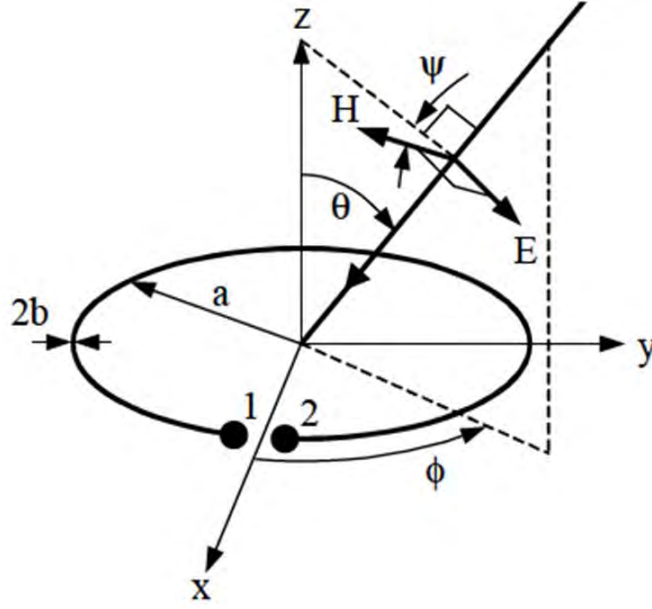
Figure 2.3:   Plane Wave Incident on Loop

The single strand loop described here is used to explain the theory behind magnetic field sensors. The B-Dot sensor used during this research is a bit more complex. Figure 1.3 shows the wiring diagram of the MGL-S8A B-Dot sensor designed by EG&G Incorporated in the mid 1970's [12]. The diagram in Figure 1.1 shows where the two ends are connected to a ground plane and the apex of the half cylinder is the center conductor.The loop formed by the half cylinder and ground plane is interrupted with two gaps, each of which develops a voltage of V/2. This multigap structure aids in the cancellation of the E-field, averages the signal, and improves the frequency response of the loop. Since each gap produces V/2, the averaged output signal is V/2. Because of this, the effective area of the loop is only one half of the geometric area [12].

2.5   Conclusion

Understanding the Poynting vector and the related **E** and **H** fields help to build a foundation behind the basic concepts of EM fields and the theory and operation of devices used to generate EM fields. EM field generators, including the Helmholtz

coil and the TEM cell are two practical methods that can be used to detect magnetic fields and test magnetic field sensors.

III. Methodology

The primary goal of this thesis is to determine if a magnetic field sensor primarily designed to operate at frequencies greater than 5 GHz can be properly simulated and characterized in the 2-32 MHz frequency spectrum at specific angles of interest. Depending on the response of the B-Dot sensors, they could be used as part of a High-Frequency direction finding system on an airborne platform. This chapter will step through the design process used for creating a possible magnetic field generation test bed, Helmholtz coil, in the HF range. Also, a theoretical evaluation will be done determining the magnetic field generated by the Helmholtz coil as well as CST Microwave Studio® computer simulations. The theoretical evaluation will be verified through lab tests, also described in this section. The test results will determine if the Helmholtz coil method is a viable approach to accurately characterize the B-Dot sensors. This chapter also steps through the methodology used to characterize the magnetic field sensors using a TEM cell. The TEM cell is a sound, proven approach to characterizing the B-Dot sensors and will also serve as a control in determining the accuracy of the Helmholtz coil.

3.1 Magnetic Field Generation - Helmholtz Coil

Helmholtz coils are often used for high quality susceptibility testing and sensor calibration purposes. The development and use of a Helmholtz coil should provide an inexpensive method to test magnetic field sensor. The coil should be capable of providing a relatively uniform magnetic field at the center volume of the cylindrically shaped coil. The optimal design of a Helmholtz coil depends upon maximizing some physical quantities while minimizing others. This section describes the methods used in determining the appropriate dimensions and electrical characteristics required in order to create a Helmholtz coil that is capable of stable operation from 2-32 MHz. Theoretical results, preliminary inductance measurements and CST Microwave Studio® simulations are also included in this section.

3.1.1 Determining Physical Parameters and Electrical Characteristics.

The approach used in determining the physical parameters and electrical characteristics of the Helmholtz coil are modeled from the techniques used by Dr. Theodore Anderson in his design of a Helmholtz coil for susceptibility testing using variational calculus and experimental verification [1]. Determining the constraints of the Helmholtz coil in order to achieve optimal parameters is the number one priority. First, the coil is required to be practical in size. Ideally, a design that enables the coil to be transported and stored where it does not take up a lot of space. This requirement, as well as being inexpensive, is the main idea behind building an in-house magnetic field generator used for HF magnetic field sensor testing./

Other constraints to consider when building the Helmholtz coil are the electrical characteristics, specifically inductance and self resonance. The ideal Helmholtz coil design would be to push the resonant frequency beyond the highest frequency of interest (32 MHz) in order to generate a steady field within the volume of the Helmholtz coil. Equation (2.14) shows the theoretical approach used when determining the resonant frequency. As can be seen, in order to increase the resonant frequency, the coil inductance needs to be minimized. Equations (2.15)and (2.16) show the series and mutual inductance through the coil. Another approach used to increase the coil resonant frequency is to reduce the coil capacitance as much as possible; however, since accurate lumped parameter approximations for coil capacitance do not exist for coils with more than a few turns [8], the focus for this coil design is to minimize total inductance. Although the Helmholtz coil parasitic capacitance cannot be directly reduced, decreasing the series inductance, especially by reducing the number of turns, helps to reduce the parasitic capacitance generated by the coil windings. Equations (2.15) and (2.16) serve as a good starting point to determine the physical parameters of the coil. Another important constraint to consider is maximizing the the magnetic field. However, due to the more important inductance and resonant frequency constraints and the maximum output voltage (1 V_{pp}) of the Tektronix arbitrary waveform generator AWG7102 used during this test, maximizing the magnetic field is not a primary

concern as long as any signal being detected is 6 dBm above the surrounding noise floor.

Table 3.1 depicts four inductance values for the Helmholtz coil given a radius of 0.105 meters and a wire bundle cross section of 2.053 mm, 12 gauge wire (Figure 3.1 shows the Helmholtz coil used in this experiment). The parameters decided on for the Helmholtz coil were calculated using the Lagrangian approach, but available material and optimal size were the primary factors which resulted in the design used in this research.

Figure 3.1:   1-Turn Helmholtz Coil

Table 3.1:   Calculated Helmholtz Coil Inductance Values

Turns	Series Inductance (henries)	Mutual Inductance (henries)	Total Inductance (henries)
1	6.21E-07	5.19E-08	1.35E-06
2	2.49E-06	2.07E-07	5.39E-06
4	9.94E-06	8.30E-07	2.15E-05
40	9.94E-04	8.30E-05	2.15E-03

The radius and wire size chosen to build the Helmholtz coil can change depending on necessity; however, the radius and wire size parameters given above will be used throughout this process. As seen in Table 3.1, the 1-turn Helmholtz coil has the

smallest inductance value which should have a high resonance frequency, thus providing a steady field within the coil for the desired bandwidth. Although the 1-turn Helmholtz coil does not produce the largest amplitude field, it is the best design in order to reduce any parasitic capacitance. Despite the small magnetic field, it was experimentally determined that the magnetic field generated was still large enough to be detected by the B-Dot sensors. This coil design will be used to determine all the following parameters.

Once the coil inductance has been calculated, the current throughout the coil needs to be determined. Since the coil is an inductor, we can use (3.1)

$$I(t) = \int \frac{V_{peak} \sin(\omega t)}{L} dt = -\frac{V_{peak} \cos(\omega t)}{L\omega} \ (A).$$ (3.1)

The peak voltage used is 0.5 volts (V_{rms}=0.354 volts), ω is the radial frequency corresponding to 2-32 MHz, and L is the inductance given for the 1-turn coil in Table 3.1. It is important to keep in mind the current is a negative value and has been shifted 90 degrees, this will play a roll in the outcome of the expected values. Figure 3.2 shows the current generated through the Helmholtz coil as a function of frequency.

3.1.2   Theoretical Evaluation of Magnetic Field Using Optimal Parameters.

Dr. Anderson's research [8] in the design of a Helmholtz coil for low frequency magnetic field susceptibility testing on military equipment serves as the baseline for determining the parameters and expected output of the Helmholtz coil constructed and used during this research experiment. It is also Dr. Anderson's analytical expressions that are used to predict the magnetic field within the volume of the Helmholtz coil

$$B_z = \frac{\mu_o N I r^2}{2} \left[\frac{1}{\left(z^2 + r^2\right)^{3/2} + \left((d - z)^2 + r^2\right)^{3/2}} \right],$$ (3.2)

25
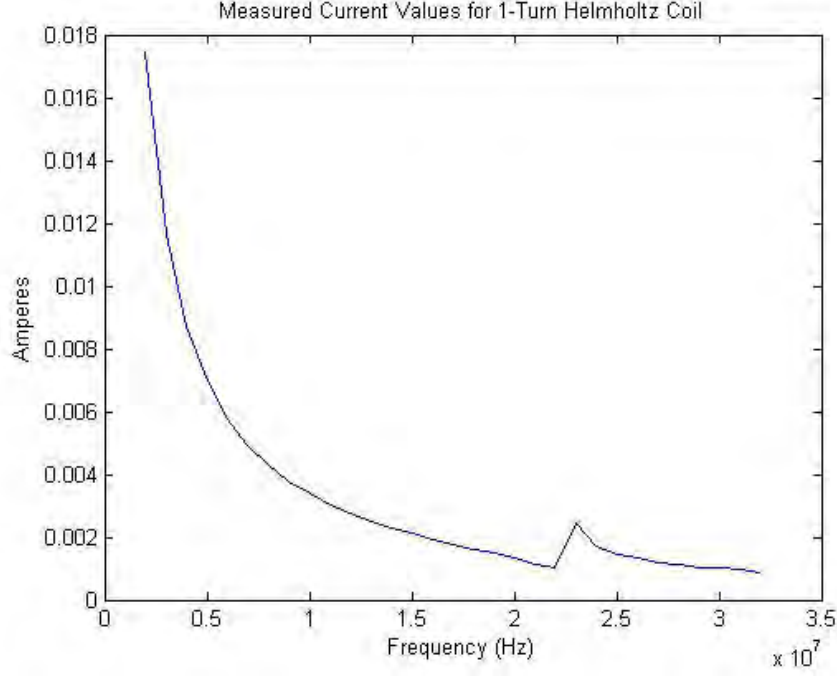
Figure 3.2:   1-Turn Helmholtz Coil Current

where,

B_z= magnetic field along the z-axis of the coil, Tesla

μ_o = permeability of free space, $4\pi x10^{-7}$ (Tesla-m)/A

N = number of turns per coil

r = radius of the coil, m

z = distance along the common axis, m

d = coil separation, m

The maximum input current, I, at the various input frequencies is derived in (3.1) and incorporated into (3.2). The B-field generated by the Helmholtz coil is seen in Figure 3.4 and shows the calculated magnetic field as it changes with frequency. This calculated B-field was derived using mathematical calculations given the optimal parameters needed to design the ideal Helmholtz coil; however, it is necessary before conducting any B-Dot sensor characterization tests to accurately measure the electrical parameters of the Helmholtz coil. Measuring the actual inductance is key when determining the input drive current and ultimately the expected magnetic field

26

generated within the volume of the coil. This measurement was done with the help of Dr. Lorenzo LoMonte at AFRL. The Agilent N5230A PNA-L Network Analyzer was used to determine the inductance through three similar coils, each with a different number of turns on each side, 1-turn, 2-turn, and 4-turns per side. The inductance measured through the 1-Turn Helmholtz coil is seen in Figure 3.3.
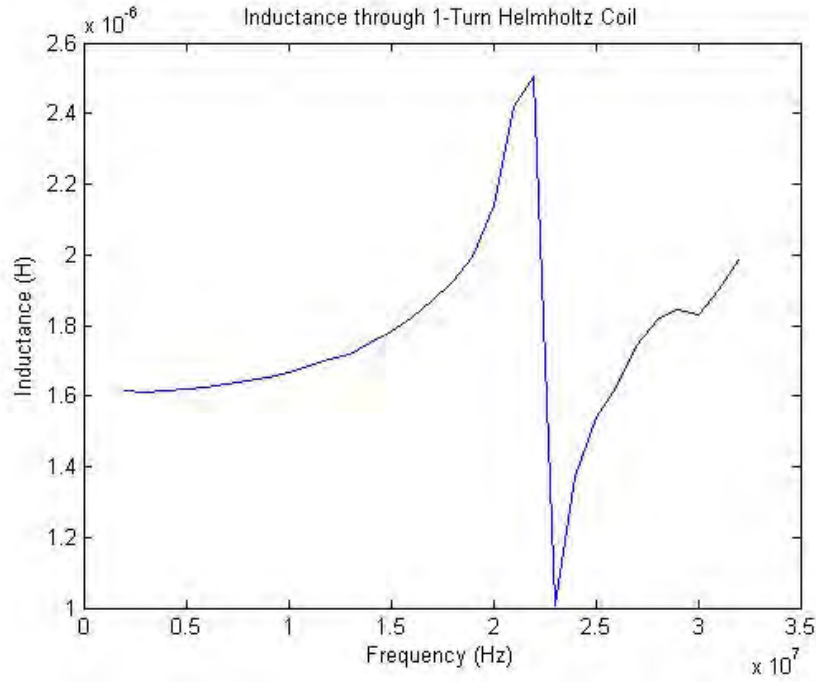
Figure 3.3:   Measured Inductance - 1-Turn Helmholtz Coil from 2-32 MHz

Once accurate inductance values are measured, new measured input current values can be calculated using (3.1). Also, an accurate depiction of the actual magnetic field generated through the volume of the Helmholtz coil using (3.2) can be made. Along with the analytic magnetic field calculated using the calculated inductance values, Figure 3.4 also shows the magnetic field expected by the Helmholtz coil, using the measured inductance values, these values can be found in Appendix B.

Figure 3.4 depicts the magnetic field generated by the Helmholtz coil using the measured inductance values compared to the magnetic field generated by the coil using the calculated inductance values. Also shown in Figure 3.4 is the CST simulated B-field which will be discussed later.
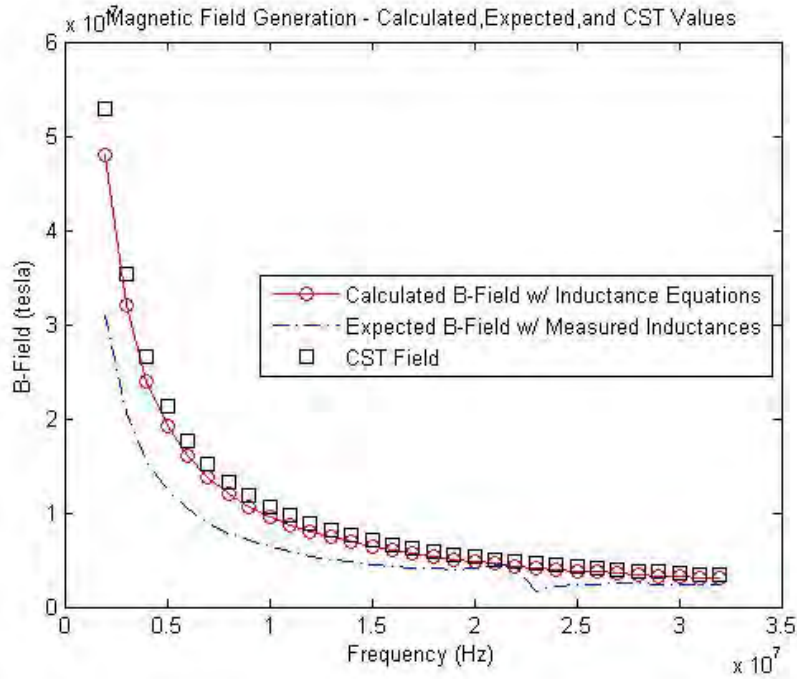
Figure 3.4:   Magnetic Field - Calculated, Measured and CST Values

The expected magnetic field shown in Figure 3.4 will be used as the field acting on the B-Dot sensor during the characterization test.

3.1.3   CST Microwave Studio Simulations.

Computer simulations for the Helmholtz coil using the CST Microwave Studio®, Figure 3.5, show the magnitude and the expected uniformity of the H-field in the center volume of the Helmholtz coil.

Figure 3.4 compares the calculated and measured Helmholtz coil B-fields to the B-field simulation of the CST Microwave Studio® models from 2-32 MHz. As can be seen, the B-field simulation of the CST Microwave Studio® models compared to the measured and calculated values is larger by 500nT at the lower frequencies and 20nT at the higher frequencies. This is due to the slightly larger input voltage used during the simulations (1.5 V_{pp}) as opposed to the 1 V_{rms} value used in the calculations. Also, the simulation is using the optimal inductance value of 1.3μH throughout causing the slightly higher field values.

28
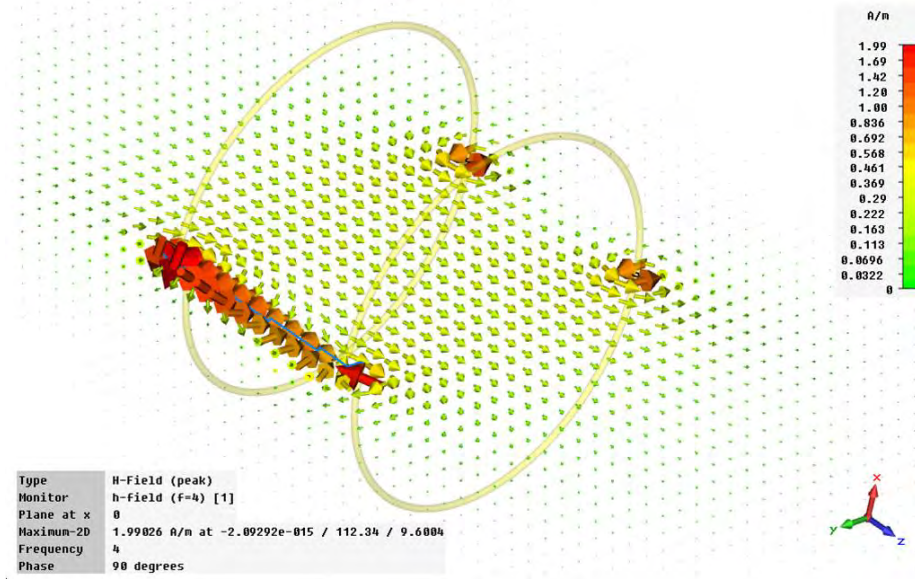
Figure 3.5:   CST H-field Generated by Helmholtz Coil - 4 MHz

3.2   Magnetic Field Generation - TEM Cell

Another method used for testing magnetic field sensors is the transverse electromagnetic (TEM) cell. The TEM cell magnetic field test in this research will be used as a parallel approach to the Helmholtz coil to characterize the B-Dot sensors. It will also serve as a control to aid in the verification of the Helmholtz coil. TEM cells can be used for a variety of measurements, including susceptibility testing, emissions testing, and sensor calibration to name a few. The IFI-CC105 Series TEM cell (see Figure 2.2) used in this research provides efficient field generation from DC to 1 GHz. The cell consist of a rectangular transmission line operating in the TEM mode. The cell is tapered at each end to a transition section that matches to a 50-ohm N-type coaxial jack. Size and precision design of the CC series allow for accurate maintenance and measurement of E-field levels (within 1.0 dB on most models) without antennas. The geometry of the cell combined with its well maintained impedance minimizes undesirable resonance effects. In addition, the typical VSWR is less than 1.25 to 1 [15].

3.2.1   Determining Physical Parameters and Electrical Characteristics.

29

Before calculating the expected magnetic field inside the TEM cell, it is important to know the physical parameters of the TEM cell. Table 3.2 gives the dimensions of the CC-105SEXX, including the septum height, which will be used to calculate the electric field generated within the TEM cell.

Table 3.2:   CC-105SEXX TEM Cell Parameters

DC to Maximum Frequency 1 GHz							
Maximum Test Object Size (inches)			Outside Dimensions (inches)			Septum Height	
Length	Depth	Height	Length	Depth	Height	Inches	Meters
4.7	4.7	2.3	34.3	16	16	7.1	0.18

The electric field generated inside the chamber may be calculated from the expression:

$$E = \frac{V_{rms}}{D} \; (V/m).$$
(3.3)

Equation (3.3) is found in the IFI CC-105 Series TEM cell specification sheet [15]. D represents the distance from the top of the TEM cell to the center, also referred to as the septum height of the TEM cell (0.18 m). The V_{rms} value is the input voltage to the TEM cell. Equation (3.4) is used to convert the input power to the input rms voltage

$$V_{rms} = \sqrt{\frac{10^{(P_{in}/10)} \times Z}{1000}} \; (V),$$
(3.4)

where Z is the TEM cell impedance (50 ohms) and the input power is in dBm from the signal generator [11]. Once the E-field is calculated, the B-field is found by

$$B = \frac{E}{c} \; (T),$$
(3.5)

where E is the electric field calculated in (3.3) and c is the speed of light in a vacuum. The equations defined above help to determine the magnetic field acting on the B-Dot

sensor in the center of the TEM cell. The theoretical magnetic field generated by the TEM cell using a 4 dBm input can be found in Appendix A.

3.3 B-Dot Sensor Characterization

This section describes the two approaches used in the the characterization of the URS and Prodyn MGL-S8A B-Dot sensors. These two characterization approaches, using TEM cell and Helmholtz coil, are conducted in a similar manner. Results will be compared to theoretical predictions, as well as computer simulations.

The MGL-S8A B-Dot sensors are half-cylinder loops mounted on conducting ground plates to measure the time-rate of change of incident magnetic fields [12]. The sensor produces a voltage output in response to a time variant magnetic field, B-field, input. The two different sensors, which are produced by URS and Prodyn, two New Mexico based companies, are the focal point of this research and will serve as the devices under test (DUT) for the 2-32 MHz HF sensor characterization testing. The Prodyn (see Figure 1.1) and URS sensors are based on the same design developed by AFWL in 1975 [12]. Sensor specifications and dimensions are presented in Table 3.3 and Figure 3.6. The test approach for the TEM cell and Helmholtz coil B-Dot sensor HF characterization test are presented in this section. Table 3.3 presents a description and technical characteristics of the MGL-S8A B-Dot sensor device under test to include response time, maximum voltage out, and device parameters. This section explains the objectives of the B-Dot sensor characterization test, the scope of the test, and an inventory of the various resources needed to complete the test (including personnel, hardware, and software). Theoretical calculations and computer simulated results have been compiled which illustrate the expected magnetic field generated by the TEM cell and Helmholtz coil and the expected values from the B-Dot sensor in response to the magnetic field.

The objective of characterizing the MGL-S8A B-Dot sensor at HF is to determine the sensor voltage out and power out response from 2-32 MHz at azimuthal angles of -90, -45, 0, 45, and 90 degrees as depicted in Figure 3.7. The frequency

31
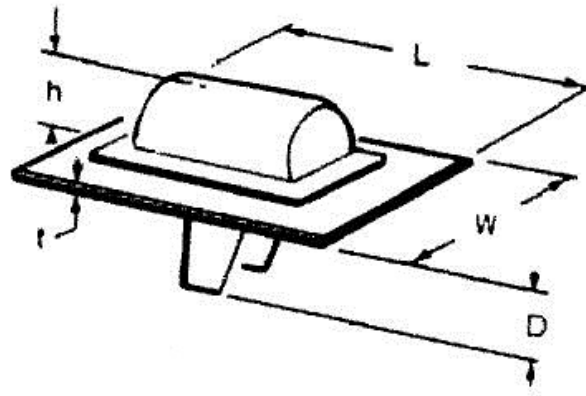
Figure 3.6:   MGL-S8A B-Dot Sensor Diagram

response and angular response measurements will subsequently be converted into the magnetic field (Tesla) and evaluated to characterize sensor HF magnetic field detection capability. Results from the B-Dot sensor HF characterization test will be compared to theoretical results and will aid in determining the feasibility of using the MGL-S8A B-Dot sensors for magnetic field direction finding purposes.
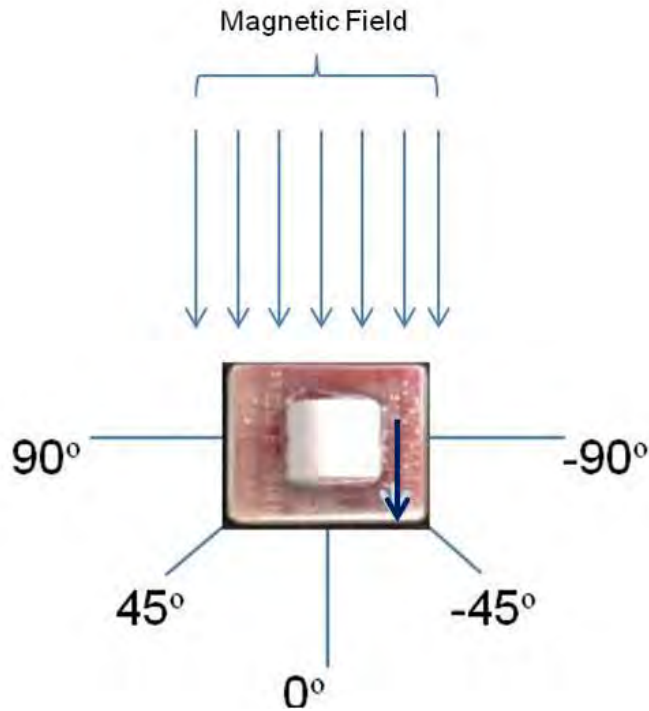
Figure 3.7:   Sensor Orientation w.r.t. B-field

Table 3.3:   MGL-S8A B-Dot Sensor Specifications

Parameter	MGL-8
A_{eq} (m^2)	$1x10^{-5}$
Frequency Response (3 dB Point)	< 5GHz
Risetime ($_{Tr10-90}$)	< 0.05 ns
Maximum Output (peak)	150 V
Maximum Field Change	$1.5x10^7$ (Tesla/sec)
Output Connector	Female SMA
Mass	15 g
Dimensions (cm)	
L	2.54
W	2.54
h	0.6
T	0.1
D	0.7

The two B-Dot sensors characterized during the TEM cell and Helmholtz coil test are:

- Prodyn MGL-S8A B-Dot Sensor, Serial Number 61

- URS MGL-S8A B-Dot Sensor, Serial Number 61

Test results from each method and the CST Microwave Studio® computer simulated results will be analyzed and compared in the following chapter.

3.3.1   B-Dot Sensor Characterization - TEM Cell.

The TEM cell is one approach to the B-Dot sensors characterization test because it establishes a uniform electromagnetic field within a shielded environment. The results of the TEM cell test are considered to be more accurate and will be used to supplement the characterization of the B-Dot sensors as well as help authenticate the Helmholtz coil.

3.3.1.1   TEM Cell Test Resources.

The TEM cell required to conduct the characterization test is not available at AFIT or AFRL, so the SPAWAR Systems Center Pacific CERF facility in Point Loma

San Diego provided insight to the test as well the necessary equipment needed for the test. Below is a list of the test equipment provided by SPAWAR to complete the characterization test:

- Aglient E8257D PSG Analog Signal Generator

- Aglient E4440A PSA Spectrum Analyzer

- All associated cables and required calibration equipment

- CC-105SEXX TEM Cell

The CC series TEM cell used to generate the constant magnetic field is shown in Figure 2.2, with technical parameters presented in Table 3.2

The MATLAB® R2010a software suite is used for pre and post processing analysis which includes the theoretical/expected voltage out, power out, and magnetic field values generated by the TEM cell. Also, CST Microwave Studio® is used to model the B-Dot sensors and provide simulated output results.

3.3.1.2   TEM Cell Theoretical Evaluation.

The MGL-S8A B-Dot sensor theoretical evaluations are presented in Appendix A and include the B-field generated by the TEM cell, the voltage out of the B-Dot sensor, and the equivalent power out at azimuthal angles of -90, -45, 0, 45, and 90 degrees.

Understanding how the TEM cell works is important to help define the magnetic field generated inside the cell in order to properly measure the response of the B-Dot sensors. The first step is to calculate the electric field inside the TEM cell (see (3.3)). Input voltage values are calculated given the 4 dBm input from the Aglient E8257D PSG Analog Signal Generator. Once the E-field is calculated it can be used in ((3.5) to calculate the B-field acting on the B-Dot sensor inside the TEM cell.

Once the B-field generated by the TEM cell is calculated, it is used as the input the the MGL-S8A B-Dot sensor. Equation (3.6) incorporates the B-field calculated in (3.5), A_{eq} is the equivalent area of the B-Dot sensor (10^{-5} m^2, ω is the radial

frequency input from the signal generator, and θ is the sensor orientation with respect to the magnetic field [12] [7],

$$V_o = BA_{eq}\omega\cos(\theta) \ (V). \tag{3.6}$$

The voltage out results and the converted power out values are given in Appendix A, the B-Dot sensor expected power out readings for the 0 and 45 degree orientation can be seen in Figure 3.8.
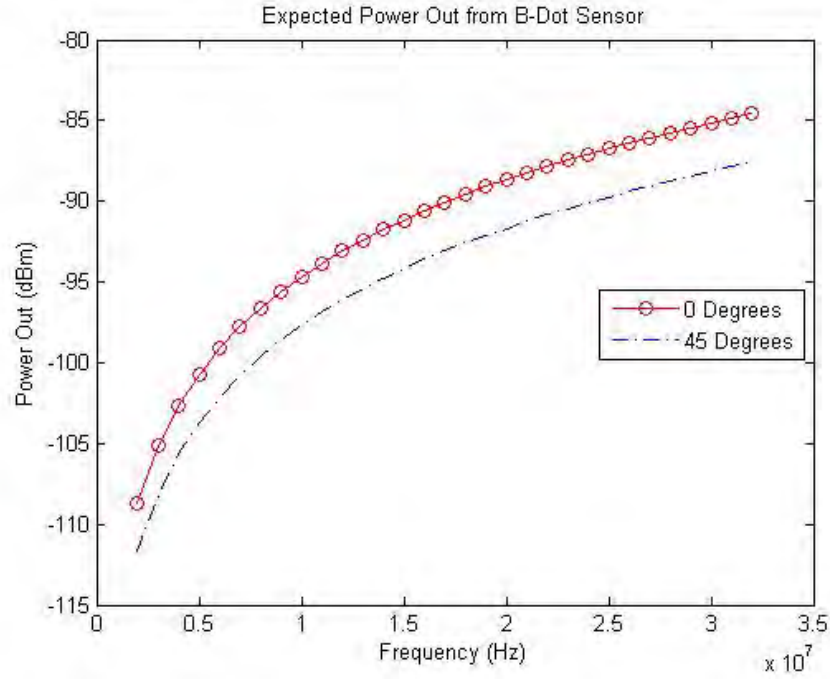
Figure 3.8: B-Dot Sensor Expected Power Out with 4 dBm Input Power

3.3.1.3 TEM Cell Test Process.

To ensure accurate results, it is import to calibrate the support equipment used, including the signal generator, spectrum analyzer, and the TEM cell. The SPAWAR test team offered to assist and verify all equipment is setup and operating accurately in order to precision measurements. Another important factor to achieve accurate test results is to use the same cables during the entire test process. Cable loss will

be measured and incorporated into the final measurement results. Once calibration is complete, the B-Dot sensor characterization test will be set up according to Figure 3.9.
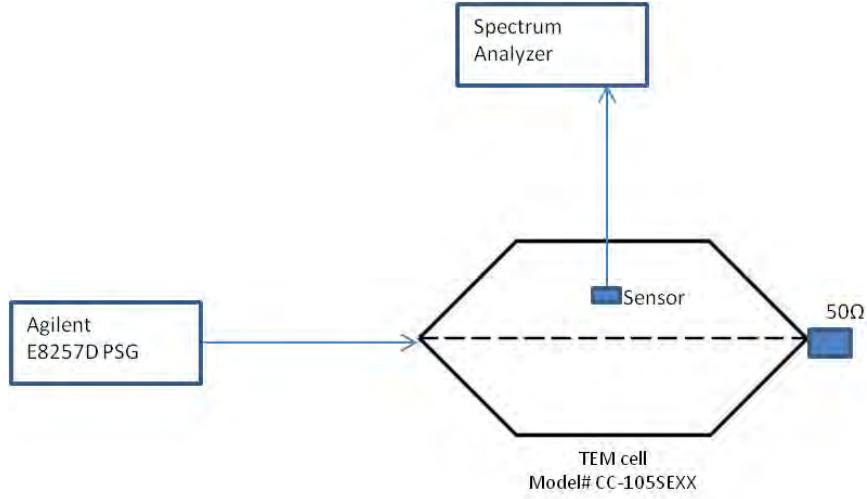
Figure 3.9:   MGL-S8A B-Dot Sensor Characterization Test Set-up

The input power to the TEM cell will be set for 4 dBm (1 V_{pp}) for all test measurements. The sensor characterization test will be completed first with the Prodyn sensor followed by the URS sensor. The first set of measurements will be taken with the sensor oriented at 0 degrees with respect to the magnetic field generated by the TEM cell. Once the sensor is oriented correctly, measurements will be taken starting at 2 MHz and ending at 32 MHz in 1 MHz increments. All test points, including power out in dBm and the integrated average noise floor, will be annotated. Once the first set of test points are recorded at the 0 degree orientation, the sensor will be orientated at -45 degrees, as depicted in Figure 3.10.

The power out and noise floor will be recorded at this orientation for all frequencies from 2-32 MHz. The test will continue in this manner for all azimuthal angles (-90, -45, 0, 45, and 90 degrees). Once the Prodyn sensor has been measured at all frequencies and all orientations, the URS sensor will be measured in the same manner.

3.3.2   B-Dot Sensor Characterization - Helmholtz Coil.
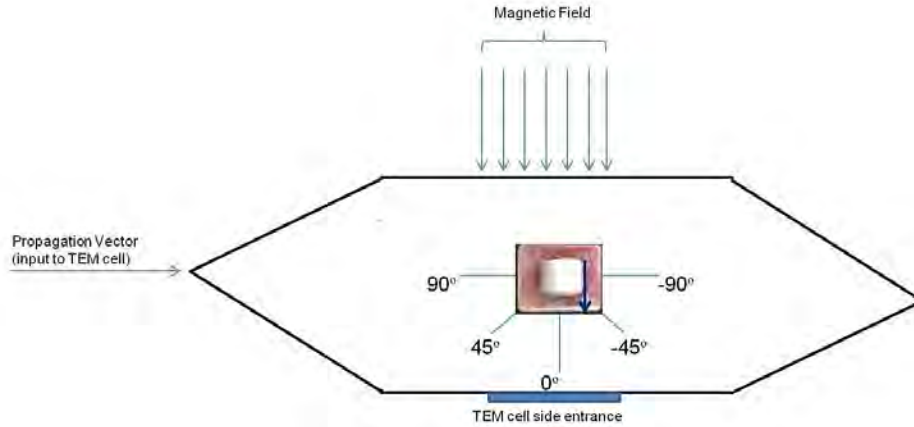
Figure 3.10:   TEM Cell Sensor Orientation w.r.t. B-field

The Helmholtz coil is the second approach used to characterize the B-Dot sensors. The coil design should produce a relatively uniform magnetic field in the center volume of the cylinder through the entire frequency range in which the test is to be conducted. Along with test equipment already on-hand at AFIT, the Helmholtz coil can likely be used as an inexpensive, in-house, magnetic field generator used for sensor characterization in the HF range. Having this capability will decrease dependance on outside organizations and allow for further verification testing of the B-Dot sensors.

3.3.2.1   Helmholtz Coil Test Resources.

All equipment required to conduct the B-Dot sensor Helmholtz coil characterization test is on-hand at AFIT and AFRL. Dr. Lorenzo LoMonte from AFRL provided insight to the development of the Helmholtz coil and also assisted in the inductance measurements of the coil. Below is a list of equipment used to measure the inductance of the Helmholtz coil and characterize the B-Dot sensors

- Agilent N5230A PNA-L Network Analyzer

- Tektronix AWG7102 Arbitrary Waveform Generator

- Agilent E4440A PSA Spectrum Analyzer

- All associated cables and required calibration equipment

- Helmholtz coil

The Helmholtz coil was constructed from an 8" diameter Quik-Tube ridged fiber building form tube. The tube consist of high-quality fiber laminated with an adhesive. The tube provides a rigid structure in which to form the coil, and the materials of the tube have a high permeability, which allows the magnetic field to radiate evenly. The wire used for the coil turns is 12-gauge insulated, solid core copper wire. An SMA type connector was soldered to each end of the wire and is used for the input voltage of the Helmholtz coil. Figure 3.1 is the 1-turn coil used for the B-Dot sensor characterization test.

Table 3.4 gives the physical parameters of the Helmholtz coil used during the characterization test. These parameters are also used to calculate the expected values of the B-field generated by the coil and the power out from the B-Dot sensors. The sensor location is in the center of the coil volume equally placed between both sets of coils.

Table 3.4: Helmholtz Coil Physical Parameters

Number of Turns	Coil Radius	Distance Between Turns	Sensor Location	Wire Diameter
1	0.105(m)	0.105(m)	0.0525(m)	2.052(mm)

The MATLAB® R2010a software suite is used for pre and post processing analysis including the theoretical/expected voltage out, power out, and magnetic field values generated by the Helmholtz coil. Also, CST Microwave Studio® is used to model the field generated by the Helmholtz coil and provides simulated results.

3.3.2.2 Helmholtz Coil Theoretical Evaluation.

The MGL-S8A B-Dot sensor theoretical evaluations are presented in Appendix B and include the B-field generated by the Helmholtz coil, the voltage out of the B-Dot sensor, and the equivalent power out at azimuthal angles of -90, -45, 0, 45, and 90 degrees.

Understanding how the Helmholtz coil works is important to help define the magnetic generated inside the coil in order to properly measure the response of the B-Dot sensors. The defining equation used to determine the magnetic field within the coil volume is expressed in (3.2)

Once the B-field generated by the Helmholtz coil is calculated, it is used as the input the the MGL-S8A B-Dot sensor. Equation (3.6) incorporates the B-field calculated in (2.21), A_{eq} is the equivalent area of the B-Dot sensor ($10^{-5}m^2$), ω is the radial frequency input from the signal generator, and θ which is the sensor orientation with respect to the magnetic field [12] [7]. The expected voltage out results and the converted power out values are given in Appendix B. The 0 and 45 degree orientation power out is also seen in Figure 3.11 (the 90 degree plot was excluded because its expected value is small and alters the scale of the plot)
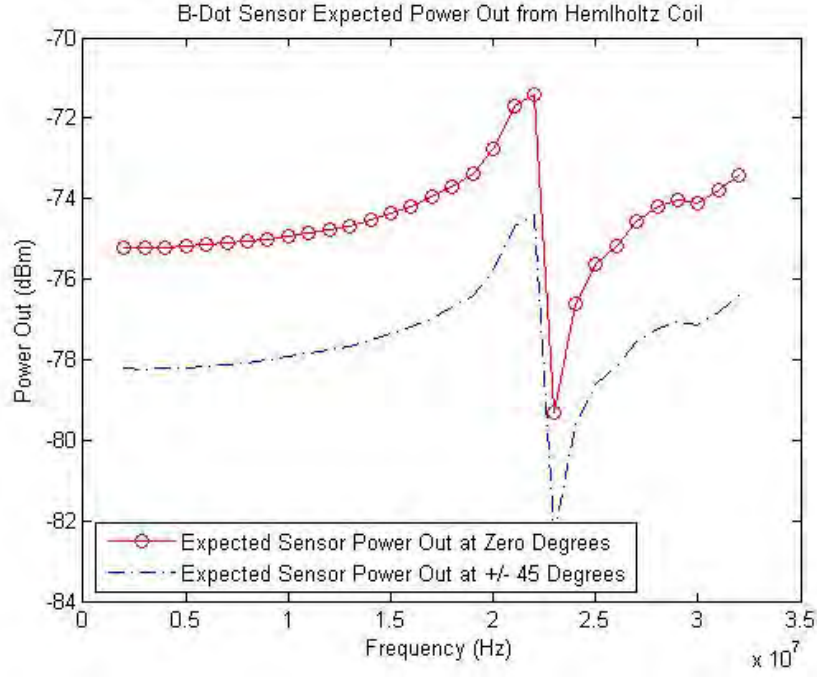
Figure 3.11:   Expected Power Out of B-Dot Sensor at 0 and 45 Degrees

3.3.2.3   Helmholtz Coil Test Process.

39

Calibration of all support equipment, including the arbitrary waveform genera-
tor and spectrum analyzer, is required to ensure accurate results are measured. It is
also important to measure and account for the attenuation loss through the cables.
For accurate results, use the same cables throughout the entire test. Once calibration
is complete and preliminary measurements are taken, the Helmholtz coil B-Dot sensor
characterization test will be set up and oriented according to Figure 3.12.
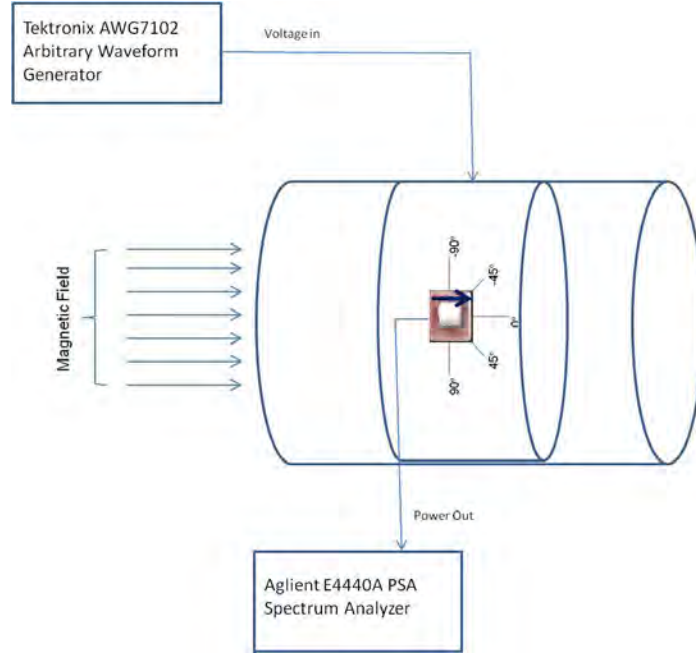
Figure 3.12:   Helmholtz Coil B-Dot Sensor Characterization Test Set-up

The input voltage to the coil is 1 V_{pp} for all test measurements. The sensor
characterization test will be completed first with the Prodyn sensor followed by the
URS sensor. The first set of measurements will be taken with the sensor oriented at
0 degrees with respect to the magnetic field generated by the TEM cell. Once the
sensor is oriented correctly, measurements will be taken starting at 2 MHz and ending
at 32 MHz in 1 MHz increments. All test points, including power out in dBm and
the noise floor, will be annotated. Once the first set of test points are recorded at
the 0 degree orientation, the sensor will be orientated at -45 degrees, as depicted in
Figure 3.12. The power out and noise floor will be recorded at this orientation for all
frequencies from 2-32 MHz. The test will continue in this manner for all azimuthal

angles (-90, -45, 0, 45, and 90 degrees). Once the Prodyn sensor has been measured at all frequencies and all orientations, the URS sensor will be measured in the same manner.

3.3.3 B-Dot Sensor - CST Microwave Studio Simulation.

The CST Microwave Studio® computer simulated expected results of the B-Dot characterization test at different orientations can be seen in Figures 3.13 and 3.14, numerical values are given in Appendix C.
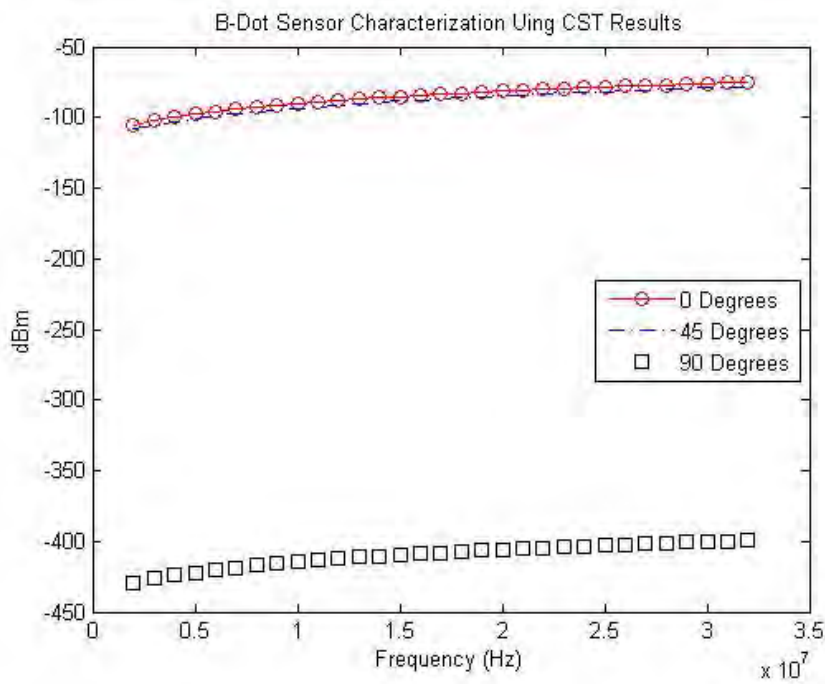
Figure 3.13:   CST Results of B-Dot Characterization at 0, 45, and 90 Degrees

The model constructed in CST Microwave Studio® is based on the Prodyn schematic figure. The results provided in Appendix C are the sensor radiation efficiency (in dB), total efficiency (in dB), and sensor directivity (in dBi). Using these results, the power out can be calculated using

$$Power\ Out\ (dBm) = 10\log{(G)}, \tag{3.7}$$

41
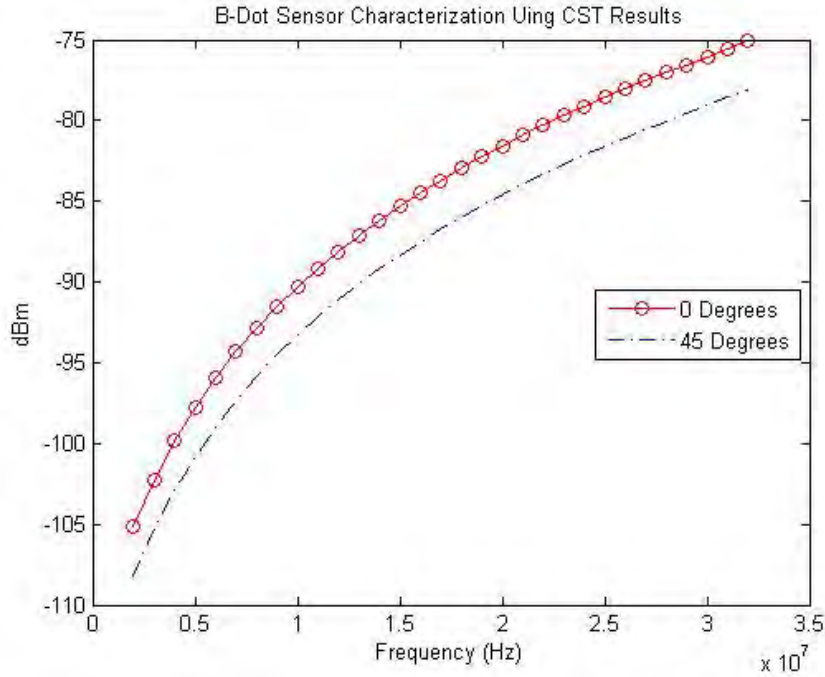
Figure 3.14:   CST Results of B-Dot Characterization at 0 and 45 Degrees

where G is the Gain of the sensor. The gain is then calculated as

$$G\left(dBm\right) = D * \varepsilon_r, \tag{3.8}$$

where ε_r is the radiation efficiency given in the CST Microwave Studio® results and D is the sensor directivity value given by

$$D = 10^{\left(\frac{dBi}{10}\right)}. \tag{3.9}$$

The dBi value in (3.9) is given in the Appendix C CST Microwave Studio® results. Figure 1.3 is the schematic diagram of the Prodyn sensor which the results were based.

IV. Results

This section analyzes and compares the measured results of both the URS and Prodyn B-Dot sensors using the Helmholtz coil and TEM cell test methods. These results are compared to theoretical values calculated in Chapter III and CST Microwave Studio® simulated results.

4.1 Helmholtz Coil B-Dot Sensor Characterization - Results

One of the main aspects of the research conducted in this thesis is to develop a magnetic field generating system in the HF frequency range to use as an inexpensive, in-house test bed for the purpose of characterizing magnetic field, B-Dot, sensors. The approach decided on and used is the Helmholtz coil. The Helmholtz coil consists of two identical loops each with the same amount of turns. The two coil pairings are separated by a distance equal to the radius of the coil. The separation is important because it creates a uniform field in the center volume of the coil pairing, where the device under test is to be placed. The coils are powered by an input voltage source which allows for a current flow through the coil. The coil is designed so the current flows in the same direction and, ideally, would be equal. However, since the coil being built requires an HF input from 2-32 MHz, and not DC, the constant current flow can be difficult to achieve. Because of this, it is important to calculate and measure the impedance through the coil. In the coil design used, we only account for the inductive reactance, ωL, and we assume any DC resistance is negligible. An ideal design of an AC Helmholtz coil should have a relatively constant inductance, which is needed to keep the field in the center volume of the coil pairing uniform.

This section provides measured values taken with a 1-turn Helmholtz coil with a radius of 0.105 meters using 12 gauge copper wire with a 1 V_{PP} input voltage (see Figure 3.1). This design is used because it provides a near uniform field from 2-20 MHz at which point the field becomes unstable due to a resonant frequency. The 1-turn coil was also chosen because it acts completely as an inductor and is not susceptible to parasitic capacitance as were the coils with multiple turns. B-Dot

43

measured values were taken using two MGL-S8A sensors, manufactured by Prodyn and URS respectively, at azimuthal angles of -90, -45, 0, 45, and 90 degrees from 2-32 MHz. The sensor power out values, in dBm, are compared to theoretical values derived from calculated and measured inductance values and the Helmholtz coil B-field as calculated using (3.2). Figure 4.1 shows the measured B-field results from the Helmholtz coil compared to the calculated, expected, and CST generated fields.
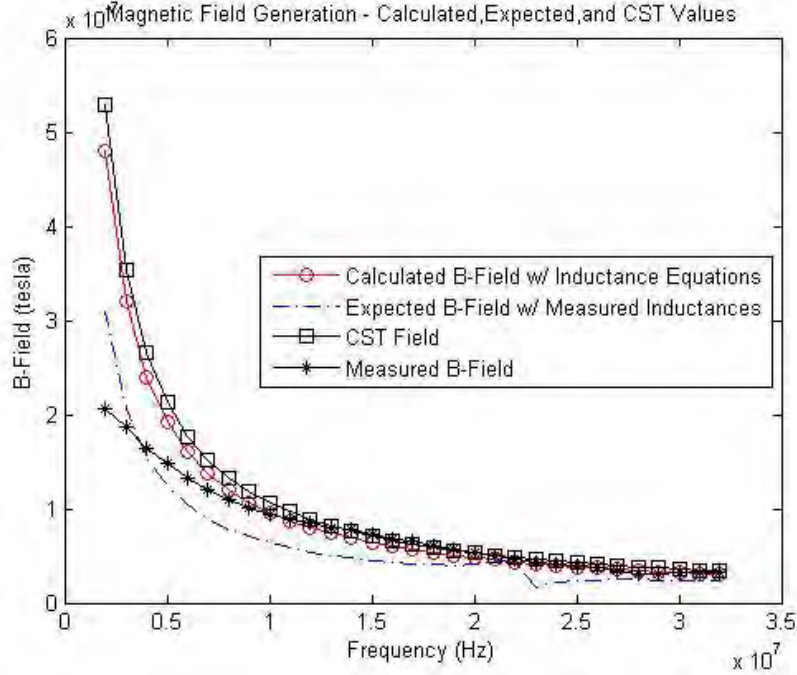
Figure 4.1:   Expected and Measured B-field - Helmholtz Coil

It is not surprising to see the calculated values match the values of the CST results, in fact, the input voltage to the CST simulations was 0.7 V_{pp} higher than the 1 V_{pp} value used in the B-field calculations, which is likely the reason the CST result is slightly higher than the calculated result. Also, the simulated/calculated values show a higher B-field in the lower frequency range, this is due to the ideal low (1.3 μH), steady inductance values calculated. The measured inductance values range from 1.6 to 1.9 μH from 2-20 MHz, at which point, the resonant frequency causes the an instability in the coil's H-field. The measured results shown in Figure 4.1 are better than expected, especially from 8-32 MHz. Although the values measured are

44

close to the expected values, recharacterizing the Helmholtz coil inductance values and determining the permeability of the Quik-Tube used to construct the Helmholtz coil may bring the expected values calculated using the measured coil inductances closer to the calculated and simulated results.

4.1.1 Prodyn B-Dot Sensor Characterization - Helmholtz Coil.

This section provides results for measured values taken using the Prodyn B-Dot sensor at orientations of -90, -45, 0, 45, and 90 degrees with respect to the generated B-field along the z-axis of the Helmholtz coil. The measured values were taken using the Tektronix AWG7102 arbitrary waveform generator with a 1 V_{pp} input voltage from 2-32 MHz. The output power results from the B-Dot sensor, in dBm, were recorded using an Aglient E4440A PSA spectrum analyzer. The average noise floor, which consists of any unwanted signals in the frequency range of interest, was -116.8 dBm. The average noise floor is proportional to the resolution bandwidth setting of the spectrum analyzer, for this test, the resolution bandwidth was set to 100 Hz. This setting resulted in an integrated noise level low enough to be able to detect the signals, especially in the lower frequency ranges. The downside to this setting was the 45 second sweep time needed to measure each signal. The power out and noise floor level at all orientations for the Prodyn sensor Helmholtz coil test can be found in Appendix E. Also note, any signal-to-noise ratio (SNR) value greater than 6 dB is considered a detectable signal. The first set of results seen in Figure 4.2 show all measured values of the Prodyn sensor at all five orientations.

As expected, the sensor has the greatest return at the zero degree orientation with an average value of -72.84 dBm from 2-32 MHz. As the sensor was turned away from the magnetic field in the positive and negative 45 degree directions, the measured power starts to decrease. The average power out in the negative 45 degree direction is -75.78 dBm and -76.67 dBm in the positive 45 degree direction. Also, as can be seen, the measured values at the positive and negative 90 degree orientations are -101.5 dBm and -100.69 dBm respectively.
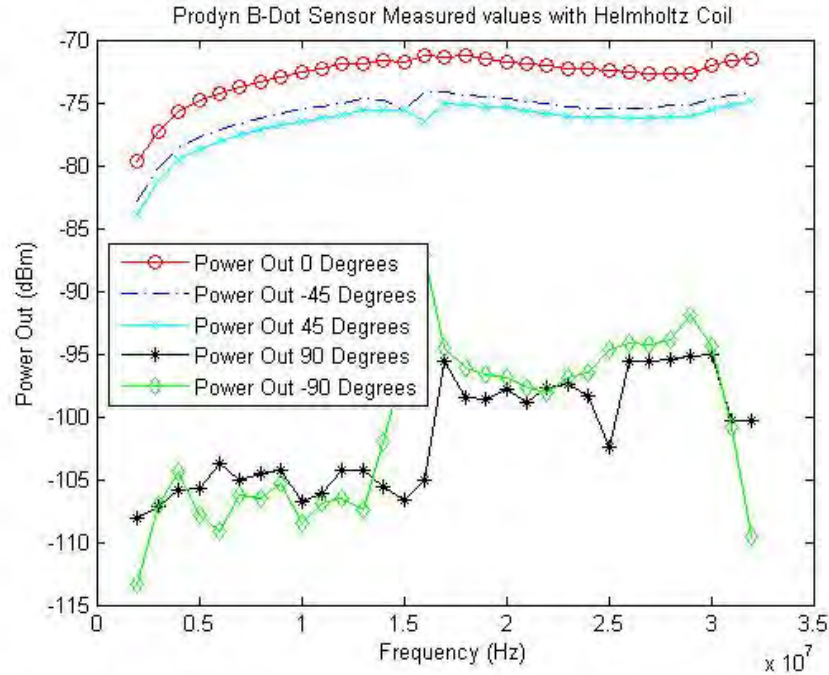
Figure 4.2:   Power Out Results from Prodyn B-Dot Sensor using Helmholtz Coil

These 90 degree results are much higher than expected. In fact, with the B-field generated by the Helmholtz coil, the sensor is detectable from negative 90 to positive 90 degrees, acting somewhat as an omnidirectional antenna (azimuth angles only, elevation angles have not been tested). Although the sensor response is inconsistent at the 90 degree orientations, the signal is likely detectable due to the 3-dimensional design of the sensor. Also seen in Figure 4.2 are two steps, one at 15 MHz for the -45 degree measurement and the other at 16 MHz for the +45 degree measurement. It was first expected that this was due to the sensor positioning accuracy when conducting the test, however, because the URS sensor results (seen later) show the same pattern, it is suspected that the slight asymmetrical design of the sensor as seen by the B-field at angles greater than zero and less than +/- 90 degrees cause the slight frequency shift. Figure 4.3 shows the SNR of the measured values. As can be seen, all measurements with the exception of the -90 degree at 2 MHz measurement are above 6 dB.
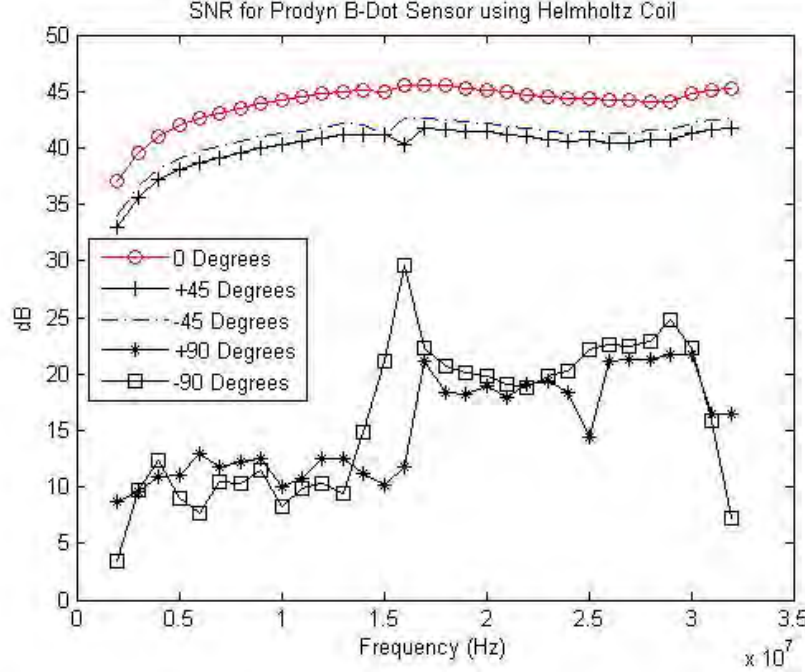
Figure 4.3:   Integrated SNR from Prodyn B-Dot Sensor using Helmholtz Coil

It is important to evaluate the measured results and compare them to the cal-culated values as well as the simulated results. Figures 4.4, 4.5 and 4.6 show the measured results versus the expected and simulation results at -90, -45, 0, 45, and 90 degrees. Before analyzing the results, it is important to understand what the results show, especially the simulations. The two CST simulation results are derived from the Helmholtz coil CST simulation and the B-Dot sensor simulation. It will be seen later (in the TEM cell results) that the CST B-Dot power out follows the expected and measured results from the TEM cell. This is due to a consistent input power level as opposed to a varying input power caused by a dependency on inductive reactance (i.e. radial frequency and inductance). The two CST results shown are simply used as a comparison and an opportunity to explain the results from a consistent input power compared to the input power generated by a coil.

The three results of interest in Figure 4.4 are the measured power out, expected power out, and the CST Helmholtz coil power out. The ideal sensor output power due to a magnetic field generated by a Helmholtz coil is seen in the CST Helmholtz coil

47

B-Dot power out. The reason the flat response is ideal is because of the generated B-field dependency on inductive reactance (ωL). In the case of the Helmholtz coil simulation, the inductance (L) is constant and the ω cancels out (see (3.1 and (3.2)). Due to the cancelation of the radial frequency, the entire voltage out, and ultimately the power out, of the B-Dot sensor becomes a constant. The expected power out results are similar to the CST results. The ω cancels out but the inductance is not constant. In the case of the calculated values here, the inductance goes from 1.6μH to 1.9μH from 2-20 MHz. It was at this point that the coil was determined to become unstable. However, it can be seen that the expected power out levels out at 30-32 MHz, since the inductance levels return to 1.6μH. As can be seen, the measured results range from -79 dBm to -71 dBm; however, the measured results from 4 MHz and up level out significantly. It is expected that the coil inductance characterization has changed and the resonance occurs between 12 and 21 MHz as opposed to the measured inductance values where instability occurred from 20 to 29 MHz. The new inductance values are also expected to be less severe than the originally measured values since any spike is difficult to discern.

The average difference between the the measured and expected values is 1.71 dBm. This is a good result with the exception that the measured results and expected results do not completely follow the same pattern. The next set of results analyzed are the Prodyn B-Dot sensor power out measurements at the positive and negative 45 degree orientations. Figure 4.5 shows the B-Dot sensor measured results using the Helmholtz coil compared to the calculated expected results and the CST B-Dot sensor and Helmholtz coil simulated values.

The positive and negative 45 degree orientation measurements average -76.67 dBm and -75.78 dBm respectively. These results differ by only 0.89 dBm. The results seen at the 45 degree orientations are similar to the zero degree measurements in that the simulated Helmholtz coil power out remains a constant due to the cancelation of the radial frequency and the constant inductance demonstrated with the CST Helmholtz coil simulation. The expected power out shown in Figure 4.5 follows
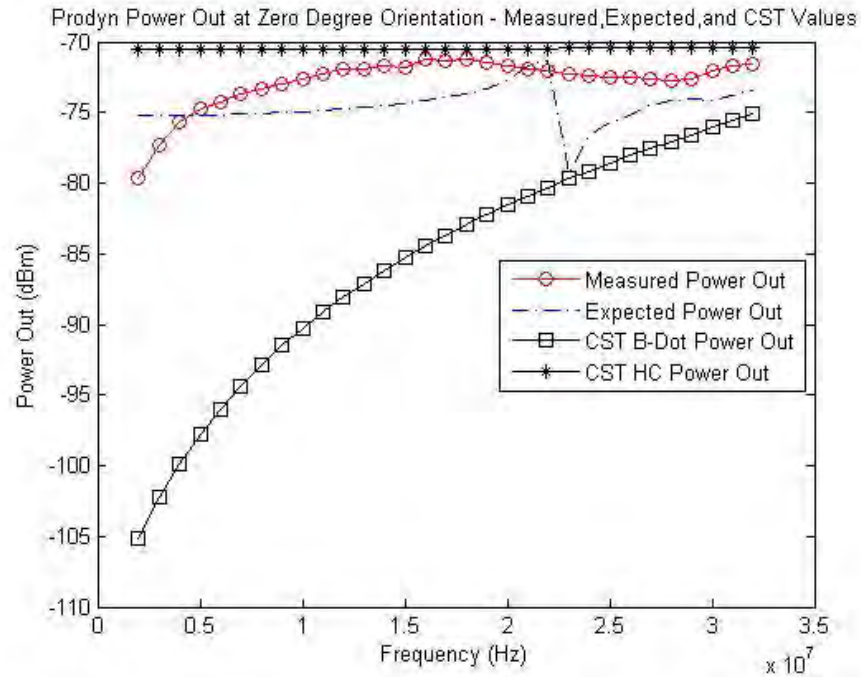
Figure 4.4:   Power Out Results from Prodyn B-Dot Sensor using Helmholtz Coil - Zero Degrees
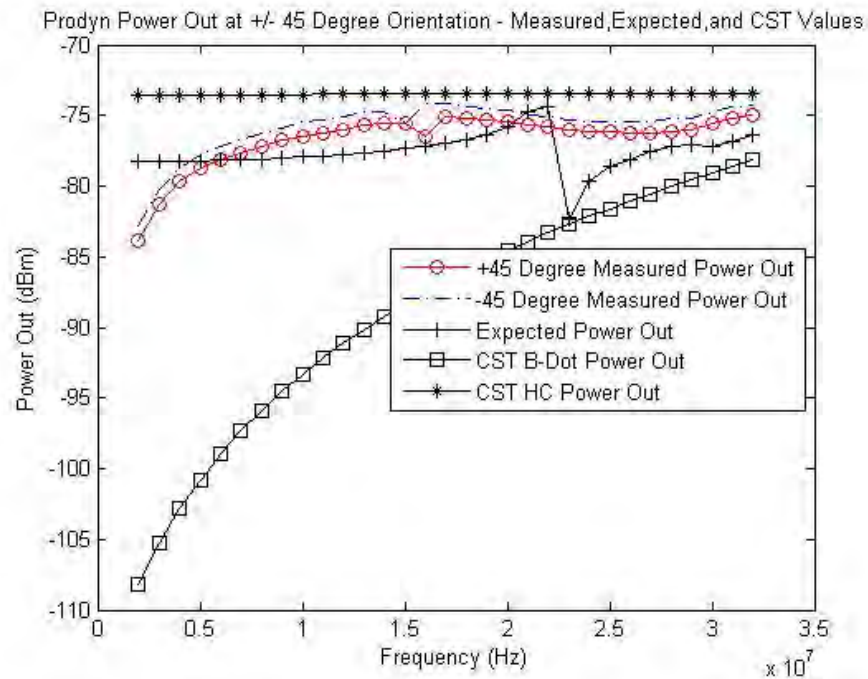
Figure 4.5:   Power Out Results from Prodyn B-Dot Sensor using Helmholtz Coil - +/- 45 Degrees

the same pattern as it did with the zero degree expected value. As noticed earlier, the expected resonant frequency is at the 24 MHz point, whereas the measured value steps at 15 and 16 MHz, the likely location of the coil resonance due to coil modifications. The next set of results analyzed are the Prodyn B-Dot sensor power out measurements at the positive and negative 90 degree orientations. Figure 4.6 shows the B-Dot sensor measured results using the Helmholtz coil compared to the calculated expected results and the CST B-Dot sensor and Helmholtz coil simulated values.
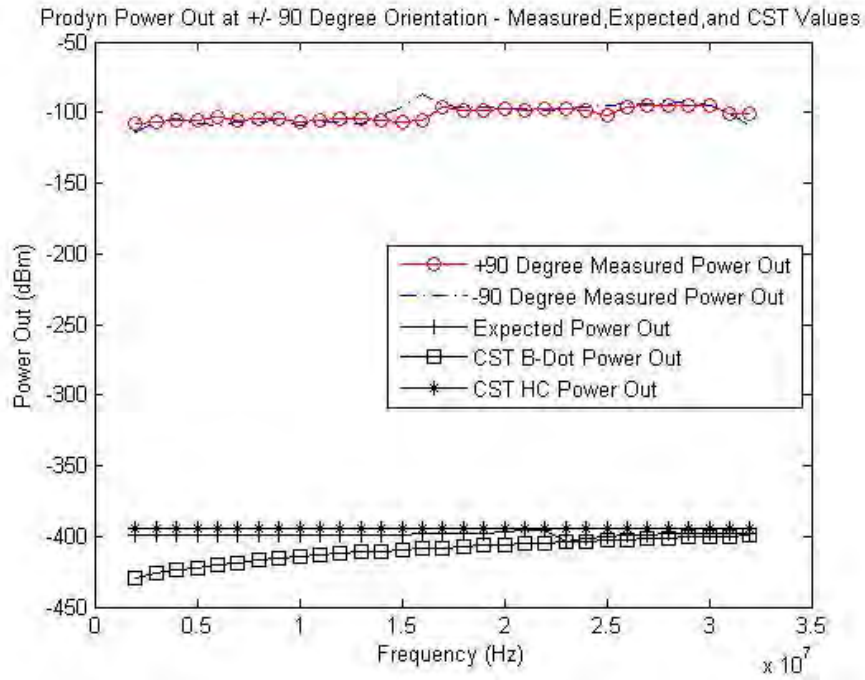
Figure 4.6:   Power Out Results from Prodyn B-Dot Sensor using Helmholtz Coil - +/- 90 Degrees

As Figure 4.6 shows (measured results at positive and negative 90 degrees are better seen in Figure 4.3), there is a signal return from the B-Dot sensor at the two 90 degree orientations. It was initially suspected that due to the cosine θ term in (3.6), the return signal to noise ratio would drop to zero causing an undetectable signal. However, it is believed that because of the 3-dimensional design of the B-Dot sensor, the signal is partially detectable at the 90 degree orientation. Although the

50

90 degree orientation measurements did have a return signal, most of which were above the 6 dB detection threshold, the voltage levels were erratic. Although power levels do decrease as the orientation of the sensor is changed, the difference in the measured values from 0 degrees to -45 degrees and also from 0 degrees to +45 degrees is small and depicts a less angular dependance than predicted and the sensor acts nearly omnidirectional. The omnidirectional behavior of the sensor could likely be a problem when attempting to use it for direction finding purposes. Since the 0 and 45 degree measurements follow a common pattern, it is important to determine where the pattern breaks down. Figure 4.6 also shows the same expected resonance at positive and negative 90 degrees as it did at the 45 degree orientations.

4.1.2 URS B-Dot Sensor Characterization - Helmholtz Coil.

This section provides results for measured values taken using the URS B-Dot sensor at orientations of interest using the Helmholtz coil. The methods and test equipment used for this test were the same as was used for the Prodyn sensor test. The spectrum analyzer resolution bandwidth was set to 100 Hz as it was with the Prodyn test which resulted in the same -116.8 dBm average noise floor. The power out and noise floor level measurements at all orientations for the URS sensor Helmholtz coil test can be found in Appendix D. Recall, a SNR of 6 dB or greater is considered a detectable signal. The following results seen in Figure 4.7 show measured values of the URS sensor at all five orientations.

As expected, the URS sensor values follow the same pattern as the Prodyn sensor. The average power out at the zero degree orientation is -71.76 dBm. The measured values start to decrease as the sensor orientation changes and turns away from the magnetic field. Figure 4.8 shows the SNR of the Prodyn sensor measured values.

The SNR values shown in Figure 4.8 are all well above the 6 dBm signal detection threshold level. Comparisons to the URS sensor and the Prodyn sensor will be made later on in this chapter.
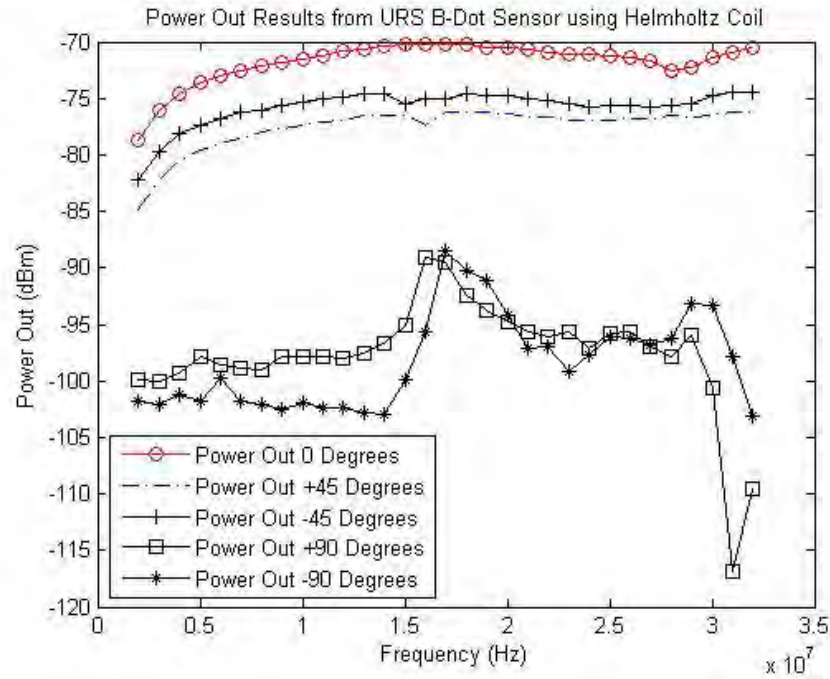
Figure 4.7:   Power Out Results from URS B-Dot Sensor using Helmholtz Coil
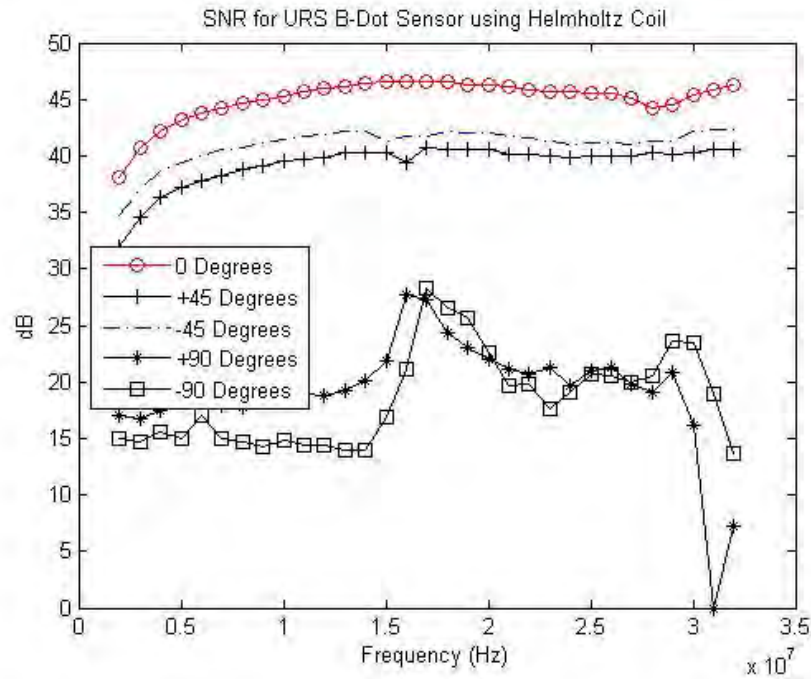
Figure 4.8:   Integrated SNR from URS B-Dot Sensor using Helmholtz Coil

Also shown are the URS sensor measured values at each orientation compared to the expected and simulated values at the given orientations. The average expected value at zero degrees from 2-32 MHz is -74.55 dBm, which differs from the measured value of -71.76 by 2.79 dBm. This difference is slightly higher than the difference measured with the Prodyn sensor. The simulated values in the following plots differ significantly due to the constant B-field used in the B-Dot sensor simulation as opposed to the varying field in the Helmholtz coil simulation. The CST B-Dot power out simulation is similar to the results of the TEM cell test, the CST/TEM comparison will be explored later in this chapter. Figures 4.9, 4.10 and 4.11 show the measured results versus the expected and simulated results.
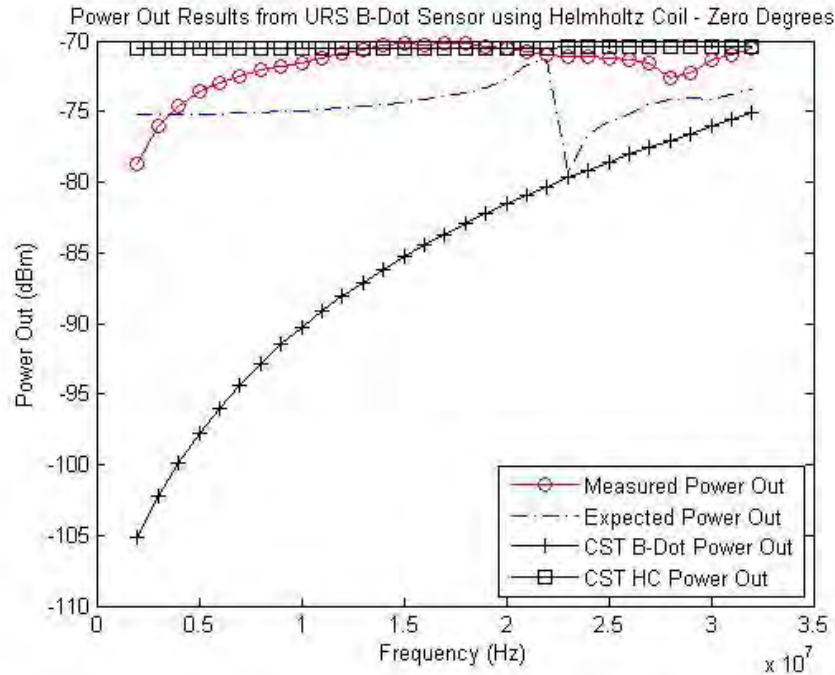
Figure 4.9:   Power Out Results from URS B-Dot Sensor using Helmholtz Coil - Zero Degrees

As can be seen, the URS sensor response is similar to that of the Prodyn sensor. The same resonant frequency steps can be seen for the negative and positive orientations at 15 and 16 MHz respectively. Note the expected power out is approximately the same for both sensors. It is suspected that the Helmholtz coil characteristics have
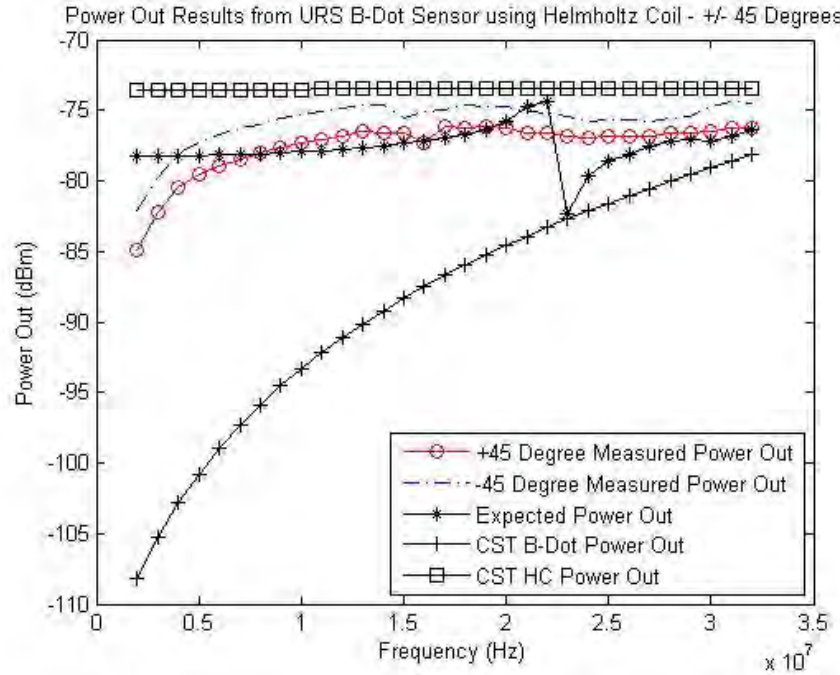
Figure 4.10:   Power Out Results from URS B-Dot Sensor using Helmholtz Coil - +/- 45 Degrees

changed and the resonant frequency is no longer between 20 and 25 MHz, but rather between 15 to 16 MHz.

4.1.3   Prodyn vs.URS B-Dot Sensor - Helmholtz Coil.

Although both the Prodyn and URS sensors are manufactured using the same design, it is important to compare the two in order to verify similarities or possible differences. This section compares the measured results between the Prodyn and URS B-Dot sensors at specified orientations. The results in this section simply compare the results given in Sections 4.1.2 and 4.1.1. The results seen in Figure 4.12 compare the measured values of the Prodyn and URS sensors at the zero degree orientation.

As can be seen, in Figure 4.12, both sensors follow the same pattern with a slightly higher power out for the URS sensor. The average difference between the two sensors is 1.07 dBm. The average difference between the two sensors is deemed to be insignificant since all values are well above the -116.8 dBm noise floor. Further results
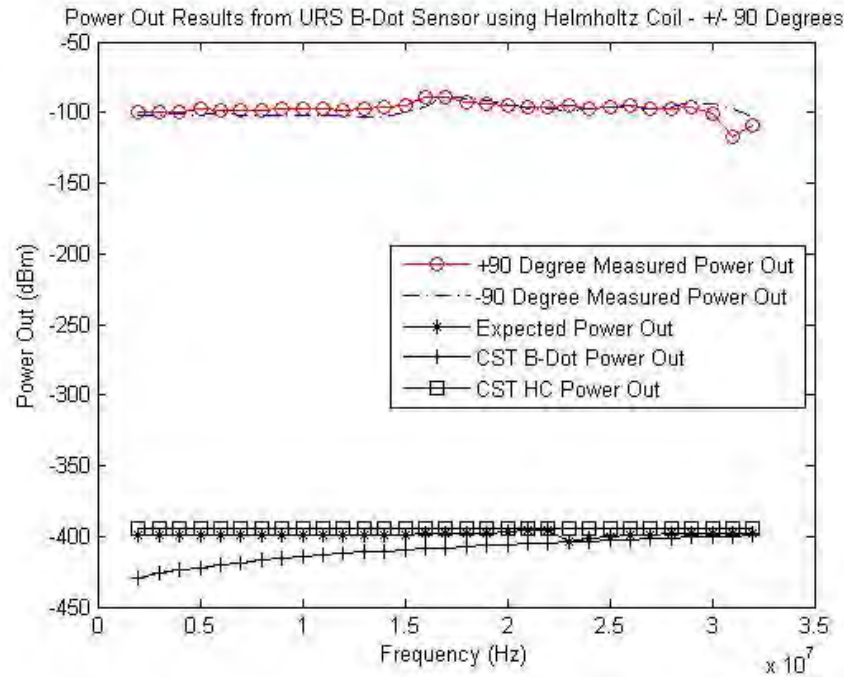
Figure 4.11:   Power Out Results from URS B-Dot Sensor using Helmholtz Coil - +/- 90 Degrees
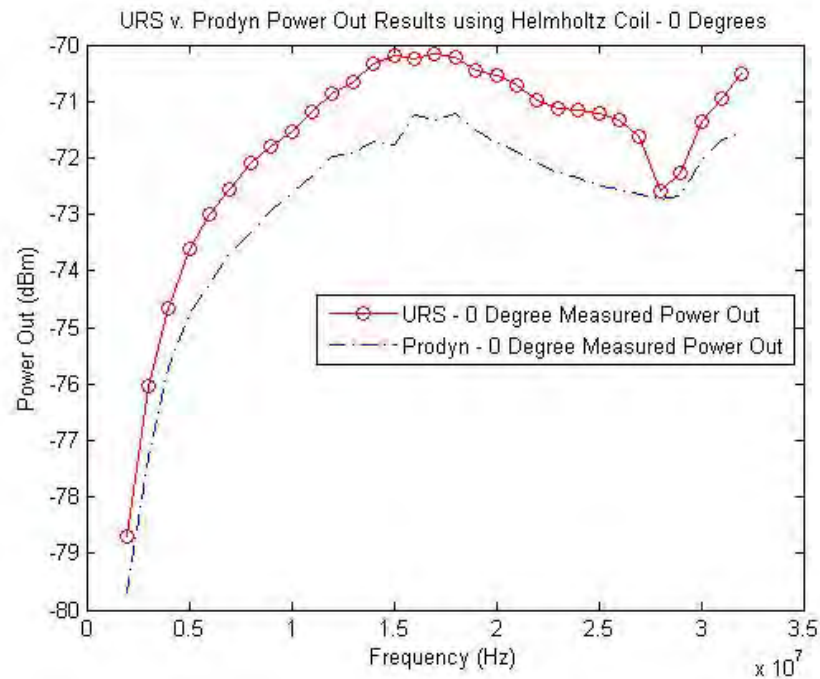
Figure 4.12:   Prodyn v. URS B-Dot Sensor Comparison with Helmholtz Coil - 0 Degrees

shown in Figure 4.13 show the measured values of the Prodyn and URS sensors at 45 degrees.
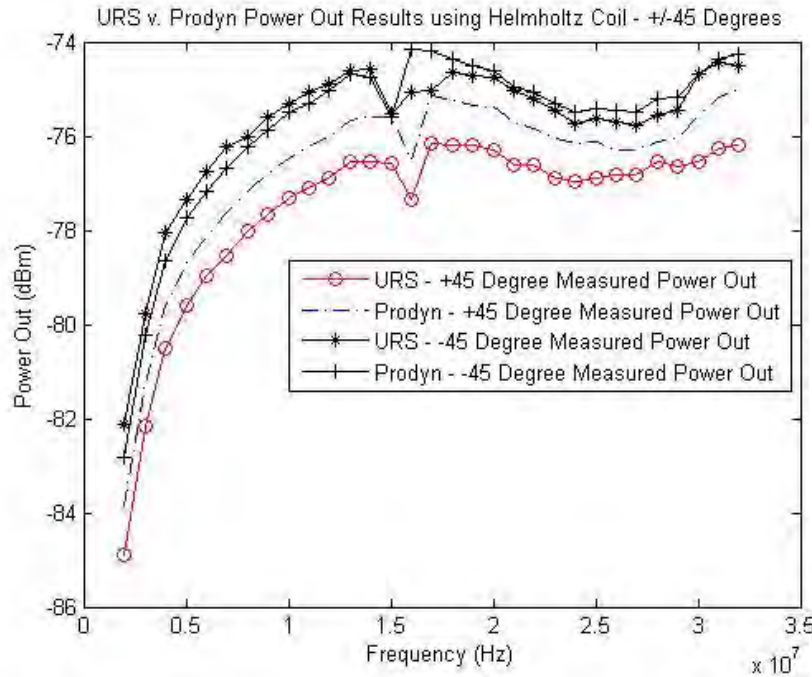
Figure 4.13:   Prodyn v. URS B-Dot Sensor Comparison with Helmholtz Coil - 45 Degrees

The results show that the measurements for both sensors at the -45 degree orientation are nearly identical. The same cannot be said for the measurements taken at the +45 degree orientation. As was seen before in Figure 4.12, the URS sensor was approximately 1 to 2 dBm higher than the Prodyn sensor on average; however, the positive 45 degree measurements shown the Prodyn sensor approximately 1 dBm above the URS sensor. It is not expected that the sensor designs differ significantly in any way, rather, the difference in power measurements at this orientation is likely due to an angular error made when making the measurements. One consistency in regards to the measurements taken is that when oriented in the positive direction, the signal is smaller than when oriented in corresponding opposite direction. Figure 4.14 shows the measured values of the Prodyn and URS sensors at 90 degrees.
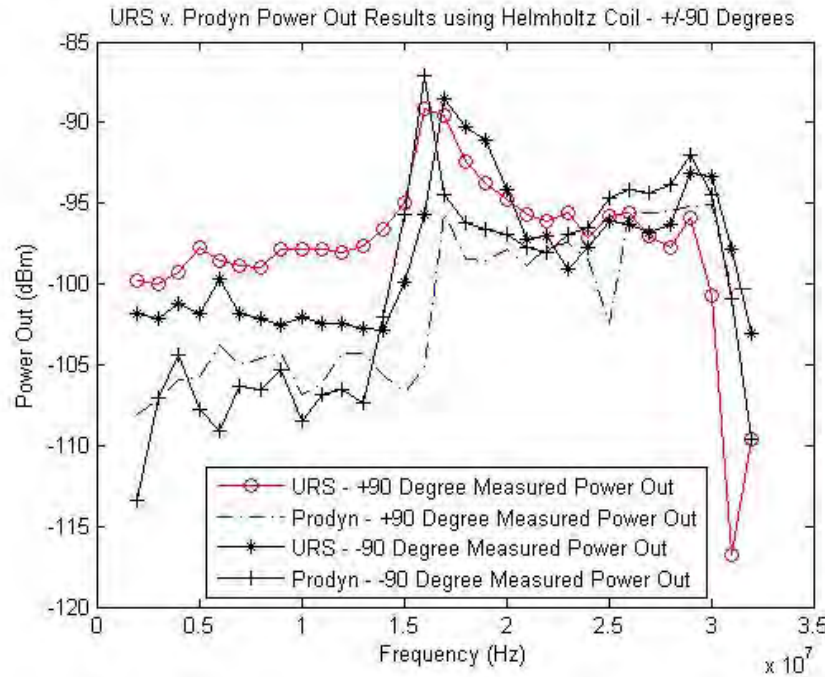
Figure 4.14: Prodyn v. URS B-Dot Sensor Comparison with Helmholtz Coil - 90 Degrees

The values at the 90 degree orientations as mentioned before are too erratic to make accurate predictions. However, despite the randomness of the measured values at this orientation, nearly all the values between maintain a SNR of 6 dB or greater.

4.2 TEM Cell B-Dot Sensor Characterization - Results

The Helmholtz coil was one approach used to generate a magnetic field and characterize the Prodyn and URS B-Dot sensors. Another method used was the TEM cell. The TEM cell is a sound approach to the characterization of the B-Dot sensors and will also serve as an accuracy test for the Helmholtz coil. The TEM cell establishes a uniform electromagnetic fields in a shielded environment. It has a broad operating bandwidth frequency, which is restricted by the waveguide multimode frequency associated with the cell size. The TEM cell is a 50 ohm impedance-matched system and consists of a rectangular coaxial transmission section tapered with coaxial connectors on the both ends, as shown in Figure 2.2.

This section provides measured values taken with the CC-105SEXX TEM Cell. The TEM cell is powered by an Aglient E8257D PSG Analog Signal Generator which supplies a constant 4 dBm input power to the TEM cell from 2-32 MHz. The 4 dBm input power to the TEM cell produces a constant 6.57 nT magnetic field where the two, Prodyn and URS, MGL-S8A B-Dot sensors can be characterized at azimuthal angles of -90, -45, 0, 45, and 90 degrees. The sensors' power out values will be measured on an Aglient E4440A PSA Spectrum Analyzer and will be compared to converted voltage out values calculated in (3.6). Expected values to the TEM cell test, including generated B-field, voltage out, and power out of sensor, can be found in Appendix A.

4.2.1 Prodyn B-Dot Sensor Characterization - TEM Cell.

This section provides results for the TEM cell measured values taken using the Prodyn B-Dot sensor at orientations of -90, -45, 0, 45, and 90 degrees with respect to the generated B-field inside the TEM cell. The noise floor for all TEM cell test measurements was averaged at -114.96 dBm. The spectrum analyzer resolution bandwidth for this test, as with the Helmoltz coil test, was set to 100 Hz. The power out and noise floor level at all orientations for the Prodyn sensor TEM cell test can be found in Appendix G. The first set of results seen in Figure 4.15 show all measured values of the Prodyn sensor at all five orientations.

Notice, unlike the measurements taken with the Helmholtz coil, the TEM cell measurements steadily increase over a span of approximately 22 dBm whereas the Helmholtz coil stayed relatively flat with the exception of the values at the lower frequencies and where the resonance occurs. The steady increase is due to the dependency of the radial frequency, ω. Recall from Section 4.1, the ω value for the Helmholtz coil had canceled out and the only variation to the power out measurement came from the coil measured inductance values. Figure 4.15 shows the measured values at zero degrees at a higher magnitude than all other measurements, as expected. The positive and negative 45 degree orientations, as with the Helmholtz coil, are nearly equal
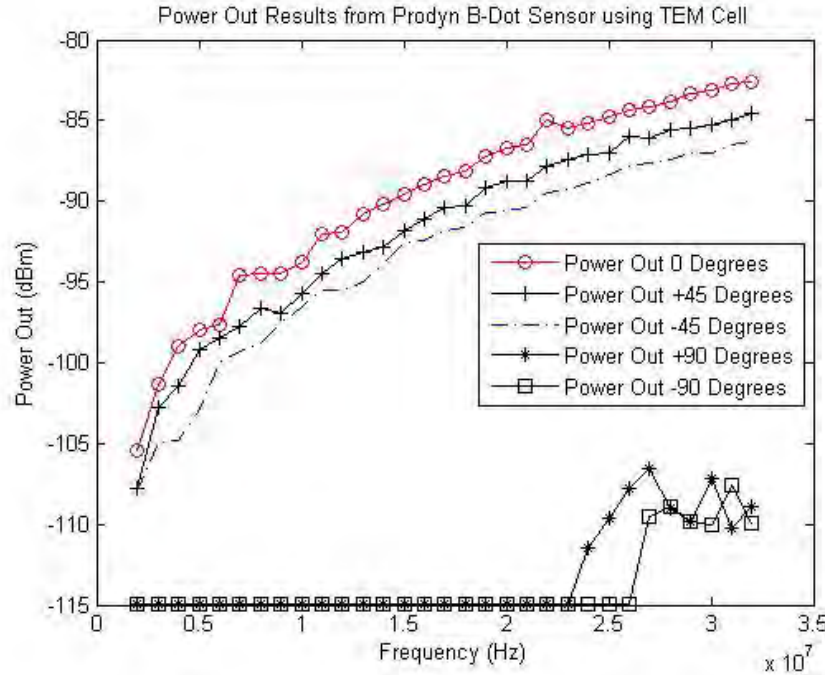
Figure 4.15:   Power Out Results from Prodyn B-Dot Sensor using TEM Cell

and are an average of 2 dBm from the zero degree orientation measurement. The discrepancy in the positive and negative 45 degree measurements where the negative 45 degree values is approximately 1 dBm higher than the positive 45 degree measurement is likely due to exact measurement orientation, or the semi-asymmetrical design of the MGL-S8A sensor. The positive and negative 90 degree measurements can also be seen in Figure 4.15. Due to the overall lower magnetic field generated within the TEM cell, opposed to the Helmholtz coil, the first signals detected at this orientation were not seen until 24 MHz for the negative 90 degree orientation and 27 MHz for the positive 90 degree orientation. Despite the 3 MHz difference between initially detect signals at this orientation, analyzing other local peaks and valleys at 29, 30, and 31 MHz show a 1 MHz frequency shift between the positive and negative 90 orientations. This is the same pattern seen in the Helmholtz coil test where the frequency shifts depending on the positive or negative orientation of the sensor. As with the Helmholtz coil test, the 90 degree measurements are erratic and have broken down from the steady increase when measured at the other orientations. Figure 4.16

59

show the same measured values as compared to the surrounding -114.96 dBm noise floor.
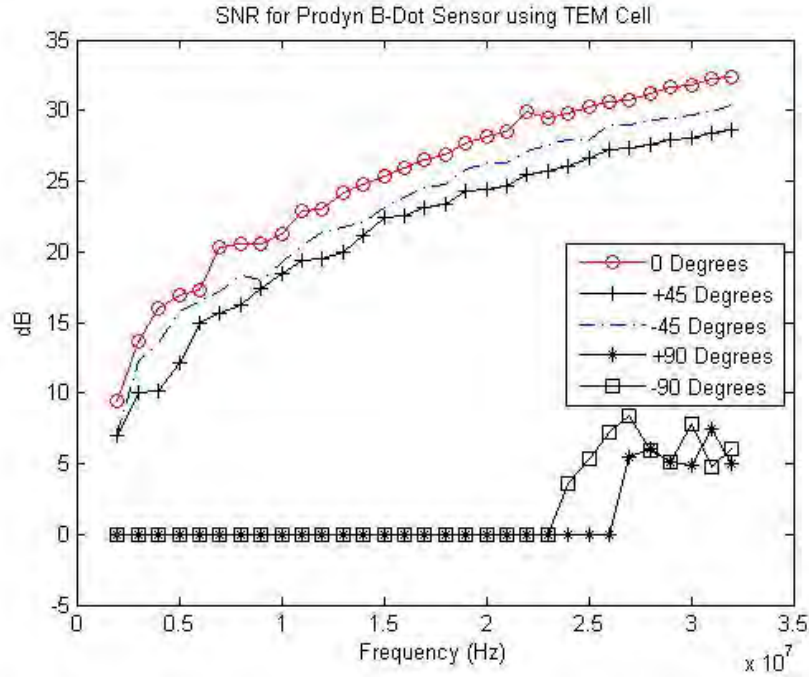
Figure 4.16:   Integrated SNR from Prodyn B-Dot Sensor using TEM Cell

Notice the positive and negative 45 degree values do not surpass the 6 dB detectable signal threshold at 2 MHz, and none of the 90 degree measurements can be considered detectable. These values show the sensor can only detect an input B-field of 6.57 nT at orientations less then 45 degrees in the 2-32 MHz frequency range.

The following results compare the measured values from the Prodyn B-Dot sensor with expected calculated results and CST simulated results. Figures 4.17, 4.18 and 4.19 show the measured results versus the expected and CST results at -90, -45, 0, 45, and 90 degrees. The CST B-Dot power out results are based on the sensor radiation efficiency, total efficiency, and sensor directivity which are derived, as in Section 3.3.3, to express the simulated power out of the B-Dot sensor in dBm. Note, for all measured, expected and CST values, the simulated results become increasingly separated from the measured and analytical results. This is likely due to the ideal

60

environment depicted within the CST simulation; however, discovering an alternate cause for the discrepancy is worth exploring.

The three results of interest in Figure 4.17 are the measured power out, expected power out, and the CST B-Dot power out. As can be seen, the measured and expected values follow the same pattern with an average separation of -2.02 dBm. This difference is acceptable since the -2.02 dBm remains mostly constant from 2-32 MHz. Any discrepancy between the measured and expected values may be due to the V_{RMS} value used (0.354 V) in the expected values calculation opposed to the 0.5 volt peak value. Using 0.5 volts as the input voltage for the theoretical calculation would have put the expected values an average of 1.08 dBm above the measured values for the Prodyn sensor.
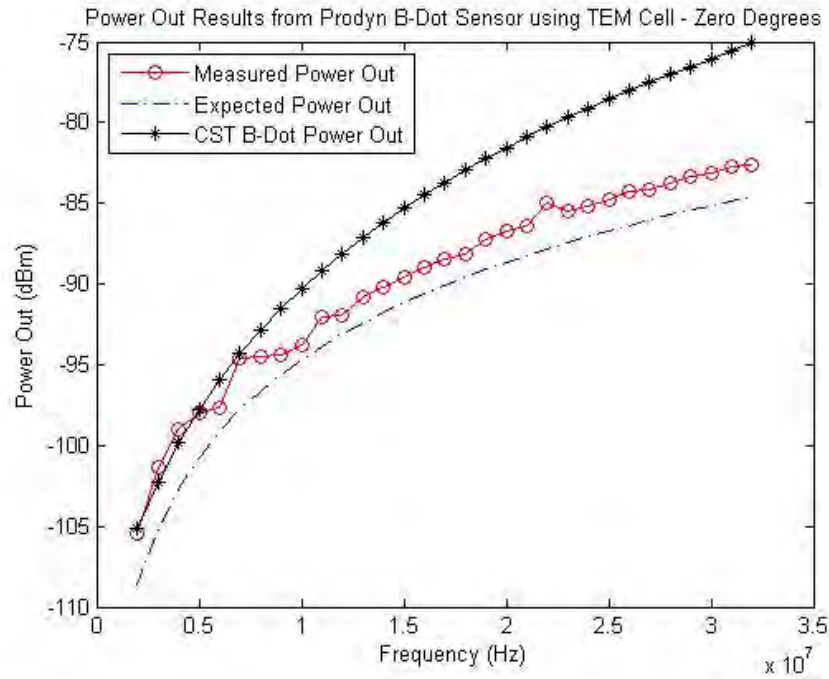
Figure 4.17:   Power Out Results from Prodyn B-Dot Sensor using TEM Cell - Zero Degrees

The next set of results, seen in Figure 4.18, show the measured values at the positive and negative 45 degree orientations compared to the expected values at 45 degrees, and the CST simulation at 45 degrees. It can be seen that the values are

what is expected. One interesting fact to point out is the 1 dBm difference between the positive and negative 45 degree measurements as was seen with the Helmholtz coil.
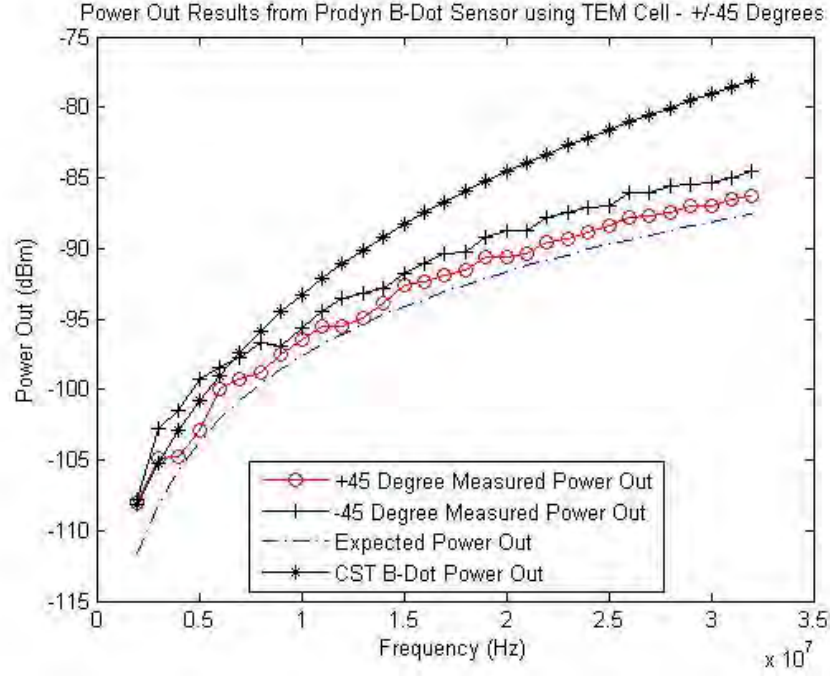
Figure 4.18:   Power Out Results from Prodyn B-Dot Sensor using TEM Cell - +/- 45 Degrees

Also, as can be seen in Figure 4.19 (or more ideally, Figure 4.15), the negative and positive 90 degree orientations values fall mostly into the noise with the exception of measurements taken at 24 and 25 MHz, however, all measurements taken at frequencies above 24 MHz still fall below the 6 dB detection threshold.

4.2.2 URS B-Dot Sensor Characterization - TEM Cell.

This section provides results for measured values taken using the URS B-Dot sensor inside the TEM cell at all orientations of interest. The URS sensor test was done in the same manner as the Prodyn sensor test. The test equipment used remained same and the same average noise floor of -114.96 was used. The URS sensor, as with the Prodyn, was measured with an input power from the signal generator of 4 dBm. The power out and noise floor level at all orientations for the URS sensor TEM cell

62
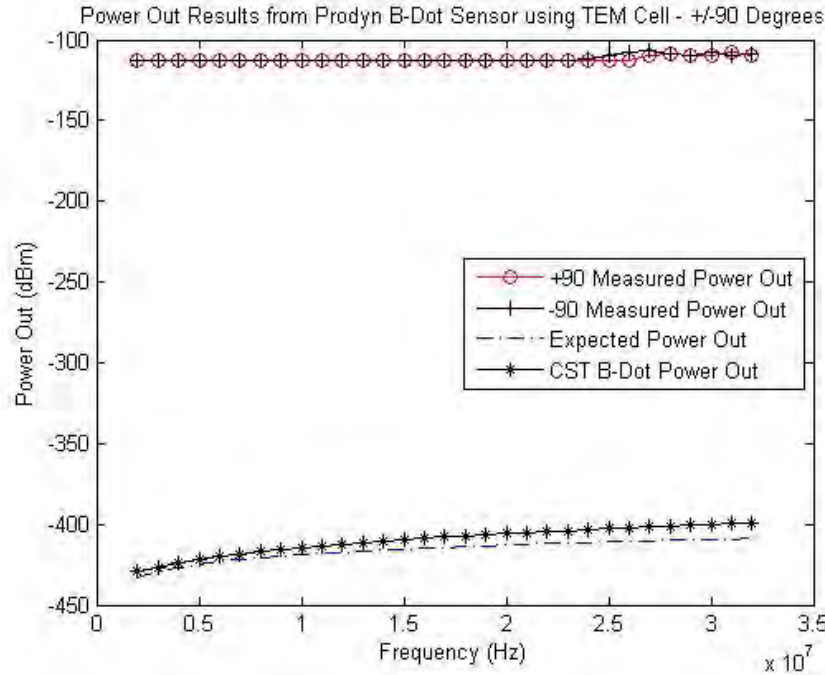
Figure 4.19: Power Out Results from Prodyn B-Dot Sensor using TEM Cell - +/- 90 Degrees

test can be found in Appendix F. The first set of results seen in Figure 4.20 show all measured values of the URS sensor at all five orientations.

It can be seen that the URS sensor follows the same pattern as the Prodyn sensor, comparisons between the two sensors will be made in the next section. Note the close comparison between the positive and negative 45 degree measurements, also, the first measured value at the 90 degree orientations is at 20 MHz and surpasses the 6 dB detectable threshold (7.27 dB). Figure 4.21 shows the same measured values compared to the -14.96 dBm average noise floor.

Figure 4.22 shows the measured results of the URS B-Dot sensor at the zero degree orientation. As with the Prodyn sensor, the measured values follow the same pattern as the expected values and the average difference is also 2 dBm. The discrepancy is likely due to the V_{RMS} values used in the expected values calculation opposed to the 0.5 volt peak value. As with the Prodyn sensor, given an input voltage of 0.5
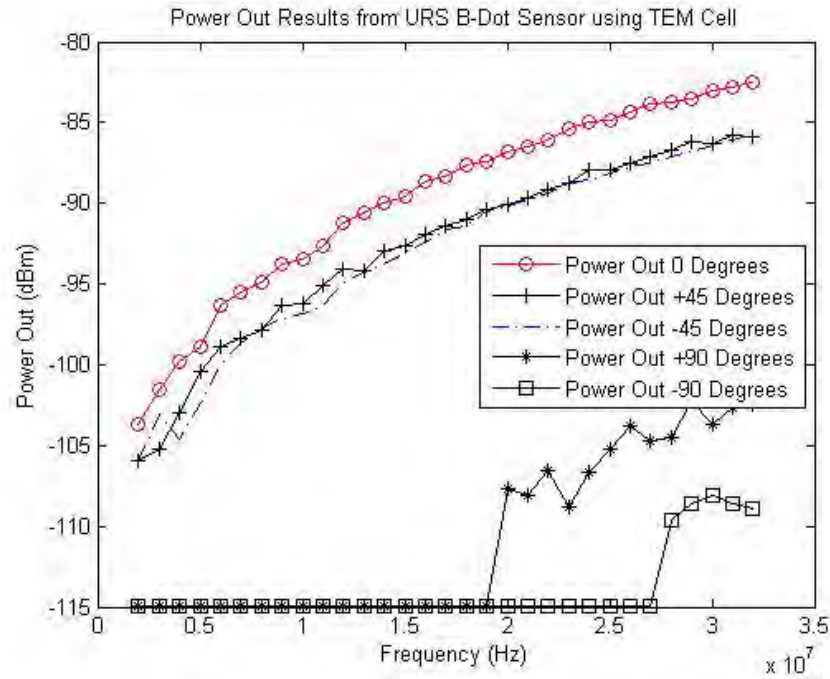
Figure 4.20:   Power Out Results from URS B-Dot Sensor using TEM Cell
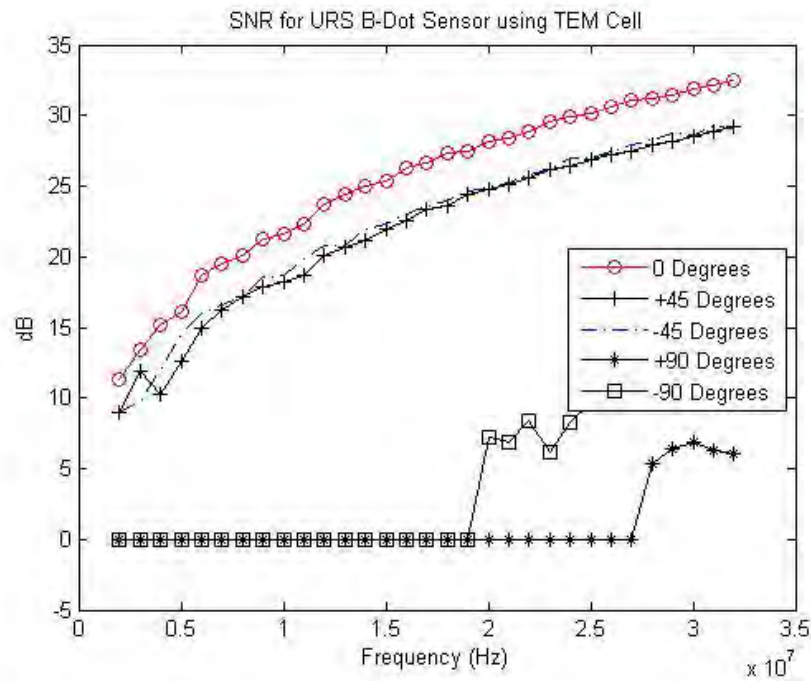
Figure 4.21:   Integrated SNR from URS B-Dot Sensor using TEM Cell

for the theoretical calculations, the expected values are an average of 1.08 dBm above the measured of the URS sensor.
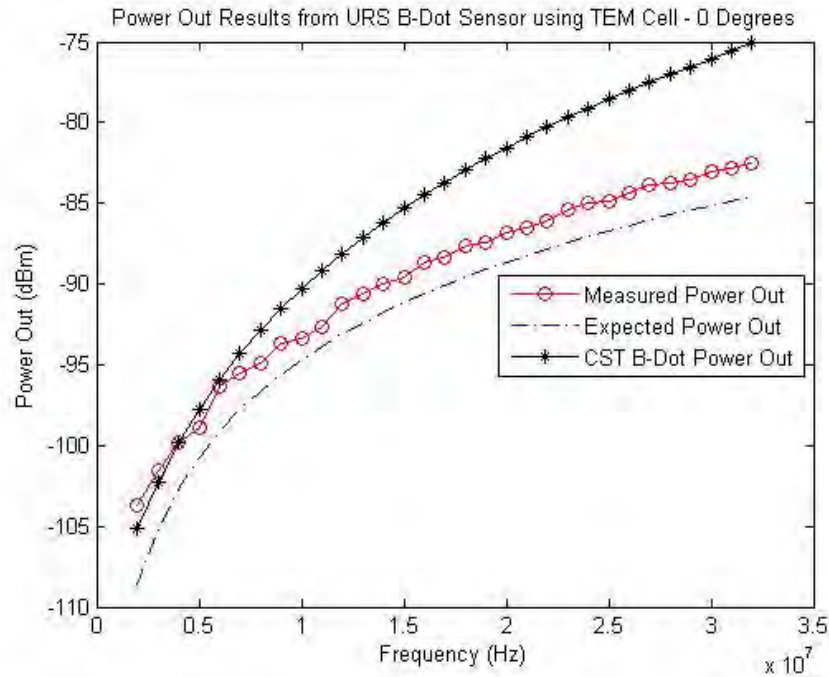
Figure 4.22:   Power Out Results from URS B-Dot Sensor using TEM Cell - Zero Degrees

The following Figures 4.23 and 4.24 show the URS B-Dot sensor measured values at the 45 degree orientations and 90 orientations, respectively. Figure 4.23 shows the values at both 45 degree orientations which, unlike the measurements made with the Prodyn sensor, are nearly all equal. It is likely the 45 degree orientation may have been more exact during this test, if so, the semi-symmetrical design of the sensor can be disregarded as a cause for the different power out values at the positive and negative orientations.

Also, as can be seen in Figure 4.24 (or more ideally, Figure 4.20), the negative and positive 90 degree orientations values fall mostly into the noise with the exception of measurements starting at 20 MHz. Unlike the Prodyn sensor, values at 20 MHz in the negative 90 degree orientation are above the 6 dB detection threshold; however, any consistent pattern breaks down at the 90 degree orientation.

65
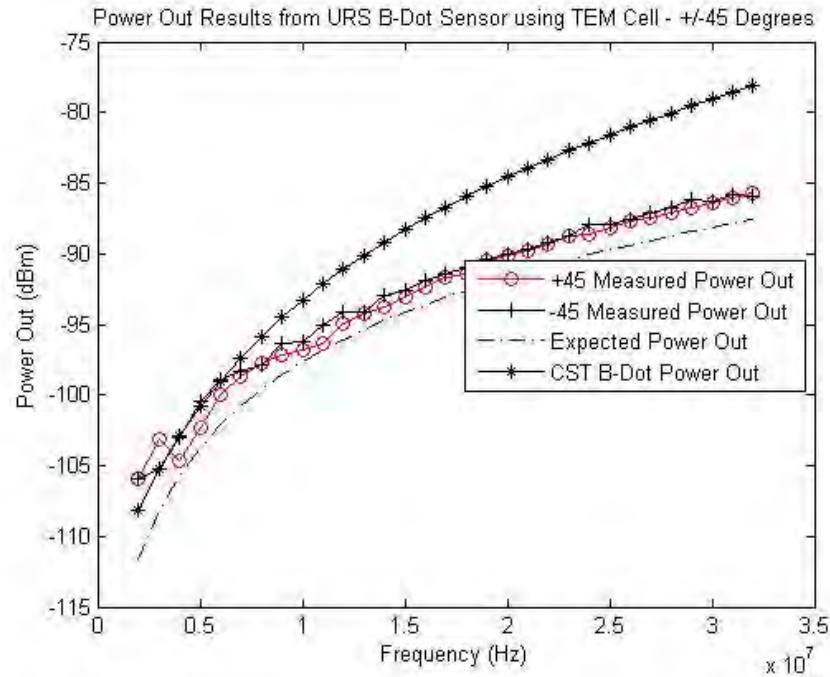
Figure 4.23:   Power Out Results from URS B-Dot Sensor using TEM Cell - +/- 45 Degrees
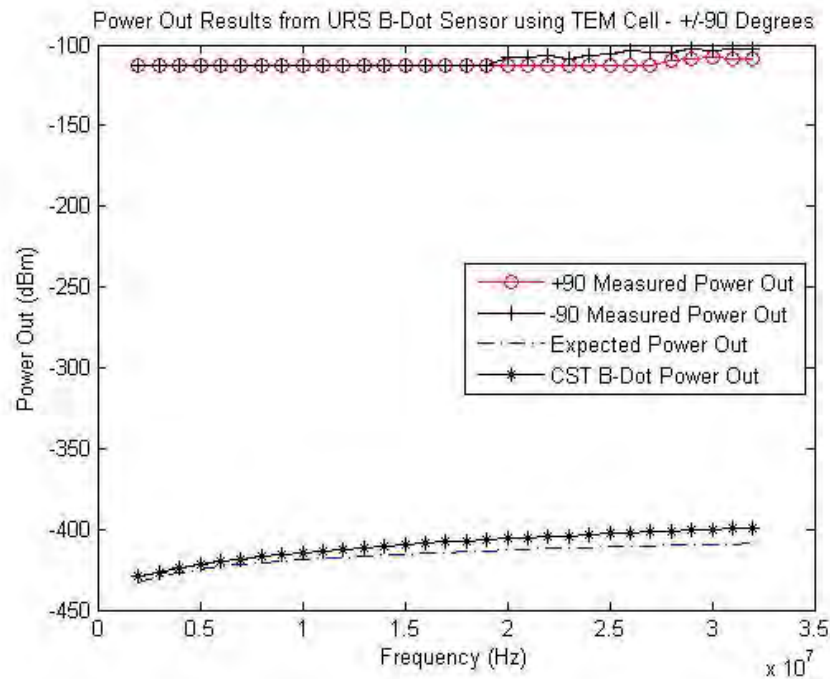
Figure 4.24:   Power Out Results from URS B-Dot Sensor using TEM Cell - +/- 90 Degrees

4.2.3 Prodyn vs.URS B-Dot Sensor - TEM Cell.

The following results show comparisons between the TEM cell measured values for the Prodyn and URS B-Dot sensors at all orientations of interest. The plots given are measured values which were initially presented in Sections 4.2.1 and 4.2.2.The power out and noise floor measurements for the TEM cell test at all orientations for the Prodyn and URS sensors can be found in Appendices G and F. The following results seen in Figure 4.25 show the measured values of the Prodyn and URS sensors at the zero degree orientation.
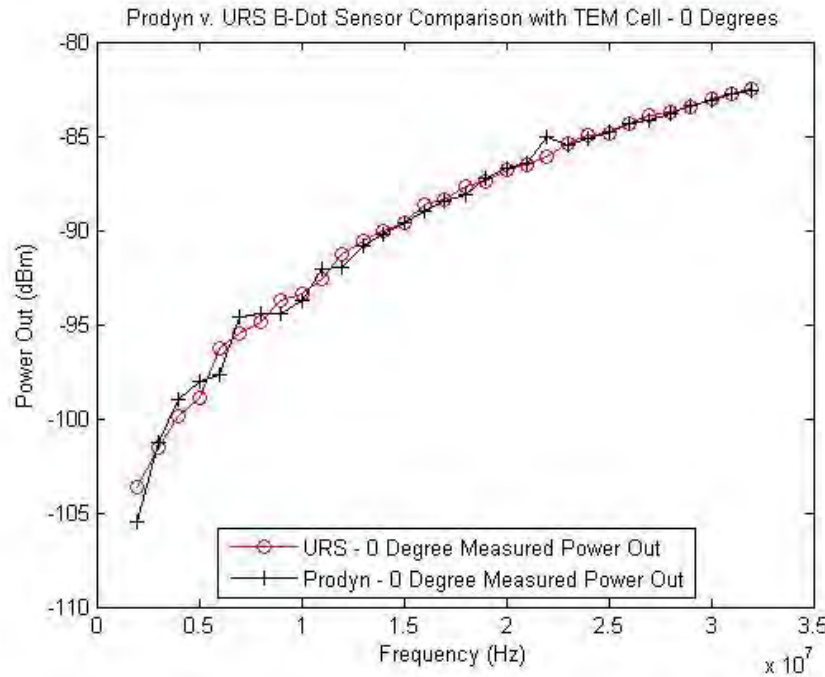
Figure 4.25:   Prodyn v. URS B-Dot Sensor Comparison with TEM Cell - 0 Degrees

Figure 4.25 shows both sensors follow the same pattern with an average difference of only 0.056 dBm. The lowest SNR values (2 MHz) of both the URS and Prodyn sensors at the 0 degree orientation are 11.29 and 9.49 dB respectively, a difference of only 1.8 dB. Because both sensors have a SNR value of greater than 6 dB, both are considered detectable at the all frequencies at this orientation. The highest SNR values for each sensor were recorded at 32 MHz. The SNR value of the URS sensor at this frequency was 32.46 dB whereas the Prodyn sensor was 32.35 dB, a difference

of 0.11 dB. Power measurements for each sensor increases steadily throughout the frequency range, the average step size throughout the range for the URS sensor is 0.705 dB and 0.762 dB for the Prodyn. Further results seen in Figure 4.26 show the measured values of the Prodyn and URS sensors at 45 degrees.
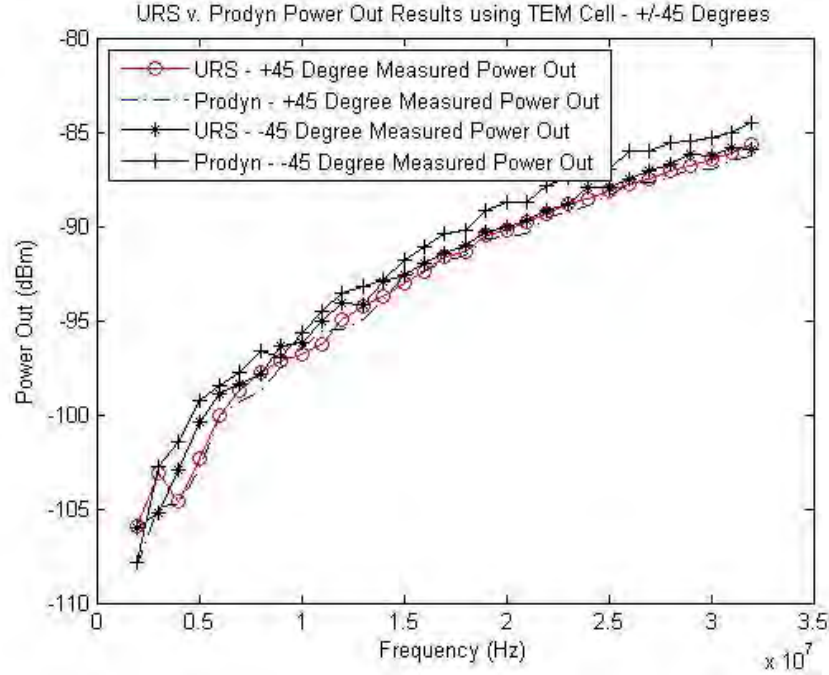
Figure 4.26:   Prodyn v. URS B-Dot Sensor Comparison with TEM Cell - 45 Degrees

Recall, the slight differences in measured values at specified orientations are likely due to orientation approximations made during the test process. The measured values at the positive and negative 45 degree values also follow a consistent pattern. The average step size from 2-32 MHz at the negative 45 degree orientation for the URS sensor is 0.669 dBm and 0.775 dBm for the Prodyn sensor. These values show approximately the same steady increase throughout the frequency range for each sensor. The power out difference at the negative 45 degree orientation between the two sensors is also small at 0.106 dBm.   The measured values for both sensors at the positive 45 degree orientation are also approximately the same with an average difference of 0.048 dBm. The step size for the URS sensor at the positive 45 degree orientation 0.675 dBm and 0.723 dBm for the Prodyn. These values show incredibly

68

accurate consistency between each sensor at the given orientations. The SNR for all measurements at both 45 degree orientations are greater than 6 dB; however, at the 2 MHz measurement, the Prodyn sensor is 1.83 dB smaller at the -45 degree measurement and 2.03 dB smaller at the positive 45 degrees. The next set of results seen in Figure 4.27 show the measured values of the Prodyn and URS sensors at 90 degrees.
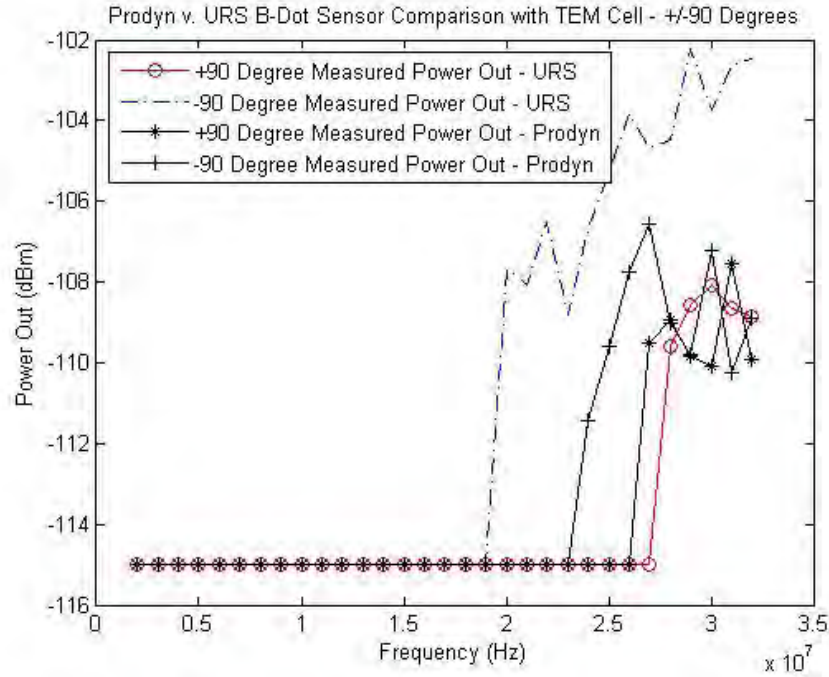
Figure 4.27:   Prodyn v. URS B-Dot Sensor Comparison with TEM Cell - 90 Degrees

As can be seen, most measurements taken at both the positive and negative 90 degree orientations for both sensors fall below the average noise floor. An interesting observation is that the responses from both sensors at the negative 90 degree orientation. It appears the sensors may be more responsive in the negative orientation. The first detectable signals from both sensors occur at 20 and 24 MHz, before any measured signals in the positive orientation. Also, the URS sensor seems more sensitive then the Prodyn. All measured values for the URS sensor above the noise floor are greater than 6 dB, whereas the Prodyn sensor only has a few measurements that exceed the 6 dB threshold. Determining the pattern breakdown as the sensor

orientation goes beyond the positive and negative 45 degree orientations would be ideal to more accurately characterize the angular response of the MGL-S8A sensors.

V. Conclusions and Recommendations

5.1 MGL-S8A B-Dot sensors in HF

The primary goal of this thesis is to determine if a MGL-S8A magnetic field sensor can be properly simulated and characterized in the 2-32 MHz frequency spectrum. The sensor capability is evaluated to determine if it can be used as one of an ensemble of sensors on board a military aircraft as part as a HF magnetic field DF array.

The measurements taken from the Prodyn and URS B-Dot sensors consistently reflect the expected values calculated when using the TEM cell and closely match the values given by the Helmholtz coil method. Also, the sensor response does not degrade significantly from 0 to +/- 45 azimuthal orientations. This is an impressive observation given the sensors are designed to operate at frequencies above 5 GHz. However, because the values do not differ significantly as the orientation changes could make it difficult to use the sensors for direction finding purposes.

5.2 Using the Helmholtz Coil as a Consistent Magnetic Field Generator for HF Characterizations

A secondary goal of this thesis is to simulate and construct a magnetic field generator (Helmholtz coil) to use as an efficient, low-cost alternative test platform to characterize the B-Dot sensors. The Helmholtz coil is a good approach to generating the magnetic field required to characterize the B-Dot sensors in the HF range. At first, due to the large wavelengths from 2-32 MHz (approximately 150 meters at 2 MHz to 9 meters at 32 MHz) it was thought that any proper test would require a substantially large coil. However, after researching what a Helmholtz coil was and understanding the theory behind it helped me realize that this method was not only feasible, but surprisingly practical. Dr. Theodore Anderson's research conducted in the development of AC Helmholtz coils in the HF range was vital in order to build an efficient coil [1].

The Helmholtz coil developed and used for the characterization testing done in this thesis did not have a steady inductance throughout the entire 2-32 MHz. Because of this resonance, the coil was not ideal. An ideal Helmholtz coil would have had a steady inductance, resulting in a constant current, throughout the entire frequency spectrum of interest. A relatively steady inductance can be established as long as there is no resonant frequency. The inductance measurements made on the one-turn Helmholtz coil used in this research stayed fairly steady ($1.6\mu H$ to $1.9\ \mu H$) from 2-20 MHz. The 20 MHz measurement was deemed to be the last steady measurement before the inductance became too high (the resonant frequency spike at 24 MHz can be seen in Figure 3.3). However, the coil becomes steady again at 30 MHz with an inductance of $1.6\mu H$. It is important when developing a Helmholtz coil to have a consistent current throughout, this requires a steady inductance in the frequency range of interest. A Helmholtz coil with a larger radius, 2-times (8 inches) larger than what was used in this research, would lower the resonant frequency below 2 MHz, allowing for a steady field throughout. However, increasing the inductance by creating a larger coil will result in a smaller B-field being generated and, depending on the size and input, could result in drive current fall-off which would move the ideal location of the magnetic field inside the Helmholtz coil to one side. Another approach to get rid of the resonant frequency is to make the coil smaller and pushing the resonant frequency beyond the 32 MHz point. Whichever approach is decided on, it is recommended the 1-turn parameter should be used as a major constraint in the coil. Any coil with multiple turns on each side start to develop a parasitic capacitance which causes the coil to become inaccurate and unpredictable. The test equipment and settings for this test were sufficient; the 12 gauge wire used was also sufficient but a less rigid wire may be ideal. Also, constructing a mu-metal for the Helmholtz coil would help decrease the noise level.

5.3 Recommendations and Future Work

The MGL-S8A B-Dot sensors are an item of interest is because their small size and this research has shown they are capable of detecting magnetic fields in the 2-32 MHz range. The sensors may be able to supplement a DF system that is intended to be used onboard military aircraft. Although the B-Dot sensors presented in this research have potential, much like the simulated structurally integrated BerrieHill antennas studied by Corbin [4], there are some disadvantages. It is worth looking into more sensitive sensors that may be used in lieu of or in conjunction with the MGL-S8A's.

A more accurate and speedy approach needs to be devised in order to properly test the sensors at various angles. The Helmholtz coil and TEM cell methods used in this research were time consuming and angular accuracy was unreliable. An ideal solution to help with the angular accuracy would be to use a solid, sturdy, SMA cable instead of the rigid cable used during these test. The sturdy cable can be place on an angular dial that can be varied in 1-degree increments. This approach will help to increase confidence in the angular performance characterization of the sensors at positive and negative orientations and help to determine at which angle the consistent pattern measured starts to breakdown. Another thought would be to purchase a small rotary joint assembly, as used in a radar system, to accurately measure the angles, see Figure 5.1.

Figure 5.1:   Rotary Joint

Along with accurate azimuthal angles, it is important to also characterize the sensor in elevation as well. I have researched but could not find the type of hinged cable I had in mind. Figure 5.2 shows a hinged antenna.

Figure 5.2:   Hinged Antenna

Something like this would be ideal, maybe a hinged antenna can be purchased and modified with SMA connectors to fit the B-Dot sensors. Along with angular accuracy, it is also important to speed up the test process. During the tests conducted during this research, the average sweep time between measured frequencies was 45 seconds. This made the test process very long. An approach that may help reduce test time would be to use the LabView software. LabView should help speed up the testing process which will allow for further tests to be conducted (i.e. conducting tests in elevation).

Appendix A. Sensor Characterization Theoretical Results - TEM Cell

Table A.1:   MGL-S8A(R) TEM Cell Expected Values - 0 Degrees

	0 degrees @ 4dBm input power		
Freq (MHz)	B-Field (tesla)	Voltage Out (volts)	Power Out (dBm)
2	6.57E-09	8.30E-07	-108.66
3	6.57E-09	1.24E-06	-105.14
4	6.57E-09	1.65E-06	-102.64
5	6.57E-09	2.06E-06	-100.70
6	6.57E-09	2.48E-06	-99.12
7	6.57E-09	2.89E-06	-97.78
8	6.57E-09	3.30E-06	-96.62
9	6.57E-09	3.71E-06	-95.59
10	6.57E-09	4.13E-06	-94.68
11	6.57E-09	4.54E-06	-93.85
12	6.57E-09	4.95E-06	-93.09
13	6.57E-09	5.36E-06	-92.40
14	6.57E-09	5.78E-06	-91.76
15	6.57E-09	6.19E-06	-91.16
16	6.57E-09	6.60E-06	-90.60
17	6.57E-09	7.01E-06	-90.07
18	6.57E-09	7.43E-06	-89.57
19	6.57E-09	7.84E-06	-89.10
20	6.57E-09	8.25E-06	-88.66
21	6.57E-09	8.67E-06	-88.23
22	6.57E-09	9.08E-06	-87.83
23	6.57E-09	9.49E-06	-87.44
24	6.57E-09	9.90E-06	-87.07
25	6.57E-09	1.03E-05	-86.72
26	6.57E-09	1.07E-05	-86.38
27	6.57E-09	1.11E-05	-86.05
28	6.57E-09	1.16E-05	-85.74
29	6.57E-09	1.20E-05	-85.43
30	6.57E-09	1.24E-05	-85.14
31	6.57E-09	1.28E-05	-84.85
32	6.57E-09	1.32E-05	-84.58

Table A.2:   MGL-S8A(R) TEM Cell Expected Values - 45 Degrees

	-/+ 45 degrees @ 4dBm input power		
Freq (MHz)	B-Field (tesla)	Voltage Out (volts)	Power Out (dBm)
2	6.57E-09	5.84E-07	-111.67
3	6.57E-09	8.75E-07	-108.15
4	6.57E-09	1.17E-06	-105.65
5	6.57E-09	1.46E-06	-103.71
6	6.57E-09	1.75E-06	-102.13
7	6.57E-09	2.04E-06	-100.79
8	6.57E-09	2.33E-06	-99.63
9	6.57E-09	2.63E-06	-98.60
10	6.57E-09	2.92E-06	-97.69
11	6.57E-09	3.21E-06	-96.86
12	6.57E-09	3.50E-06	-96.10
13	6.57E-09	3.79E-06	-95.41
14	6.57E-09	4.09E-06	-94.77
15	6.57E-09	4.38E-06	-94.17
16	6.57E-09	4.67E-06	-93.61
17	6.57E-09	4.96E-06	-93.08
18	6.57E-09	5.25E-06	-92.58
19	6.57E-09	5.54E-06	-92.11
20	6.57E-09	5.84E-06	-91.67
21	6.57E-09	6.13E-06	-91.24
22	6.57E-09	6.42E-06	-90.84
23	6.57E-09	6.71E-06	-90.45
24	6.57E-09	7.00E-06	-90.08
25	6.57E-09	7.30E-06	-89.73
26	6.57E-09	7.59E-06	-89.39
27	6.57E-09	7.88E-06	-89.06
28	6.57E-09	8.17E-06	-88.75
29	6.57E-09	8.46E-06	-88.44
30	6.57E-09	8.75E-06	-88.15
31	6.57E-09	9.05E-06	-87.86
32	6.57E-09	9.34E-06	-87.59

Table A.3:   MGL-S8A(R) TEM Cell Expected Values - 90 Degrees

	-/+ 90 degrees @ 4dBm input power		
Freq (MHz)	B-Field (tesla)	Voltage Out (volts)	Power Out (dBm)
2	6.57E-09	5.05E-23	-432.92
3	6.57E-09	7.58E-23	-429.40
4	6.57E-09	1.01E-22	-426.90
5	6.57E-09	1.26E-22	-424.96
6	6.57E-09	1.52E-22	-423.38
7	6.57E-09	1.77E-22	-422.04
8	6.57E-09	2.02E-22	-420.88
9	6.57E-09	2.27E-22	-419.85
10	6.57E-09	2.53E-22	-418.94
11	6.57E-09	2.78E-22	-418.11
12	6.57E-09	3.03E-22	-417.36
13	6.57E-09	3.29E-22	-416.66
14	6.57E-09	3.54E-22	-416.02
15	6.57E-09	3.79E-22	-415.42
16	6.57E-09	4.04E-22	-414.86
17	6.57E-09	4.30E-22	-414.33
18	6.57E-09	4.55E-22	-413.83
19	6.57E-09	4.80E-22	-413.36
20	6.57E-09	5.05E-22	-412.92
21	6.57E-09	5.31E-22	-412.49
22	6.57E-09	5.56E-22	-412.09
23	6.57E-09	5.81E-22	-411.70
24	6.57E-09	6.06E-22	-411.33
25	6.57E-09	6.32E-22	-410.98
26	6.57E-09	6.57E-22	-410.64
27	6.57E-09	6.82E-22	-410.31
28	6.57E-09	7.08E-22	-410.00
29	6.57E-09	7.33E-22	-409.69
30	6.57E-09	7.58E-22	-409.40
31	6.57E-09	7.83E-22	-409.11
32	6.57E-09	8.09E-22	-408.84

Appendix B. Sensor Characterization Theoretical Results - Helmholtz

Coil

Table B.1:   MGL-S8A(R) Helmholtz Coil Expected Values

Freq (MHz)	0 degrees @ 1 Vpp input voltage		
	B-Field (tesla)	Voltage Out (volts)	Power Out (dBm)
2	3.09E-07	3.88E-05	-75.21
3	2.06E-07	3.88E-05	-75.22
4	1.54E-07	3.88E-05	-75.21
5	1.24E-07	3.89E-05	-75.19
6	1.04E-07	3.91E-05	-75.15
7	8.92E-08	3.92E-05	-75.12
8	7.86E-08	3.95E-05	-75.06
9	7.03E-08	3.98E-05	-75.00
10	6.38E-08	4.01E-05	-74.93
11	5.85E-08	4.05E-05	-74.85
12	5.43E-08	4.09E-05	-74.75
13	5.06E-08	4.13E-05	-74.67
14	4.78E-08	4.21E-05	-74.51
15	4.54E-08	4.28E-05	-74.35
16	4.35E-08	4.37E-05	-74.18
17	4.20E-08	4.49E-05	-73.95
18	4.08E-08	4.62E-05	-73.70
19	4.01E-08	4.79E-05	-73.38
20	4.09E-08	5.14E-05	-72.76
21	4.41E-08	5.82E-05	-71.70
22	4.36E-08	6.02E-05	-71.39
23	1.67E-08	2.42E-05	-79.33
24	2.19E-08	3.30E-05	-76.62
25	2.36E-08	3.70E-05	-75.62
26	2.39E-08	3.90E-05	-75.16
27	2.47E-08	4.18E-05	-74.56
28	2.48E-08	4.36E-05	-74.20
29	2.44E-08	4.44E-05	-74.05
30	2.33E-08	4.40E-05	-74.13
31	2.34E-08	4.56E-05	-73.80
32	2.37E-08	4.77E-05	-73.42

Table B.2:   MGL-S8A(R) Helmholtz Coil Expected Values

| Freq (MHz) | -/+ 45 degrees @ 1 Vpp input voltage | | |
	B-Field (tesla)	Voltage Out (volts)	Power Out (dBm)
2	3.09E-07	2.75E-05	-78.22
3	2.06E-07	2.74E-05	-78.23
4	1.54E-07	2.75E-05	-78.22
5	1.24E-07	2.75E-05	-78.20
6	1.04E-07	2.76E-05	-78.16
7	8.92E-08	2.77E-05	-78.13
8	7.86E-08	2.79E-05	-78.07
9	7.03E-08	2.81E-05	-78.01
10	6.38E-08	2.84E-05	-77.94
11	5.85E-08	2.86E-05	-77.86
12	5.43E-08	2.89E-05	-77.76
13	5.06E-08	2.92E-05	-77.68
14	4.78E-08	2.98E-05	-77.52
15	4.54E-08	3.03E-05	-77.37
16	4.35E-08	3.09E-05	-77.19
17	4.20E-08	3.17E-05	-76.96
18	4.08E-08	3.27E-05	-76.71
19	4.01E-08	3.39E-05	-76.39
20	4.09E-08	3.64E-05	-75.77
21	4.41E-08	4.11E-05	-74.71
22	4.36E-08	4.26E-05	-74.40
23	1.67E-08	1.71E-05	-82.34
24	2.19E-08	2.33E-05	-79.63
25	2.36E-08	2.62E-05	-78.63
26	2.39E-08	2.76E-05	-78.17
27	2.47E-08	2.96E-05	-77.57
28	2.48E-08	3.08E-05	-77.21
29	2.44E-08	3.14E-05	-77.06
30	2.33E-08	3.11E-05	-77.14
31	2.34E-08	3.23E-05	-76.81
32	2.37E-08	3.37E-05	-76.43

Table B.3:   MGL-S8A(R) Helmholtz Coil Expected Values

Freq (MHz)	-/+ 90 degrees @ 1 Vpp input voltage		
	B-Field (tesla)	Voltage Out (volts)	Power Out (dBm)
2	3.09E-07	2.38E-21	-399.47
3	2.06E-07	2.37E-21	-399.48
4	1.54E-07	2.38E-21	-399.47
5	1.24E-07	2.38E-21	-399.45
6	1.04E-07	2.39E-21	-399.41
7	8.92E-08	2.40E-21	-399.38
8	7.86E-08	2.42E-21	-399.32
9	7.03E-08	2.44E-21	-399.26
10	6.38E-08	2.46E-21	-399.19
11	5.85E-08	2.48E-21	-399.11
12	5.43E-08	2.51E-21	-399.01
13	5.06E-08	2.53E-21	-398.93
14	4.78E-08	2.58E-21	-398.77
15	4.54E-08	2.62E-21	-398.62
16	4.35E-08	2.68E-21	-398.44
17	4.20E-08	2.75E-21	-398.21
18	4.08E-08	2.83E-21	-397.96
19	4.01E-08	2.94E-21	-397.64
20	4.09E-08	3.15E-21	-397.02
21	4.41E-08	3.56E-21	-395.96
22	4.36E-08	3.69E-21	-395.65
23	1.67E-08	1.48E-21	-403.59
24	2.19E-08	2.02E-21	-400.88
25	2.36E-08	2.27E-21	-399.88
26	2.39E-08	2.39E-21	-399.42
27	2.47E-08	2.56E-21	-398.82
28	2.48E-08	2.67E-21	-398.46
29	2.44E-08	2.72E-21	-398.31
30	2.33E-08	2.69E-21	-398.39
31	2.34E-08	2.80E-21	-398.06
32	2.37E-08	2.92E-21	-397.68

Appendix C. B-dot Sensor CST Results

Table C.1:   MGL-S8A(R) CST Measurements (Prodyn)

Freq (MHz)	Radiation Eff (dB)	Total Eff (dB)	Directivity (dBi)	Power Out (dBm)
5	-22.32	-57.45	-82.86	-105.18
6	-22.23	-56.93	-80.02	-102.25
7	-21.54	-55.86	-78.31	-99.85
8	-20.27	-54.27	-77.51	-97.78
9	-19.31	-53.02	-76.66	-95.97
10	-18.64	-52.1	-75.69	-94.33
11	-18.16	-51.39	-74.7	-92.86
12	-17.68	-50.7	-73.84	-91.52
13	-17.19	-50	-73.11	-90.3
14	-16.75	-49.38	-72.41	-89.16
15	-16.35	-48.81	-71.75	-88.1
16	-15.99	-48.28	-71.12	-87.11
17	-15.68	-47.82	-70.5	-86.18
18	-15.36	-47.36	-69.95	-85.31
19	-15.06	-46.92	-69.42	-84.48
20	-14.81	-46.54	-68.89	-83.7
21	-14.56	-46.17	-68.39	-82.95
22	-14.34	-45.82	-67.91	-82.25
23	-14.12	-45.49	-67.45	-81.57
24	-13.93	-45.19	-67	-80.93
25	-13.75	-44.91	-66.55	-80.3
26	-13.58	-44.63	-66.12	-79.7
27	-13.43	-44.39	-65.7	-79.13
28	-13.29	-44.15	-65.29	-78.58
29	-13.15	-43.92	-64.89	-78.04
30	-13.04	-43.72	-64.5	-77.54
31	-12.94	-43.53	-64.1	-77.04
32	-12.83	-43.34	-63.72	-76.55
33	-12.73	-43.16	-63.36	-
34	-12.64	-43	-62.99	-
35	-12.55	-42.83	-62.64	-

Appendix D.   URS Sensor Characterization Results - Helmholtz Coil

Table D.1:   MGL-S8A(R) B-Dot Sensor Measured Values - Helmholtz Coil

URS (SN 61) - 0 degrees @ 1 Vpp input voltage			
Frequency (MHz)	Power Out (dBm)	Noise Floor (dBm)	Above Noise Floor
2	-78.69	-116.8	38.11
3	-76.04	-116.8	40.76
4	-74.65	-116.8	42.15
5	-73.61	-116.8	43.19
6	-73	-116.8	43.8
7	-72.56	-116.8	44.24
8	-72.1	-116.8	44.7
9	-71.81	-116.8	44.99
10	-71.53	-116.8	45.27
11	-71.17	-116.8	45.63
12	-70.85	-116.8	45.95
13	-70.67	-116.8	46.13
14	-70.35	-116.8	46.45
15	-70.18	-116.8	46.62
16	-70.25	-116.8	46.55
17	-70.17	-116.8	46.63
18	-70.21	-116.8	46.59
19	-70.46	-116.8	46.34
20	-70.55	-116.8	46.25
21	-70.73	-116.8	46.07
22	-70.99	-116.8	45.81
23	-71.12	-116.8	45.68
24	-71.15	-116.8	45.65
25	-71.22	-116.8	45.58
26	-71.32	-116.8	45.48
27	-71.63	-116.8	45.17
28	-72.59	-116.8	44.21
29	-72.27	-116.8	44.53
30	-71.35	-116.8	45.45
31	-70.94	-116.8	45.86
32	-70.52	-116.8	46.28

Table D.2:   MGL-S8A(R) B-Dot Sensor Measured Values - Helmholtz Coil

URS (SN 61) - -45 degrees @ 1 Vpp input voltage			
Frequency (MHz)	Power Out (dBm)	Noise Floor (dBm)	Above Noise Floor
2	-82.14	-116.8	34.66
3	-79.76	-116.8	37.04
4	-78.06	-116.8	38.74
5	-77.34	-116.8	39.46
6	-76.77	-116.8	40.03
7	-76.24	-116.8	40.56
8	-76.03	-116.8	40.77
9	-75.58	-116.8	41.22
10	-75.3	-116.8	41.5
11	-75.08	-116.8	41.72
12	-74.89	-116.8	41.91
13	-74.62	-116.8	42.18
14	-74.57	-116.8	42.23
15	-75.54	-116.8	41.26
16	-75.07	-116.8	41.73
17	-75.02	-116.8	41.78
18	-74.64	-116.8	42.16
19	-74.71	-116.8	42.09
20	-74.74	-116.8	42.06
21	-75.03	-116.8	41.77
22	-75.22	-116.8	41.58
23	-75.46	-116.8	41.34
24	-75.74	-116.8	41.06
25	-75.64	-116.8	41.16
26	-75.7	-116.8	41.1
27	-75.77	-116.8	41.03
28	-75.56	-116.8	41.24
29	-75.47	-116.8	41.33
30	-74.68	-116.8	42.12
31	-74.44	-116.8	42.36
32	-74.51	-116.8	42.29

Table D.3:   MGL-S8A(R) B-Dot Sensor Measured Values - Helmholtz Coil

URS (SN 61) - -90 degrees @ 1 Vpp input voltage			
Frequency (MHz)	Power Out (dBm)	Noise Floor (dBm)	Above Noise Floor
2	-101.8	-116.8	15
3	-102.1	-116.8	14.7
4	-101.2	-116.8	15.6
5	-101.8	-116.8	15
6	-99.71	-116.8	17.09
7	-101.8	-116.8	15
8	-102.1	-116.8	14.7
9	-102.6	-116.8	14.2
10	-102	-116.8	14.8
11	-102.4	-116.8	14.4
12	-102.4	-116.8	14.4
13	-102.8	-116.8	14
14	-102.9	-116.8	13.9
15	-99.93	-116.8	16.87
16	-95.7	-116.8	21.1
17	-88.48	-116.8	28.32
18	-90.29	-116.8	26.51
19	-91.08	-116.8	25.72
20	-94.14	-116.8	22.66
21	-97.19	-116.8	19.61
22	-97.01	-116.8	19.79
23	-99.12	-116.8	17.68
24	-97.74	-116.8	19.06
25	-96.15	-116.8	20.65
26	-96.29	-116.8	20.51
27	-96.79	-116.8	20.01
28	-96.31	-116.8	20.49
29	-93.14	-116.8	23.66
30	-93.31	-116.8	23.49
31	-97.89	-116.8	18.91
32	-103.1	-116.8	13.7

Table D.4:   MGL-S8A(R) B-Dot Sensor Measured Values - Helmholtz Coil

URS (SN 61) - +45 degrees @ 1 Vpp input voltage			
Frequency (MHz)	Power Out (dBm)	Noise Floor (dBm)	Above Noise Floor
2	-84.91	-116.8	31.89
3	-82.17	-116.8	34.63
4	-80.51	-116.8	36.29
5	-79.58	-116.8	37.22
6	-78.97	-116.8	37.83
7	-78.53	-116.8	38.27
8	-78.01	-116.8	38.79
9	-77.68	-116.8	39.12
10	-77.32	-116.8	39.48
11	-77.12	-116.8	39.68
12	-76.9	-116.8	39.9
13	-76.54	-116.8	40.26
14	-76.56	-116.8	40.24
15	-76.57	-116.8	40.23
16	-77.36	-116.8	39.44
17	-76.15	-116.8	40.65
18	-76.21	-116.8	40.59
19	-76.18	-116.8	40.62
20	-76.3	-116.8	40.5
21	-76.61	-116.8	40.19
22	-76.63	-116.8	40.17
23	-76.88	-116.8	39.92
24	-76.98	-116.8	39.82
25	-76.88	-116.8	39.92
26	-76.84	-116.8	39.96
27	-76.83	-116.8	39.97
28	-76.56	-116.8	40.24
29	-76.64	-116.8	40.16
30	-76.54	-116.8	40.26
31	-76.28	-116.8	40.52
32	-76.21	-116.8	40.59

Table D.5:   MGL-S8A(R) B-Dot Sensor Measured Values - Helmholtz Coil

URS (SN 61) - +90 degrees @ 1 Vpp input voltage			
Frequency (MHz)	Power Out (dBm)	Noise Floor (dBm)	Above Noise Floor
2	-99.83	-116.8	16.97
3	-100	-116.8	16.8
4	-99.31	-116.8	17.49
5	-97.78	-116.8	19.02
6	-98.56	-116.8	18.24
7	-98.86	-116.8	17.94
8	-98.98	-116.8	17.82
9	-97.89	-116.8	18.91
10	-97.89	-116.8	18.91
11	-97.89	-116.8	18.91
12	-98.07	-116.8	18.73
13	-97.61	-116.8	19.19
14	-96.63	-116.8	20.17
15	-95.01	-116.8	21.79
16	-89.1	-116.8	27.7
17	-89.57	-116.8	27.23
18	-92.39	-116.8	24.41
19	-93.72	-116.8	23.08
20	-94.78	-116.8	22.02
21	-95.66	-116.8	21.14
22	-96.07	-116.8	20.73
23	-95.59	-116.8	21.21
24	-97.11	-116.8	19.69
25	-95.81	-116.8	20.99
26	-95.59	-116.8	21.21
27	-96.99	-116.8	19.81
28	-97.79	-116.8	19.01
29	-95.9	-116.8	20.9
30	-100.7	-116.8	16.1
31	-116.8	-116.8	0
32	-109.6	-116.8	7.2

Appendix E. Prodyn Sensor Characterization Results - Helmholtz Coil

Table E.1: MGL-S8A(R) B-Dot Sensor Measured Values - Helmholtz Coil

Prodyn (SN 61) - 0 degrees @ 1 Vpp input voltage			
Frequency (MHz)	Power Out (dBm)	Noise Floor (dBm)	Above Noise Floor
2	-79.69	-116.8	37.11
3	-77.29	-116.8	39.51
4	-75.72	-116.8	41.08
5	-74.74	-116.8	42.06
6	-74.23	-116.8	42.57
7	-73.71	-116.8	43.09
8	-73.31	-116.8	43.49
9	-72.94	-116.8	43.86
10	-72.62	-116.8	44.18
11	-72.33	-116.8	44.47
12	-71.96	-116.8	44.84
13	-71.91	-116.8	44.89
14	-71.71	-116.8	45.09
15	-71.78	-116.8	45.02
16	-71.23	-116.8	45.57
17	-71.33	-116.8	45.47
18	-71.22	-116.8	45.58
19	-71.51	-116.8	45.29
20	-71.75	-116.8	45.05
21	-71.89	-116.8	44.91
22	-72.08	-116.8	44.72
23	-72.27	-116.8	44.53
24	-72.36	-116.8	44.44
25	-72.49	-116.8	44.31
26	-72.57	-116.8	44.23
27	-72.64	-116.8	44.16
28	-72.74	-116.8	44.06
29	-72.69	-116.8	44.11
30	-72.04	-116.8	44.76
31	-71.68	-116.8	45.12
32	-71.56	-116.8	45.24

Table E.2:   MGL-S8A(R) B-Dot Sensor Measured Values - Helmholtz Coil

Prodyn (SN 61) - -45 degrees @ 1 Vpp input voltage			
Frequency (MHz)	Power Out (dBm)	Noise Floor (dBm)	Above Noise Floor
2	-82.83	-116.8	33.97
3	-80.24	-116.8	36.56
4	-78.66	-116.8	38.14
5	-77.75	-116.8	39.05
6	-77.17	-116.8	39.63
7	-76.68	-116.8	40.12
8	-76.22	-116.8	40.58
9	-75.86	-116.8	40.94
10	-75.48	-116.8	41.32
11	-75.32	-116.8	41.48
12	-75.05	-116.8	41.75
13	-74.68	-116.8	42.12
14	-74.76	-116.8	42.04
15	-75.59	-116.8	41.21
16	-74.17	-116.8	42.63
17	-74.21	-116.8	42.59
18	-74.36	-116.8	42.44
19	-74.52	-116.8	42.28
20	-74.62	-116.8	42.18
21	-74.98	-116.8	41.82
22	-75.06	-116.8	41.74
23	-75.33	-116.8	41.47
24	-75.48	-116.8	41.32
25	-75.42	-116.8	41.38
26	-75.45	-116.8	41.35
27	-75.48	-116.8	41.32
28	-75.22	-116.8	41.58
29	-75.17	-116.8	41.63
30	-74.68	-116.8	42.12
31	-74.36	-116.8	42.44
32	-74.25	-116.8	42.55

Table E.3:   MGL-S8A(R) B-Dot Sensor Measured Values - Helmholtz Coil

Frequency (MHz)	Power Out (dBm)	Noise Floor (dBm)	Above Noise Floor
Prodyn (SN 61) - -90 degrees @ 1 Vpp input voltage			
2	-113.4	-116.8	3.4
3	-107.1	-116.8	9.7
4	-104.4	-116.8	12.4
5	-107.8	-116.8	9
6	-109.1	-116.8	7.7
7	-106.3	-116.8	10.5
8	-106.5	-116.8	10.3
9	-105.3	-116.8	11.5
10	-108.5	-116.8	8.3
11	-106.9	-116.8	9.9
12	-106.5	-116.8	10.3
13	-107.4	-116.8	9.4
14	-102	-116.8	14.8
15	-95.66	-116.8	21.14
16	-87.13	-116.8	29.67
17	-94.49	-116.8	22.31
18	-96.18	-116.8	20.62
19	-96.63	-116.8	20.17
20	-96.94	-116.8	19.86
21	-97.73	-116.8	19.07
22	-98.03	-116.8	18.77
23	-96.95	-116.8	19.85
24	-96.48	-116.8	20.32
25	-94.69	-116.8	22.11
26	-94.16	-116.8	22.64
27	-94.33	-116.8	22.47
28	-93.86	-116.8	22.94
29	-91.96	-116.8	24.84
30	-94.45	-116.8	22.35
31	-100.9	-116.8	15.9
32	-109.6	-116.8	7.2

Table E.4:   MGL-S8A(R) B-Dot Sensor Measured Values - Helmholtz Coil

| Prodyn (SN 61) - +45 degrees @ 1 Vpp input voltage |
Frequency (MHz)	Power Out (dBm)	Noise Floor (dBm)	Above Noise Floor
2	-83.83	-116.8	32.97
3	-81.25	-116.8	35.55
4	-79.6	-116.8	37.2
5	-78.7	-116.8	38.1
6	-78.11	-116.8	38.69
7	-77.62	-116.8	39.18
8	-77.19	-116.8	39.61
9	-76.78	-116.8	40.02
10	-76.46	-116.8	40.34
11	-76.24	-116.8	40.56
12	-76	-116.8	40.8
13	-75.65	-116.8	41.15
14	-75.61	-116.8	41.19
15	-75.59	-116.8	41.21
16	-76.51	-116.8	40.29
17	-75.13	-116.8	41.67
18	-75.25	-116.8	41.55
19	-75.36	-116.8	41.44
20	-75.39	-116.8	41.41
21	-75.71	-116.8	41.09
22	-75.84	-116.8	40.96
23	-76.06	-116.8	40.74
24	-76.17	-116.8	40.63
25	-76.14	-116.8	40.66
26	-76.31	-116.8	40.49
27	-76.31	-116.8	40.49
28	-76.13	-116.8	40.67
29	-76.06	-116.8	40.74
30	-75.55	-116.8	41.25
31	-75.18	-116.8	41.62
32	-74.99	-116.8	41.81

Table E.5:   MGL-S8A(R) B-Dot Sensor Measured Values - Helmholtz Coil

Prodyn (SN 61) - +90 degrees @ 1 Vpp input voltage			
Frequency (MHz)	Power Out (dBm)	Noise Floor (dBm)	Above Noise Floor
2	-108.1	-116.8	8.7
3	-107.2	-116.8	9.6
4	-105.9	-116.8	10.9
5	-105.7	-116.8	11.1
6	-103.8	-116.8	13
7	-105	-116.8	11.8
8	-104.6	-116.8	12.2
9	-104.3	-116.8	12.5
10	-106.8	-116.8	10
11	-106.1	-116.8	10.7
12	-104.3	-116.8	12.5
13	-104.3	-116.8	12.5
14	-105.6	-116.8	11.2
15	-106.7	-116.8	10.1
16	-105.1	-116.8	11.7
17	-95.62	-116.8	21.18
18	-98.46	-116.8	18.34
19	-98.58	-116.8	18.22
20	-97.89	-116.8	18.91
21	-98.91	-116.8	17.89
22	-97.73	-116.8	19.07
23	-97.42	-116.8	19.38
24	-98.42	-116.8	18.38
25	-102.4	-116.8	14.4
26	-95.63	-116.8	21.17
27	-95.58	-116.8	21.22
28	-95.46	-116.8	21.34
29	-95.15	-116.8	21.65
30	-95.08	-116.8	21.72
31	-100.3	-116.8	16.5
32	-100.3	-116.8	16.5

Appendix F. URS Sensor Characterization Results - TEM Cell

Table F.1:   MGL-S8A(R) B-Dot Sensor Measured Values - TEM Cell

URS (SN 61) - 0 degrees @ 4 dBm input power			
Frequency (MHz)	Power Out (dBm)	Noise Floor (dBm)	Above Noise Floor
2	-103.67	-114.96	11.29
3	-101.53	-114.96	13.43
4	-99.84	-114.96	15.12
5	-98.9	-114.96	16.06
6	-96.3	-114.96	18.66
7	-95.48	-114.96	19.48
8	-94.86	-114.96	20.1
9	-93.72	-114.96	21.24
10	-93.41	-114.96	21.55
11	-92.62	-114.96	22.34
12	-91.24	-114.96	23.72
13	-90.57	-114.96	24.39
14	-90	-114.96	24.96
15	-89.57	-114.96	25.39
16	-88.68	-114.96	26.28
17	-88.37	-114.96	26.59
18	-87.64	-114.96	27.32
19	-87.45	-114.96	27.51
20	-86.77	-114.96	28.19
21	-86.53	-114.96	28.43
22	-86.11	-114.96	28.85
23	-85.39	-114.96	29.57
24	-84.99	-114.96	29.97
25	-84.85	-114.96	30.11
26	-84.36	-114.96	30.6
27	-83.86	-114.96	31.1
28	-83.74	-114.96	31.22
29	-83.5	-114.96	31.46
30	-83.06	-114.96	31.9
31	-82.8	-114.96	32.16
32	-82.5	-114.96	32.46

Table F.2:   MGL-S8A(R) B-Dot Sensor Measured Values - TEM Cell

URS (SN 61) - -45 degrees @ 4 dBm input power			
Frequency (MHz)	Power Out (dBm)	Noise Floor (dBm)	Above Noise Floor
2	-105.99	-114.96	8.97
3	-105.22	-114.96	9.74
4	-102.96	-114.96	12
5	-100.42	-114.96	14.54
6	-98.91	-114.96	16.05
7	-98.35	-114.96	16.61
8	-97.81	-114.96	17.15
9	-96.34	-114.96	18.62
10	-96.22	-114.96	18.74
11	-95.05	-114.96	19.91
12	-94.12	-114.96	20.84
13	-94.17	-114.96	20.79
14	-92.98	-114.96	21.98
15	-92.62	-114.96	22.34
16	-91.93	-114.96	23.03
17	-91.42	-114.96	23.54
18	-91.01	-114.96	23.95
19	-90.35	-114.96	24.61
20	-90.06	-114.96	24.9
21	-89.68	-114.96	25.28
22	-89.19	-114.96	25.77
23	-88.78	-114.96	26.18
24	-87.92	-114.96	27.04
25	-87.93	-114.96	27.03
26	-87.53	-114.96	27.43
27	-87.09	-114.96	27.87
28	-86.7	-114.96	28.26
29	-86.17	-114.96	28.79
30	-86.29	-114.96	28.67
31	-85.8	-114.96	29.16
32	-85.9	-114.96	29.06

Table F.3:   MGL-S8A(R) B-Dot Sensor Measured Values - TEM Cell

URS (SN 61) - -90 degrees @ 4 dBm input power			
Frequency (MHz)	Power Out (dBm)	Noise Floor (dBm)	Above Noise Floor
2	-114.96	-114.96	0
3	-114.96	-114.96	0
4	-114.96	-114.96	0
5	-114.96	-114.96	0
6	-114.96	-114.96	0
7	-114.96	-114.96	0
8	-114.96	-114.96	0
9	-114.96	-114.96	0
10	-114.96	-114.96	0
11	-114.96	-114.96	0
12	-114.96	-114.96	0
13	-114.96	-114.96	0
14	-114.96	-114.96	0
15	-114.96	-114.96	0
16	-114.96	-114.96	0
17	-114.96	-114.96	0
18	-114.96	-114.96	0
19	-114.96	-114.96	0
20	-107.69	-114.96	7.27
21	-108.06	-114.96	6.9
22	-106.52	-114.96	8.44
23	-108.83	-114.96	6.13
24	-106.68	-114.96	8.28
25	-105.24	-114.96	9.72
26	-103.84	-114.96	11.12
27	-104.68	-114.96	10.28
28	-104.47	-114.96	10.49
29	-102.23	-114.96	12.73
30	-103.73	-114.96	11.23
31	-102.64	-114.96	12.32
32	-102.49	-114.96	12.47

Table F.4:   MGL-S8A(R) B-Dot Sensor Measured Values - TEM Cell

Frequency (MHz)	Power Out (dBm)	Noise Floor (dBm)	Above Noise Floor
URS (SN 61) - +45 degrees @ 4 dBm input power			
2	-105.96	-114.96	9
3	-103.1	-114.96	11.86
4	-104.64	-114.96	10.32
5	-102.34	-114.96	12.62
6	-100.02	-114.96	14.94
7	-98.71	-114.96	16.25
8	-97.8	-114.96	17.16
9	-97.12	-114.96	17.84
10	-96.8	-114.96	18.16
11	-96.29	-114.96	18.67
12	-94.93	-114.96	20.03
13	-94.26	-114.96	20.7
14	-93.77	-114.96	21.19
15	-93.04	-114.96	21.92
16	-92.42	-114.96	22.54
17	-91.61	-114.96	23.35
18	-91.39	-114.96	23.57
19	-90.5	-114.96	24.46
20	-90.19	-114.96	24.77
21	-89.79	-114.96	25.17
22	-89.32	-114.96	25.64
23	-88.78	-114.96	26.18
24	-88.58	-114.96	26.38
25	-88.13	-114.96	26.83
26	-87.74	-114.96	27.22
27	-87.5	-114.96	27.46
28	-87.08	-114.96	27.88
29	-86.81	-114.96	28.15
30	-86.42	-114.96	28.54
31	-86.08	-114.96	28.88
32	-85.7	-114.96	29.26

Table F.5:   MGL-S8A(R) B-Dot Sensor Measured Values - TEM Cell

URS (SN 61) - +90 degrees @ 4 dBm input power			
Frequency (MHz)	Power Out (dBm)	Noise Floor (dBm)	Above Noise Floor
2	-114.96	-114.96	0
3	-114.96	-114.96	0
4	-114.96	-114.96	0
5	-114.96	-114.96	0
6	-114.96	-114.96	0
7	-114.96	-114.96	0
8	-114.96	-114.96	0
9	-114.96	-114.96	0
10	-114.96	-114.96	0
11	-114.96	-114.96	0
12	-114.96	-114.96	0
13	-114.96	-114.96	0
14	-114.96	-114.96	0
15	-114.96	-114.96	0
16	-114.96	-114.96	0
17	-114.96	-114.96	0
18	-114.96	-114.96	0
19	-114.96	-114.96	0
20	-114.96	-114.96	0
21	-114.96	-114.96	0
22	-114.96	-114.96	0
23	-114.96	-114.96	0
24	-114.96	-114.96	0
25	-114.96	-114.96	0
26	-114.96	-114.96	0
27	-114.96	-114.96	0
28	-109.61	-114.96	5.35
29	-108.59	-114.96	6.37
30	-108.08	-114.96	6.88
31	-108.64	-114.96	6.32
32	-108.86	-114.96	6.1

Appendix G.   Prodyn Sensor Characterization Results - TEM Cell

Table G.1: MGL-S8A(R) B-Dot Sensor Measured Values - TEM Cell

Prodyn (SN 61) - 0 degrees @ 4 dBm input power			
Frequency (MHz)	Power Out (dBm)	Noise Floor (dBm)	Above Noise Floor
2	-105.47	-114.96	9.49
3	-101.31	-114.96	13.65
4	-98.99	-114.96	15.97
5	-97.99	-114.96	16.97
6	-97.68	-114.96	17.28
7	-94.58	-114.96	20.38
8	-94.46	-114.96	20.5
9	-94.44	-114.96	20.52
10	-93.73	-114.96	21.23
11	-92.03	-114.96	22.93
12	-91.93	-114.96	23.03
13	-90.81	-114.96	24.15
14	-90.19	-114.96	24.77
15	-89.57	-114.96	25.39
16	-89	-114.96	25.96
17	-88.46	-114.96	26.5
18	-88.12	-114.96	26.84
19	-87.25	-114.96	27.71
20	-86.75	-114.96	28.21
21	-86.45	-114.96	28.51
22	-85	-114.96	29.96
23	-85.47	-114.96	29.49
24	-85.17	-114.96	29.79
25	-84.75	-114.96	30.21
26	-84.31	-114.96	30.65
27	-84.19	-114.96	30.77
28	-83.79	-114.96	31.17
29	-83.35	-114.96	31.61
30	-83.15	-114.96	31.81
31	-82.75	-114.96	32.21
32	-82.61	-114.96	32.35

Table G.2: MGL-S8A(R) B-Dot Sensor Measured Values - TEM Cell

Prodyn (SN 61) - -45 degrees @ 4 dBm input power			
Frequency (MHz)	Power Out (dBm)	Noise Floor (dBm)	Above Noise Floor
2	-107.82	-114.96	7.14
3	-102.73	-114.96	12.23
4	-101.47	-114.96	13.49
5	-99.22	-114.96	15.74
6	-98.48	-114.96	16.48
7	-97.8	-114.96	17.16
8	-96.66	-114.96	18.3
9	-96.94	-114.96	18.02
10	-95.66	-114.96	19.3
11	-94.52	-114.96	20.44
12	-93.55	-114.96	21.41
13	-93.18	-114.96	21.78
14	-92.83	-114.96	22.13
15	-91.8	-114.96	23.16
16	-91.08	-114.96	23.88
17	-90.41	-114.96	24.55
18	-90.24	-114.96	24.72
19	-89.19	-114.96	25.77
20	-88.73	-114.96	26.23
21	-88.72	-114.96	26.24
22	-87.82	-114.96	27.14
23	-87.4	-114.96	27.56
24	-87.08	-114.96	27.88
25	-86.98	-114.96	27.98
26	-86.02	-114.96	28.94
27	-86.04	-114.96	28.92
28	-85.58	-114.96	29.38
29	-85.47	-114.96	29.49
30	-85.32	-114.96	29.64
31	-85.01	-114.96	29.95
32	-84.55	-114.96	30.41

Table G.3: MGL-S8A(R) B-Dot Sensor Measured Values - TEM Cell

Prodyn (SN 61) - -90 degrees @ 4 dBm input power			
Frequency (MHz)	Power Out (dBm)	Noise Floor (dBm)	Above Noise Floor
2	-113.23	-114.96	1.73
3	-113.23	-114.96	1.73
4	-113.23	-114.96	1.73
5	-113.23	-114.96	1.73
6	-113.23	-114.96	1.73
7	-113.23	-114.96	1.73
8	-113.23	-114.96	1.73
9	-113.23	-114.96	1.73
10	-113.23	-114.96	1.73
11	-113.23	-114.96	1.73
12	-113.23	-114.96	1.73
13	-113.23	-114.96	1.73
14	-113.23	-114.96	1.73
15	-113.23	-114.96	1.73
16	-113.23	-114.96	1.73
17	-113.23	-114.96	1.73
18	-113.23	-114.96	1.73
19	-113.23	-114.96	1.73
20	-113.23	-114.96	1.73
21	-113.23	-114.96	1.73
22	-113.23	-114.96	1.73
23	-113.23	-114.96	1.73
24	-111.42	-114.96	3.54
25	-109.59	-114.96	5.37
26	-107.74	-114.96	7.22
27	-106.56	-114.96	8.4
28	-109.02	-114.96	5.94
29	-109.79	-114.96	5.17
30	-107.21	-114.96	7.75
31	-110.23	-114.96	4.73
32	-108.88	-114.96	6.08

Table G.4:   MGL-S8A(R) B-Dot Sensor Measured Values - TEM Cell

Prodyn (SN 61) - +45 degrees @ 4 dBm input power			
Frequency (MHz)	Power Out (dBm)	Noise Floor (dBm)	Above Noise Floor
2	-107.99	-114.96	6.97
3	-104.91	-114.96	10.05
4	-104.8	-114.96	10.16
5	-102.85	-114.96	12.11
6	-100.01	-114.96	14.95
7	-99.32	-114.96	15.64
8	-98.75	-114.96	16.21
9	-97.51	-114.96	17.45
10	-96.49	-114.96	18.47
11	-95.54	-114.96	19.42
12	-95.51	-114.96	19.45
13	-94.95	-114.96	20.01
14	-93.86	-114.96	21.1
15	-92.56	-114.96	22.4
16	-92.41	-114.96	22.55
17	-91.85	-114.96	23.11
18	-91.57	-114.96	23.39
19	-90.67	-114.96	24.29
20	-90.6	-114.96	24.36
21	-90.36	-114.96	24.6
22	-89.51	-114.96	25.45
23	-89.29	-114.96	25.67
24	-88.86	-114.96	26.1
25	-88.36	-114.96	26.6
26	-87.79	-114.96	27.17
27	-87.66	-114.96	27.3
28	-87.42	-114.96	27.54
29	-86.98	-114.96	27.98
30	-86.97	-114.96	27.99
31	-86.53	-114.96	28.43
32	-86.3	-114.96	28.66

Table G.5:   MGL-S8A(R) B-Dot Sensor Measured Values - TEM Cell

Prodyn (SN 61) - +90 degrees @ 4 dBm input power			
Frequency (MHz)	Power Out (dBm)	Noise Floor (dBm)	Above Noise Floor
2	-112.12	-114.96	2.84
3	-112.12	-114.96	2.84
4	-112.12	-114.96	2.84
5	-112.12	-114.96	2.84
6	-112.12	-114.96	2.84
7	-112.12	-114.96	2.84
8	-112.12	-114.96	2.84
9	-112.12	-114.96	2.84
10	-112.12	-114.96	2.84
11	-112.12	-114.96	2.84
12	-112.12	-114.96	2.84
13	-112.12	-114.96	2.84
14	-112.12	-114.96	2.84
15	-112.12	-114.96	2.84
16	-112.12	-114.96	2.84
17	-112.12	-114.96	2.84
18	-112.12	-114.96	2.84
19	-112.12	-114.96	2.84
20	-112.12	-114.96	2.84
21	-112.12	-114.96	2.84
22	-112.12	-114.96	2.84
23	-112.12	-114.96	2.84
24	-112.12	-114.96	2.84
25	-112.12	-114.96	2.84
26	-112.12	-114.96	2.84
27	-109.51	-114.96	5.45
28	-108.92	-114.96	6.04
29	-109.84	-114.96	5.12
30	-110.08	-114.96	4.88
31	-107.55	-114.96	7.41
32	-109.93	-114.96	5.03

Bibliography

1. Anderson, T. "Design of a Helmholtz coil for susceptibility testing using variational calculus and experimental verification". *Electromagnetic Compatibility, 1999 IEEE International Symposium on*, volume 2, 601–604 vol.2. 1999. ID: 1.

2. Appelgren, Patrik, Cecilia Nylander, and Sten E. Nyholm. *Magnetic Field Measurement System for Microwave Frequencies*. Technical Report FOHR-1330-SE, Swedish Defence Research Agency, 2004.

3. Boriraksantikul, Nattaphong. "A TEM Cell Design to Study Electromagnetic Radiation Exposure from Cellular Phones", 2008.

4. Corbin, Clair F. *High Frequency Direction Finding Using Structurally Integrated Antennas on a Large Airborne Platform*. Master's thesis, Air Force Institute of Technology, 2011.

5. Crawford, M. L. *Measurement of EM radiation from electronic equipment using TEM transmission cells*. Technical report, NBS International, 1973.

6. Crawford, M. L. "Generation of Standard EM Fields Using TEM Transmission Cells". *Electromagnetic Compatibility, IEEE Transactions on*, EMC-16(4):189–195, 1974.

7. Edgel, W. Reed. *Electric and Magnetic Field Sensor Application*. Technical report, Prodyn Services, Inc., 1990.

8. Javor, E. R. and T Anderson. "Design of a Helmholtz coil for low frequency magnetic field susceptibility testing". *Electromagnetic Compatibility, 1998. IEEE International Symposium on*, volume 2, 912–917 vol.2. 1998.

9. McIntyre, D. E. *A Method for Generating a Cylindrical Homogeneous Magnetic*. Master's thesis, Air Force Institute of Technology, 1964.

10. Moore, H. *MATLAB for engineers*. Prentice Hall, 2009. ISBN 9780136044222. URL http://books.google.com/books?id=G9pCkkGmnKsC. 2008043571.

11. Neuhaus, John. "Coversion table for dBm at 50 ohms, 75 ohms and 600 ohms and dBmv at 75 ohms", 2002.

12. Olsen, Stewart L. *MGL-S8(R) B-Dot Sensor Development*. Final Report AFWL-TR-75-252, EG&G Inc., 1976.

13. Somsak, T., K. Chomsuwan, S. Yamada, M. Iwahara, and S. C. Mukhopadhyay. "Conductive microbead detection by Helmholtz coil technique with SV-GMR sensor". *Electronic Design, Test and Applications, 2006. DELTA 2006. Third IEEE International Workshop on*, 6 pp. 2006. ID: 1.

14. Technology, CST Computer Simulation. "CST Computer Simulation Technology", 2011.

15. Tesla Equipment Sales, Leasing and Repair. "IFI CC105 Series TEM Cell", 1997. URL `http://www.44tesla.com/commerce/ccp7742-tem-cell-cc-1xxxx-series-04287.htm###`.

16. Zahn, M. *Electromagnetic field theory: a problem solving approach.* Wiley, 1979. ISBN 9780471021988. URL `http://books.google.com/books?id=FdLvAAAAMAAJ`. 78015928.

1. REPORT DATE *(DD-MM-YYYY)* 22-03-2012	2. REPORT TYPE **Master's Thesis**	3. DATES COVERED *(From – To)* Aug 2010 – Mar 2012

4. TITLE AND SUBTITLE

Magnetic Field Generation and B-Dot Sensor Characterization in the High Frequency Band

5a. CONTRACT NUMBER

5b. GRANT NUMBER

5c. PROGRAM ELEMENT NUMBER

6. AUTHOR(S)

Hardin, Ryan L, Capt, USAF

5d. PROJECT NUMBER
JON# 11G200

5e. TASK NUMBER

5f. WORK UNIT NUMBER

7. PERFORMING ORGANIZATION NAMES(S) AND ADDRESS(S)
Air Force Institute of Technology
Graduate School of Engineering and Management (AFIT/EN)
2950 Hobson Way
WPAFB OH 45433-7765

8. PERFORMING ORGANIZATION REPORT NUMBER
AFIT/GE/ENG/12-20

9. SPONSORING/MONITORING AGENCY NAME(S) AND ADDRESS(ES)
Air Force Research Laboratory
Dr. Phil Mumford (philip.mumford@wpafb.af.mil)
(937) 528-8553
2241 Avionics Circle
Area B, B620
Wright-Patterson AFB, OH, 45433

10. SPONSOR/MONITOR'S ACRONYM(S)
AFRL/RYM

11. SPONSOR/MONITOR'S REPORT NUMBER(S)

12. DISTRIBUTION/AVAILABILITY STATEMENT
 APPROVED FOR PUBLIC RELEASE; DISTRIBUTION UNLIMITED

13. SUPPLEMENTARY NOTES
This material is declared a work of the U.S. Government and is not subject to copyright protection in the United States

14. ABSTRACT

   Designing a high frequency (HF) magnetic field direction finding (DF) array for use onboard a military aircraft is the challenge that drives the effort of the research presented. The frequency range of interest, 2-32 MHz, has a maximum wavelength (150 meters) that approaches the maximum length of the platform on which the array is to be used. The large wavelengths in the HF range make it difficult to accurately estimate from which direction a magnetic field is emitting.

   The primary goal of this research is to characterize the performance of the MGL-S8A (Multi-Gap loop) B-Dot sensor. Although the sensors are designed to operate at frequencies above 5 GHz, their small size and potential to accurately detect magnetic fields in the 2-32 MHz range make them likely to be one type of an ensemble of sensors in the design of a HF DF array. The sensors are also characterized at angles of 0, 45, -45, 90, and -90 degrees. Each sensor is characterized using two different types of magnetic field generators, a transverse electromagnetic (TEM) cell and a Helmholtz coil.

   The sensors can accurately measure electromagnetic (EM) fields in the HF range. Although the detection capability of the sensors is good, small differences between the 0 and 45 degree measurements may make it difficult for the sensors to be used in a DF array.

15. SUBJECT TERMS
High frequency magnetic field sensors, high frequency magnetic field generation, Helmholtz coil, TEM cell

16. SECURITY CLASSIFICATION OF:			17. LIMITATION OF ABSTRACT	18. NUMBER OF PAGES	19a. NAME OF RESPONSIBLE PERSON Geoffrey A. Akers, Lt Col ,USAF (ENG)
REPORT **U**	ABSTRACT **U**	c. THIS PAGE **U**	**UU**	125	19b. TELEPHONE NUMBER *(Include area code)* (937) 255-3636 x4659 Geoffrey.akers@afit.edu